

Controlled Growth of Vertically Aligned Single-Walled Carbon Nanotubes for Devices

デバイス応用に向けた垂直配向単層 CNT の合成制御

by XIANG, Rong

項 栄

A thesis presented in partial fulfillment of
the requirements for the degree of
DOCTOR OF PHILOSOPHY

東京大学大学院工学系研究科機械工学専攻

Department of Mechanical Engineering
The University of Tokyo

August 2009



Content

Chapter 1 Introduction	1
1. 1 Organization.....	1
1.2 The many forms of carbon	2
1.3 SWNT fundamentals.....	3
1.4 Characterization methods.....	10
1.4.1 Optical absorption spectroscopy.....	11
1.4.2 Resonant Raman spectroscopy.....	12
1.4.3 Electron microscopy	16
1.5 Vertically aligned SWNTs from alcohol.....	18
1.5.1 SWNT synthesis	18
1.5.2 The ACCVD method	19
1.5.3. Achieving vertical alignment	20
1. 6 Applications of vertically aligned carbon nanotubes.....	22
1.6.1 Enhanced performance.....	23
1.6.2 Unique phenomena	24
1.6.3 Convenient platform.....	27
Chapter 2 Root growth mechanism and diffusion limit	29
2.1 Background.....	29
2.2 Root growth or tip growth.....	31
2.2.1 Characterization of VA-SWNT from noflow condition.....	31
2.2.3 Isotope labeling and root growth	33
2.3 Diffusion limit or Catalyst deactivation.....	37
2.3.1 General 1D diffusion model	40
2.3.2 First order reaction confirmed by experiment.....	46
2.3.3 Results for SWNT and MWNT	46
2.3.4 Solution for a diffusion-limited process	49
2.4 Sub-millimeter long VA-SWNTs from ACCVD	51
2.5 Summary.....	52
Chapter 3 Growth acceleration and ethanol decomposition	55
3.1 Background and motivation	55
3.2 Acetylene accelerated ACCVD	58
3.2.1 Effect of different species.....	58
3.2.2 Acetylene acceleration	59
3.2.3 Possible mechanism	61
3.2.4 Revealing other reaction pathways to SWNTs	63
3.3 Thermal decomposition of Ethanol.....	67
3.4 Summary.....	70
Chapter 4 Diameter control of VA-SWNTs	71
4.1 Background and motivation	71
4.2 Quantitative evaluation along a SWNT array.....	74
4.2.1 Cross-sectional Raman scan.....	74
4.2.2 Decomposed UV-vis-NIR optical absorption.....	75
4.3 Diameter tailoring.....	77

4.3.1 Effect of CVD parameters	77
4.3.2 Effect of catalyst recipe	78
4.3.2.1 UV-vis-NIR optical absorption	79
4.3.2.2 Raman spectroscopy	80
4.3.2.3 TEM and histogram	81
4.4 Summary	82
Chapter 5 High-precision patterned growth	83
5.1 Background and motivation	83
5.2 SWNT growth on Si/SiO ₂ patterns	84
5.3 Effect of surface wettability	90
5.3 SWNT pattern obtained from UV lithography	94
5.4 SWNT patterns obtained from e-beam lithography	96
5.5 Summary	98
Chapter 6 Conclusions and prospect	99
References	101
Appendix	107
Acknowledgements	111
Curriculum Vitae	113
Publication list	115

Chapter 1 Introduction

1. 1 Organization

This thesis begins with a brief introduction to single-walled carbon nanotubes (SWNTs), followed by a discussion of some of the physical properties of SWNTs. This will provide the foundation upon which the results presented later will be based. After the general introduction, some general techniques for characterizing and evaluating SWNTs are introduced, which will be referenced throughout this work. The history of vertically aligned SWNT synthesis will be reviewed, and several examples will be given to show the potential applications of aligned arrays.

Results of the research conducted during this PhD are presented beginning in Chapter 2, which discusses the investigation of the growth process of vertically aligned (VA-)SWNT films. In this section I utilized isotope labeling to conclusively affirmed the location of the metal catalyst. Since all the SWNTs are found to be root growth. I modeled the diffusion behavior of carbon precursor and quantitatively evaluated the role of diffusion resistance on the deceleration of the SWNT growth.

Chapter 3 presents a growth acceleration phenomenon, which gives insights into several fundamental issues in the catalytic growth process of SWNTs. Together with theoretical and experimental analysis on the decomposition of ethanol, I revealed hidden precursors for the SWNT formation and also obtained semi-quantitative contribution of different species.

In chapter 4, I carried out a comprehensive characterization on the diameter of aligned SWNTs. SWNTs in the root part of array was found to be slightly thicker than the top. After this detailed analysis, the effect of different CVD parameter and the catalyst recipe on the

average diameter was studied. Average diameter of VA-SWNTs can be tuned down to ~1.3 nm.

I proposed a novel technique for localizing the growth of SWNTs in chapter 5. This technique is also through liquid route, which is compatible to dip-coating process. The method is easier than conventional lithography but, more importantly, possess potential for sub 10 nm resolution. An example of constructing field effect transistors using as-grown SWNTs will be presented.

1.2 The many forms of carbon

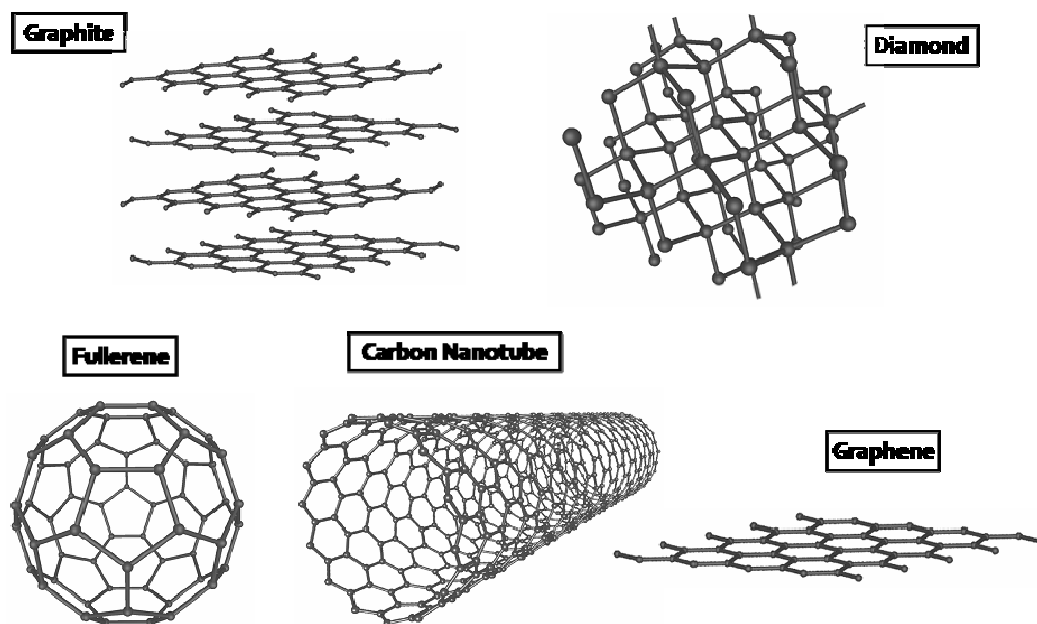


Figure 1-1. Atomic structures of bulk (graphite and diamond) and nano-size (fullerene, carbon nanotube and graphene) carbon materials. (images from wikipedia)

Carbon can take on many forms, the most well-known being graphite commonly found in the cores of pencils and diamond commonly found on engagement rings. These are the two bulk forms of carbon, illustrated in Figure 1-1. Graphite has a layered, planar structure. In

diamond, however, each atom shares a bond with every neighboring atom, forming a tetrahedral structure.

In addition to these two forms, a new allotrope of carbon, called a fullerene, was discovered in 1985 by Robert F. Curl, Sir Harold W. Kroto, and Richard E. Smalley,^[1] a breakthrough for which they were awarded the Nobel prize in chemistry in 1996. The most well-known of these fullerenes is the “buckyball”, or C₆₀. Due to its spherical symmetry and small size (consisting of 60 atoms), it is essentially a zero-dimensional (0D) material, also known as a quantum dot. With the discovery of fullerenes, members of the carbon family included the 3D forms of diamond and graphite, 2D graphene, and 0D fullerenes. So what about a one-dimensional material? One can imagine forming a 1D carbon allotrope by either elongating a buckyball, or by rolling up a 2D graphene sheet into a narrow, tubular structure.

This is exactly the structure discovered in 1993,^[2, 3] and is known as a single-walled carbon nanotube (SWNT). In fact, both single- and multi-walled forms^[4, 5] of this material exist, but the physical properties of SWNTs have proved to be much more interesting, and will be addressed in the following chapter. The properties of these new materials were intriguing enough to spawn an entire new field called nanotechnology, attracting researchers from almost all scientific disciplines.

Meanwhile, each stacked layer comprising bulk (3D) graphite can be treated as a weakly-interacting 2D form of graphite, called graphene, which is a rising star in the field of nano-carbon. Physical properties and potential applications of graphene have been explored at a tremendous speed since several years ago.^[6]

1.3 SWNT fundamentals

The structure of the sp^2 carbon network of a two-dimensional (2D) graphene sheet is schematically presented as a hexagonal lattice in Figure 1-2a. The shadowed rhombus

indicates a unit cell of the graphene, which contains two non-equivalent C atoms. The distance between neighboring atoms a_{c-c} is 1.42 Å, and vectors \mathbf{a}_1 and \mathbf{a}_2 represent the unit vectors of the cell. The Brillouin zone of the graphene is denoted in Figure 1-2b as a shadowed hexagon, and vectors \mathbf{b}_1 and \mathbf{b}_2 are the reciprocal vectors. These are expressed as

$$\mathbf{a}_1 = \left(\frac{\sqrt{3}}{2}a, \frac{a}{2} \right), \quad \mathbf{a}_2 = \left(\frac{\sqrt{3}}{2}a, -\frac{a}{2} \right) \quad (1)$$

and

$$\mathbf{b}_1 = \left(\frac{2\pi}{\sqrt{3}a}, \frac{2\pi}{a} \right), \quad \mathbf{b}_2 = \left(\frac{2\pi}{\sqrt{3}a}, -\frac{2\pi}{a} \right) \quad (2)$$

based on the x - y and k_x - k_y coordinates, respectively, as shown in Figure 1-2. In these equations, the lattice constant of the 2D graphene is defined as $a \equiv |\mathbf{a}_1| = |\mathbf{a}_2| = 1.42 \text{ \AA} \times 3^{1/2} = 2.46 \text{ \AA}$. By convention, high symmetry points at the center, corner, and the midpoint of the neighboring corners of the Brillouin zone are denoted as Γ , M, and K points, respectively.

The unit cell of SWNTs is enlarged when compared to that of the graphene due to the lower symmetry of SWNTs. Figure 1-3 shows an unrolled hexagonal lattice of a SWNT, in which the unit cell of a certain type of SWNT is indicated as a shadowed area. The vectors \mathbf{C}_h and \mathbf{T} that connect two crystallographically equivalent sites in the circumferential and axial directions of SWNTs, respectively, are also shown. These vectors are termed the chiral vector and the translational vector, respectively, as further explained below.

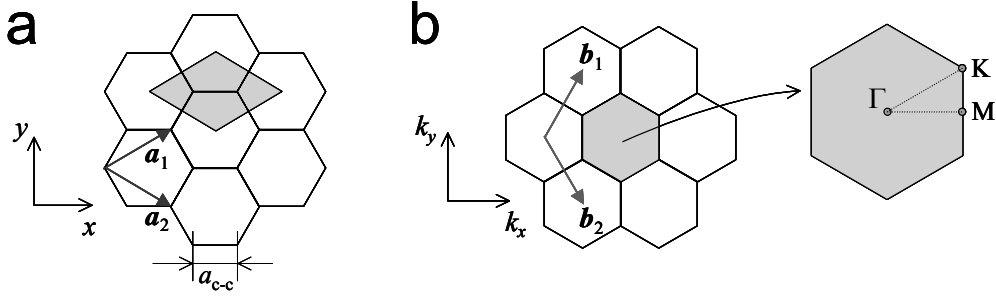


Figure 1-2. (a) Unit cell and (b) Brillouin zone of 2D graphite represented as the shadowed rhombus and hexagon, respectively. \mathbf{a}_i and \mathbf{b}_i ($i = 1, 2$) are unit vectors and reciprocal lattice vectors, respectively. The high-symmetry points in the 2D Brillouin zone conventionally called Γ , K, and M point, are also shown.

The chiral vector \mathbf{C}_h is expressed in terms of real-space unit vectors \mathbf{a}_1 and \mathbf{a}_2 and two integers n and m ($0 \leq m \leq n$) as

$$\mathbf{C}_h = n\mathbf{a}_1 + m\mathbf{a}_2 \equiv (n, m) \quad (3)$$

The type of SWNT is completely specified by the two integers (n, m) through the definition given in Eq. 3. Since the length of \mathbf{C}_h indicates the circumferential length of the SWNT, the diameter of the SWNT, d_t , is expressed as

$$d_t = \frac{|\mathbf{C}_h|}{\pi} = \frac{\sqrt{\mathbf{C}_h \cdot \mathbf{C}_h}}{\pi} = \frac{a\sqrt{n^2 + m^2 + nm}}{\pi} \quad (4)$$

Here, $a \equiv |\mathbf{a}_1| = |\mathbf{a}_2| = 1.44 \text{ \AA} \times 3^{1/2} = 2.49 \text{ \AA}$ is the lattice constant of the honeycomb lattice of the SWNT. A slightly greater C–C bond length in SWNTs compared to that in the graphene (1.42 \text{ \AA}) should be noted.

The angle formed by \mathbf{C}_h and \mathbf{a}_1 is termed chiral vector θ , and its value is $0 \leq \theta \leq 30^\circ$ due to the hexagonal symmetry of the honeycomb lattice; specifically, it is expressed as

$$\cos\theta = \frac{\mathbf{C}_h \cdot \mathbf{a}_1}{|\mathbf{C}_h| |\mathbf{a}_1|} = \frac{2n + m}{2\sqrt{n^2 + m^2 + nm}} \quad (5)$$

The translational vector \mathbf{T} is defined as the unit vector of a 1D SWNT, which is parallel to the SWNT axis. From the relationship $\mathbf{C}_h \cdot \mathbf{T} = 0$,

$$\mathbf{T} = t_1 \mathbf{a}_1 + t_2 \mathbf{a}_2 \equiv (t_1, t_2), \quad t_1 = \frac{2m+n}{d_R}, \quad t_2 = -\frac{2n+m}{d_R} \quad (6)$$

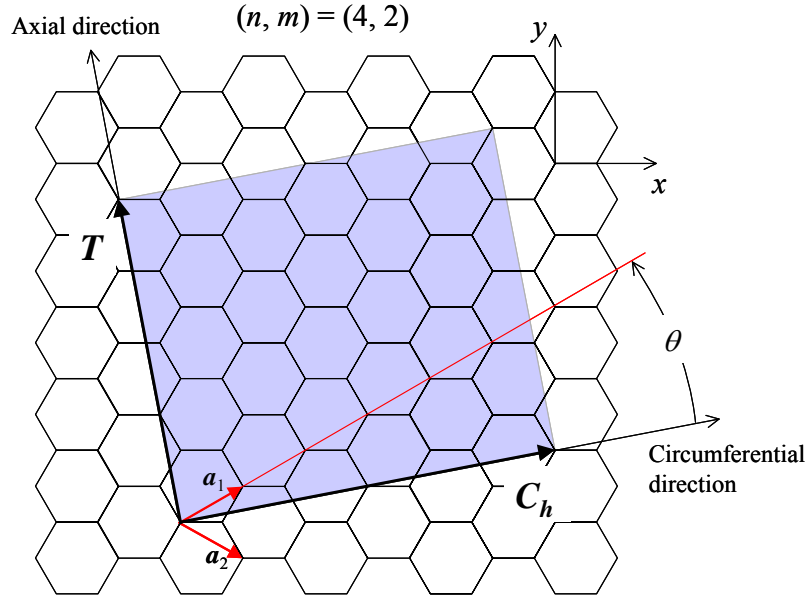


Figure 1-3. Unrolled hexagonal lattice of a SWNT. The chiral vector \mathbf{C}_h and translational vector \mathbf{T} are presented for the case of $\mathbf{C}_h = 4\mathbf{a}_1 + 2\mathbf{a}_2$ SWNT. Its unit cell is denoted as shadowed area in which $N = 28$ hexagons are contained. The angle between \mathbf{a}_1 and \mathbf{C}_h gives the chiral angle θ ($0 \leq \theta \leq 30^\circ$).

where d_R is the greatest common divisor (gcd) of $(2m+n)$ and $(2n+m)$. Using the above defined d_R , the number of hexagons in the unit cell of a SWNT N is expressed as

$$N = \frac{|\mathbf{C}_h \times \mathbf{T}|}{|\mathbf{a}_1 \times \mathbf{a}_2|} = \frac{2(n^2 + m^2 + nm)}{d_R} \quad (7)$$

Therefore, there are $2N$ carbon atoms in the unit cell of a SWNT. For example, $(n, m) = (4, 2)$ SWNT shown in Figure 1-3 has 28 hexagons in the unit cell.

Since the unit cell of a SWNT is 2D and specified by the orthogonal lattice vectors \mathbf{C}_h and \mathbf{T} , as shown in Figure 1-3, the reciprocal lattice vectors corresponding to the circumferential direction \mathbf{K}_1 and the axial direction \mathbf{K}_2 are defined such that the following relationships are satisfied:

$$\mathbf{C}_h \cdot \mathbf{K}_1 = \mathbf{T} \cdot \mathbf{K}_2 = 2\pi, \quad \mathbf{C}_h \cdot \mathbf{K}_2 = \mathbf{T} \cdot \mathbf{K}_1 = 0 \quad (8)$$

Solving these relations using Eqs. 6 and 7, \mathbf{K}_1 and \mathbf{K}_2 are expressed as

$$\mathbf{K}_1 = \frac{1}{N}(-t_2\mathbf{b}_1 + t_1\mathbf{b}_2) \quad (9)$$

$$\mathbf{K}_2 = \frac{1}{N}(m\mathbf{b}_1 - n\mathbf{b}_2) \quad (10)$$

Figure 1-4 shows the reciprocal lattice vectors \mathbf{K}_1 and \mathbf{K}_2 for $(n, m) = (4, 2)$ SWNT. The first Brillouin zone of the SWNT is expressed as a line segment W-W' as shown in Figure 1-4a. Therefore, N line segments $\mu\mathbf{K}_1$ ($\mu = 1, \dots, N-1$) give rise to N discrete wave vectors, which originate from the quantized wave vector in the direction of \mathbf{C}_h due to the periodic boundary condition imposed in this direction.

The electronic structure of a SWNT can be obtained from that of 2D graphite. When the energy dispersion relation of 2D graphite is denoted as $E_{g,2D}$, N pairs of 1D energy dispersion relation $E_\mu(k)$ are expressed as

$$E_\mu(k) = E_{g,2D}\left(k \frac{\mathbf{K}_2}{|\mathbf{K}_2|} + \mu\mathbf{K}_1\right), \quad (\mu = 0, \dots, N-1, \text{ and } -\frac{\pi}{|\mathbf{T}|} < k < \frac{\pi}{|\mathbf{T}|}) \quad (11)$$

Here, k denotes the wave number along the SWNT axis. If these energy dispersion curves are collected (or folded) into the first Brillouin zone of the 2D graphene by translating them using multiples of \mathbf{K}_1 and \mathbf{K}_2 , Figure 1-4a is equivalently expressed as Figure 1-4b in the reduced zone scheme. This expression shows that the wave vectors possible in the case of SWNTs are limited from the case of 2D graphene. The line indicating the possible wave vector shown in Figure 1-4b will hereafter be referred to as “cutting line”.

Such a quantized wave vector of SWNTs causes a sharp divergence in their eDOS, termed “van Hove singularities,” that is characteristic of 1D materials. Figure 1-5 shows the eDOS of $(n, m) = (4, 2)$ SWNT calculated by the tight-binding method with parameters $\gamma_0 = 2.9$ eV, $s = 0$, and $a_{c-c} = 0.144$ nm. Since it is obvious that the cutting line of this SWNT—described by Eq. 11—does not pass the K -point, in which the valence and conduction bands meet in the case of 2D graphene, the $(n, m) = (4, 2)$ SWNT is *semiconducting* in which eDOS is absent at

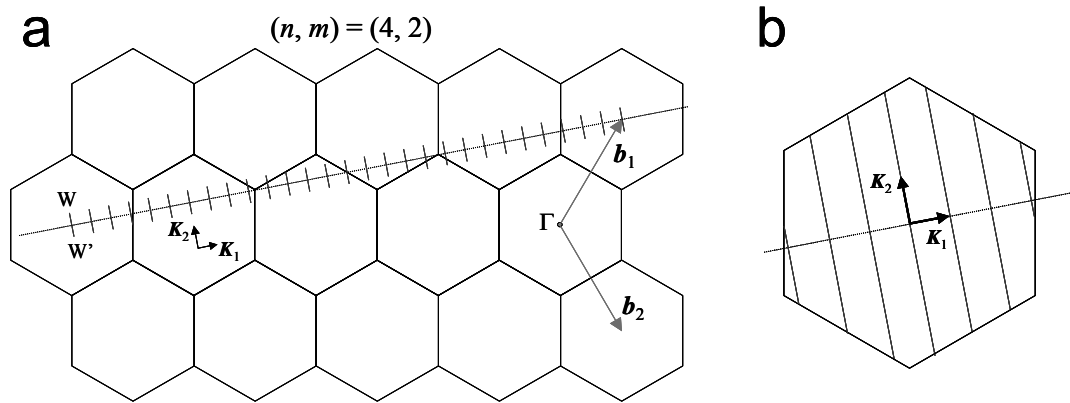


Figure 1-4. (a) Brillouin zone of a SWNT represented by the line segment W-W' for the case of $(n, m) = (4, 2)$ SWNT, and (b) its equivalent representation displayed by the reduced-zone scheme. The vectors \mathbf{K}_1 and \mathbf{K}_2 are reciprocal lattice vectors correspond to \mathbf{C}_h and \mathbf{T} , respectively.

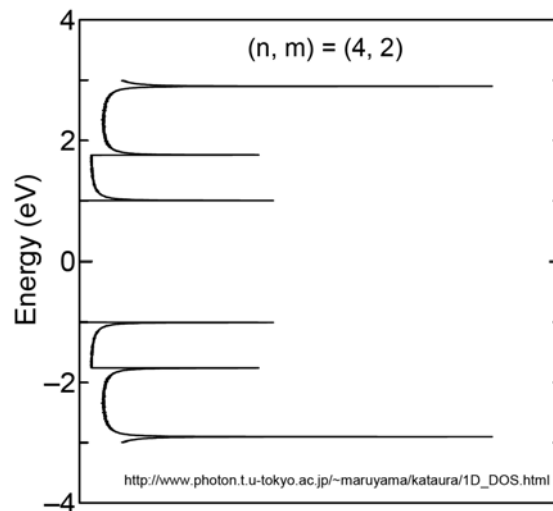


Figure 1-5. eDOS of $(n, m) = (4, 2)$ SWNT calculated by tight-binding method with $\gamma_0 = 2.9$ eV, $s = 0$, and $a_{c-c} = 0.144$ nm.

the Fermi level. On the other hand, when the cutting line passes the K-point in the case of e.g. $(n, m) = (5, 2)$ SWNT, the SWNT is metallic in which eDOS is at the Fermi level. In general, $\text{mod}(n - m, 3) = 0$ SWNTs are metallic and $\text{mod}(n - m, 3) \neq 0$ SWNTs are semiconducting. One of the most important characteristics of SWNTs is that the difference of metallic/semiconducting transport properties is determined solely by the chirality.

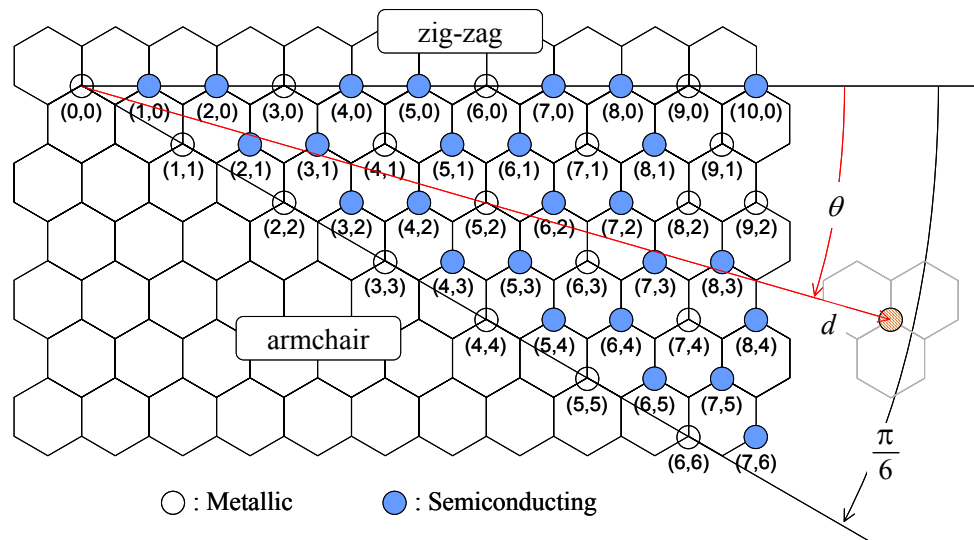


Figure 1-6. The (n, m) of SWNTs that are metallic (open circles) and semiconducting (solid circles), respectively, denoted on the map of chiral vectors (n, m) . Any chirality is specified either by two integers (n, m) or, equivalently, a combination of diameter d and chiral angle θ .

Figure 1-6 shows the chiral mapping of (n, m) SWNTs that are either metallic (open circles) or semiconducting (solid circles). Any chirality is specified either by two integers (n, m) or equivalently, a combination of diameter d and chiral angle θ , as schematized in this figure. Among these, the SWNTs with $m = 0$ (i.e., $\theta = 0^\circ$) and $n = m$ (i.e., $\theta = 30^\circ$) chirality are termed “zig-zag” and “armchair” types, respectively. This is because the edges of their tubes look like a zigzag and an armchair, as shown in Figure 1-7a and 1-7b, respectively. The SWNTs that do not belong to either of these types are the “chiral” type, as shown in Figure 1-7c.

The fundamental characteristics, structure, and notational system presented in this section will be used in subsequent chapters, in which specific topics are studied in detail.

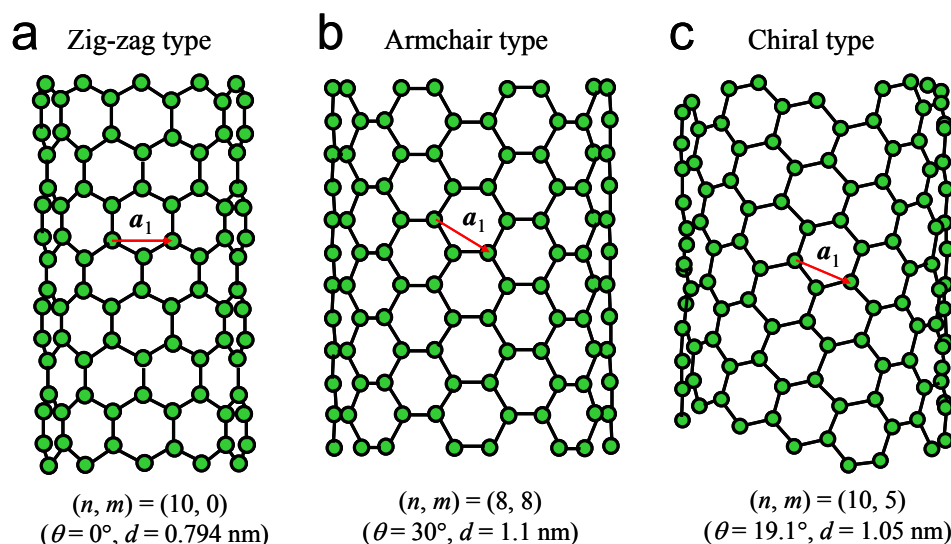


Figure 1-7. Structure of (a) zig-zag type, (b) armchair type, and (c) chiral type SWNTs represented by $(n, m) = (10, 0)$, $(8, 8)$, and $(10, 5)$ tubes.

1.4 Characterization methods

In the previous section I discussed some of the physical aspects of SWNTs, and showed how the one-dimensionality of a SWNT gives rise to singularities in the electronic density of states. Since this electronic structure depends on the (n, m) of a given nanotube, experimental probes of the electronic structure can reveal much information about the diameter, chirality, and metallic or semiconducting nature of a nanotube sample. Furthermore, since optical techniques obtain information via photon interactions, they are usually very well suited for use as non-destructive characterization methods. In this section, I will introduce two optical spectroscopic methods commonly used to characterize SWNTs. Beside these, electron microscopes are powerful tools for revealing the morphologies and structures of grown SWNTs. The information obtained from electron microscope observation is more

straightforward and sometime more comprehensive than that from optical tools, where signal from small amounts of SWNTs could be significantly enhanced.

1.4.1 Optical absorption spectroscopy

As light propagates through an absorbing medium, its intensity decreases exponentially according to the Beer-Lambert law,

$$I(L) = I_0 e^{-\alpha L c}, \quad (12)$$

where $I(L)$ is the intensity of the incident light, α the absorption coefficient, L the optical path length, and c the concentration of absorbing species in the material. By measuring the transmitted intensity relative to the incident intensity, the absorbance (for a given wavelength λ) can be calculated from the following expression

$$A = -\log_{10} \left(\frac{I}{I_0} \right). \quad (13)$$

In optical absorption spectroscopy, the wavelength of the incident light is scanned through some spectral range -- usually covering the ultraviolet, visible, and near infra-red (UV-vis-NIR) spectral regions -- throughout which the absorbance is determined using equation (13). Features in the resulting absorption spectrum can be mapped directly to features in the electronic states of the material, thus this technique is useful for SWNT characterization and analysis. In particular, if the incident photon energy matches the energy separation between Van Hove singularities in the SWNT density of states, the absorption probability increases dramatically, provided the transition is allowed. This will show up as a peak in the absorption spectrum. Since the DOS depends on the chirality of the SWNT, the diameter and metallic or semiconducting nature can also be determined from the peak energies, making absorption spectroscopy an important tool for SWNT characterization.

The optical properties of a material are a direct consequence of the electronic nature of the material. As shown in the previous section, both metallic and semiconducting SWNTs exhibit Van Hove singularities in their electronic DOS. This results in valence and conduction band states, between which optically-induced electronic transitions can occur. However, the possible transitions are restricted due to symmetry considerations.^[7] Due to the 1D nature of SWNTs, these optical selection rules are different depending on the polarization of the incident light with respect to the SWNT axis. The result is highly anisotropic absorption, which is strong for polarization parallel to the SWNT axis, and much weaker for perpendicular polarization. Therefore, optical absorption spectroscopy can give qualitative information of the orientation of the detected SWNTs, when polarized incident light is used.

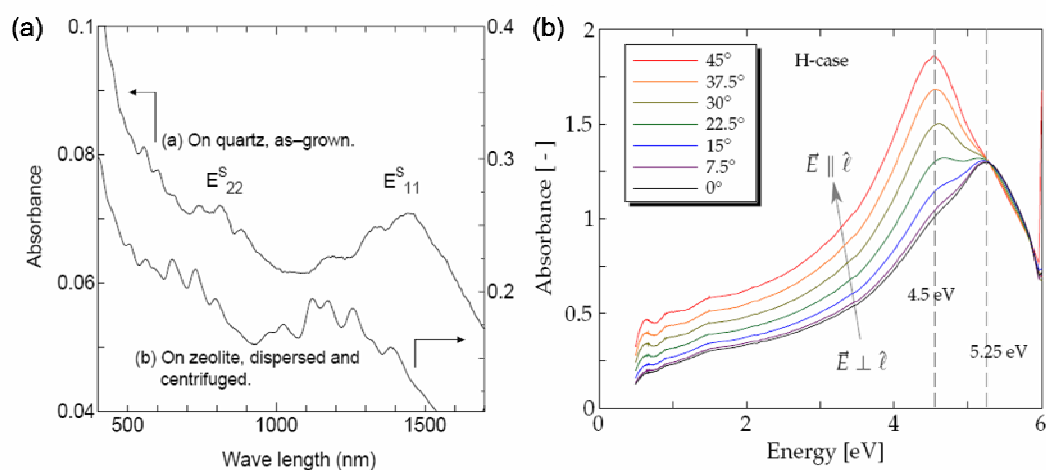


Figure 1-8. Typical optical absorption spectra of surfactant dispersed SWNTs, as grown random SWNTs grown on quartz (a) and vertically aligned SWNTs grown on quartz (b).

1.4.2 Resonant Raman spectroscopy

Raman scattering is the *inelastic* scattering of a photon, which occurs in roughly one of every 10^7 scattering events. Most other scattering events are elastic (Rayleigh) processes. Since the inelastic scattering chance is low, in order to obtain a decent measurement of this

signal it is necessary to increase the frequency of scattering events. One way to accomplish this is to use a laser as the light source, unlike in optical absorption spectroscopy, where a lamp is sufficient.

As previously mentioned, SWNTs with different chiralities have different electronic density of states. As a result, the energy differences E_{ii} between singularities i in the valence and conduction bands are unique for every (n,m) nanotube. This plays a very important role in Raman spectroscopy of SWNTs because a strong resonance occurs when the energy of the excitation light is close to E_{ii} . This resonant Raman effect dramatically increases the scattering probability, which gives rise to a strong peak in Raman spectra. Because of this resonance, the Raman signals detected for different excitation energies can be used to identify SWNTs of different (n,m) . This makes Raman spectroscopy one of the most important optical techniques for characterization of SWNTs. However, due to this strong resonance effect, a Raman spectrum, particularly radial breathing modes, doesn't reflect comprehensively the population distribution inside a sample.

Figure 1-9 is a typical Raman spectrum of vertically aligned SWNTs. The dominant peak at around 1590 cm^{-1} in the Raman spectrum corresponds to a resonant excitation of in-plane optical phonons, reflecting the graphitic nature of the nanotube.^[8] For this reason, this peak is called the G-band, where G stands for graphite. However, unlike graphite, the curvature of the SWNT causes the axial and transverse in-plane vibrational modes to have a slight difference in energy. These vibrations are indicated by the red and blue arrows in Figure 1-10.

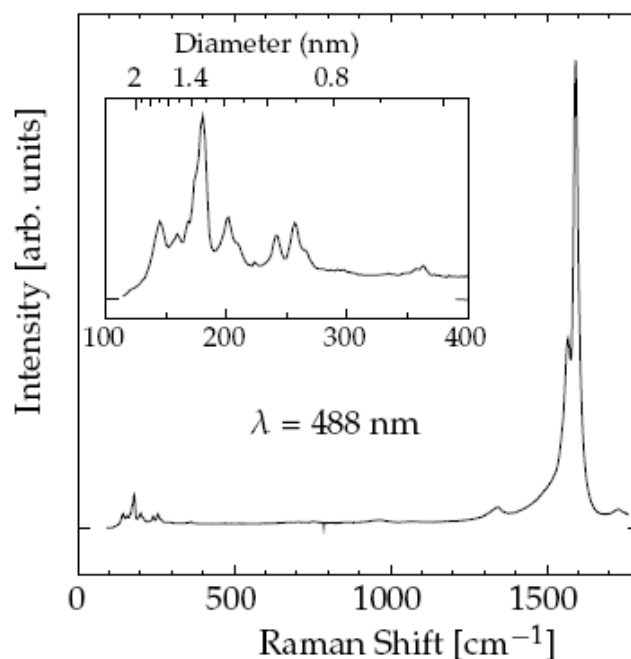


Figure 1-9. A typical Raman spectrum of vertically aligned SWNTs (488 nm excitation laser). The RBM peaks are shown in the insert.

This energy difference causes the G-band peak to split into a lower energy G^- peak and a higher energy G^+ peak. Interestingly, it has been shown that the relative shift of the transverse and longitudinal modes is opposite for semiconducting and metallic SWNTs.^[9, 10] The scattering process associated with the G-band excitation is a first-order process, meaning one scattering event occurs. Second-order scattering can occur when excited phonons are scattered by defects or inconsistencies in the crystal lattice. This shows up in Raman spectra of SWNTs as a small hump near 1350 cm^{-1} called the disorder band, or D-band.

The last major feature visible in the spectrum in Figure 1-9 is the series of peaks below 400 cm^{-1} (magnified in the insert). These peaks are from a phonon excitation that is unique to SWNTs, and contain much information about the nanotubes present in the sample. Recall that the G-band mode described above is caused by a resonant in-plane vibrational mode, which is characteristic of graphite. An out-of-plane modes also exists, where the vibration is perpendicular to the lattice plane.^[11] If one imagines taking a graphene sheet supporting such

an out-of-plane vibration, and rolling it into the cylindrical shape of a SWNT, the out-of-plane vibrations become oriented radially away from the SWNT axis, as shown in Figure 1-10b. The result is a purely radial mode, where the diameter of the entire SWNT oscillates, appearing as though it were “breathing”. For this reason, this mode is known as the radial breathing mode, or RBM. The RBM is also a resonant Raman mode, which is in resonance when the energy of the incident photons matches an energy gap E_{ii} in the SWNT density of states. The fact that the RBM is unique to SWNTs makes Raman spectroscopy a quick and easy method to confirm the presence of SWNTs in a sample, as well as to estimate the diameter distribution and overall sample quality. In general it is possible to detect the RBM from the inner and outer walls of a DWNT,^[12] but additional walls strongly dampen these radial modes.

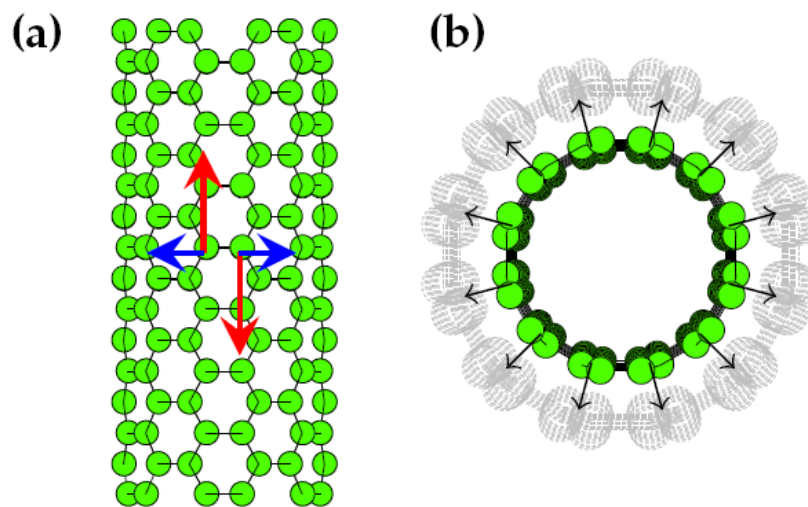


Figure 1-10. (a) the in-plane vibrational modes corresponding to the G-band Raman signal, and (b) the uniform out-of-plane vibration that gives rise to the radial breathing mode (RBM).

As one might expect, the frequency of the RBM depends on the diameter of the SWNT, thus each peak in the spectrum corresponds to a SWNT of a certain diameter (note the diameter scale on the upper axis in the inset in Figure 1-9). This diameter dependence has been thoroughly studied, and the experimental data show a very well-behaved relationship.^[13]

Based on these data, the RBM frequency ω_{RBM} (cm^{-1}) is related to the SWNT diameter d_t (nm) by the empirical equation

$$\omega_{RBM} \approx \frac{218}{d_t} + 16. \quad (14)$$

As seen in this equation, ω_{RBM} is roughly inversely proportional to the SWNT diameter, thus as the SWNT diameter increases, ω_{RBM} decreases. Since the region near 0 cm^{-1} is suppressed by the notch filter, it is difficult to detect RBM peaks from large-diameter SWNTs.

Using different excitation energies, RBMs of different frequencies -- corresponding to different SWNTs -- will be excited. This makes it possible to "map out" the diameter distribution of a sample by scanning the excitation laser through a wide energy range. This multi-wavelength strategy has been recently used to confirm the enrichment of semi-conducting SWNTs grown on flat substrates.^[14, 15]

1.4.3 Electron microscopy

Electron microscopy is an indispensable tool used in many areas of science. Just as the wavelike nature of light is used to produce an image in a light microscope, the wavelike nature of electrons to produce an image in an electron microscope, thereby obtaining much higher resolution (magnification exceeding 100,000X). Images are produced by scanning an electron beam over a sample in a raster pattern, and then detecting the scattered electrons. A microscope designed for this purpose is called a scanning electron microscope, or SEM. A field emission (FE-)SEM uses a field emitter to obtain an intense electron beam, which further improves the resolution. Figure 1-11 (a) shows an electron micrograph of carbon

nanotube bundles obtained using an FE-SEM, which unambiguously reveals the morphologies, e.g. alignment, of SWNT samples.

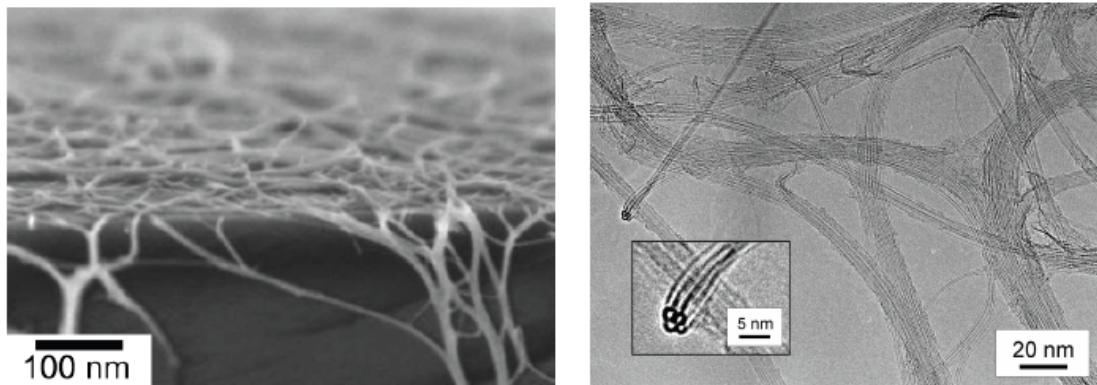


Figure 1-11. A high-resolution FE-SEM image of SWNT bundles lying on a substrate surface (left), and a TEM image of SWNT bundles (right). Individual SWNTs within a bundle can be seen in the insert.

In addition to the SEM there is another kind of electron microscope that is capable of even higher magnification (over 1,000,000X). This is achieved not by detecting electrons scattered by a material, but rather by detecting electrons that have *passed through* the sample or *diffracted* by the sample. This is accomplished by accelerating the electrons to high energies (typically > 100 keV) and specially preparing the sample so that it is thin enough for the incident electrons to pass through. A microscope operating on this principle is called a transmission electron microscope, or TEM. A good TEM is capable of atomic resolution, thus gives an extremely accurate picture of the crystal structure of a material. A TEM image of SWNTs produced from alcohol is shown in Figure 1-11 (b).^[16] The single-layered tube walls can be made out in the image. A bundle of four SWNTs is shown in the inset. From atomic-resolution image or diffraction pattern of a SWNT one can determine the chirality of the SWNT. If enough amount of samples is characterized by this method one by one. Though time consuming, TEM gives the most reliable statistical information on the diameter and

chirality distribution of a SWNT sample, e.g. semi-conducting enriched sample prepared by density gradient ultra-centrifugation.^[17, 18]

1.5 Vertically aligned SWNTs from alcohol

1.5.1 SWNT synthesis

In the first few years following their discovery, highly crystalline, few-defect SWNTs could be produced by only a few methods, such as the arc discharge^[19] and laser over methods,^[20] but the pace of research was inhibited because SWNTs could not be produced on the scale required for most experiments. SWNT synthesis became much simpler when Hongjie Dai and coworkers at Rick Smalley's group at Rice University (the same Rick Smalley who was awarded the Nobel prize for the discovery of C₆₀) developed a method by which SWNTs could be produced by chemical vapor deposition (CVD),^[21] in which the carbon source used for CVD growth was a carbon containing gas, such as CO, reacted with metal catalyst particles inside a heated reactor. This quickly became the most common SWNT production method, but the quality of the SWNTs produced varied from laboratory to laboratory.

In the late 1990s, again at Rick Smalley's group, a SWNT synthesis process called HiPco was developed,^[22] by which SWNTs were synthesized by a high-pressure disproportionation reaction of CO. This was the first time gram-scale quantities of SWNTs could be synthesized in a reproducible fashion. Requests for samples poured in from laboratories around the world. Many of these requests were filled, and HiPco nanotubes subsequently became the *de facto* SWNT standard, allowing direct comparison of experimental results from various experiments carried out at laboratories around the world. This significantly accelerated the

pace of SWNT research, and many significant advancements in the field soon followed. However, nanotechnology was still in its infancy.

One major challenge in nanotechnology is controlling the morphology of SWNTs during synthesis. Morphologically-controlled growth is critical for the realization of many proposed nanotube-based applications. A major advance in this area came in 2003, with the synthesis of vertically-aligned SWNTs^[23] using an alcohol-based CVD growth process.^[16]

1.5.2 The ACCVD method

There are many SWNT production methods, each with its own advantages and disadvantages. However, one problem common to all of them is the presence of impurities, usually in the form of catalyst particles or amorphous carbon formed during SWNT synthesis.

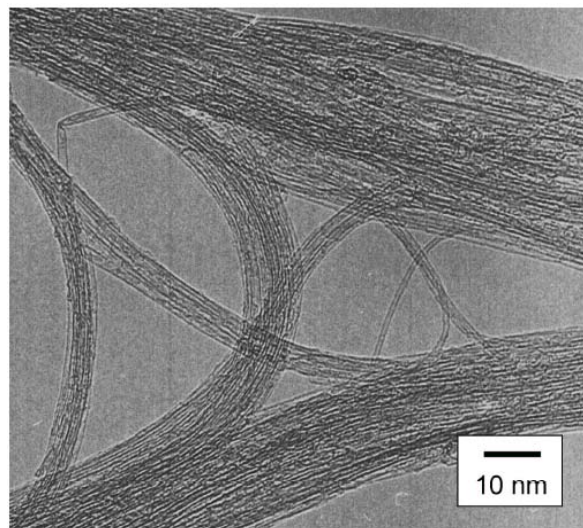


Figure 1-12. A TEM image showing bundles of high-purity SWNTs synthesized from alcohol.^[16]

In 2002, it was reported that high-purity SWNTs could be grown using alcohol as the carbon feedstock gas.^[16] A TEM image of SWNTs synthesized from alcohol is shown in

Figure 1-12. This alcohol catalytic chemical vapor deposition (ACCVD) method has since become one of the most popular methods used for low-cost, high-purity SWNT synthesis. This lack of amorphous carbon was attributed to the OH radical present in alcohols, which preferentially reacts with carbon molecules that have dangling bonds. This effectively etches away those carbon atoms that are most likely to produce amorphous carbon.^[16, 24] The details of the growth mechanism, however, are not yet well understood. It is known, however, that SWNT growth is a catalytic process, by which a carbon-containing molecule reacts with a metal catalyst particle and precipitates a nanotube. The general CVD process is still being investigated by many different methods, including molecular dynamics simulations.^[25]

1.5.3. Achieving vertical alignment

Another significant advance in SWNT research was the synthesis of vertically aligned SWNTs.^[23] This had previously been achieved using multi-walled carbon nanotubes, but SWNTs are known to form bundles, bound together by Van der Waals forces. This typically results in a tangled mess of random SWNTs, often likened to spaghetti. However, due to their one-dimensionality, many SWNT properties are anisotropic, thus control over the orientation is highly desirable for exploiting these anisotropic properties. For SWNTs, this was achieved by combining the aforementioned ACCVD method with a liquid-based catalyst loading method,^[26] described as follows.

Catalyst loading was performed by submerging an optically polished quartz substrate into a solution containing Co acetate and Mo acetate dissolved in ethanol. The amount of each metal species in the solution was 0.01 wt.%. The substrate was immersed in the Co/Mo

solution for approximately 10 minutes, then slowly withdrawn from the solution at 4 cm min⁻¹.

The thin liquid film on the substrate surface after withdrawing from the solution contains a nearly homogeneous mixture of the dissolved metals. The dip-coated substrate is then baked in air at 400°C for 5 min to remove the acetate and oxidize the metals. Formation of this oxide fixes the catalyst in place on the substrate surface, thereby resisting agglomeration at high temperatures (e.g. 800°C). The result is densely deposited, mono-dispersed catalyst particles 10⁵ particles per μm² with diameters of approximately 1.5 nm.^[27] It is believed that this high catalyst density leads to vertically aligned growth. Due to the high catalyst density, the presence of SWNTs in close proximity to one another limits their lateral freedom during growth, thus they orient themselves perpendicular to the substrate and grow in an aligned fashion.

Since oxidized metals are generally catalytically inactive,^[28] the oxidized catalyst particles were reduced prior to SWNT growth. This was done by supplying an Ar/H₂ mixture (3% H₂, Ar balance) at a flow rate of 300 sccm and pressure of 40 kPa during heating of the CVD reaction chamber. After reaching the growth temperature (650-850°C), the Ar/H₂ mixture was stopped and ethanol vapor (99.5% dehydrated ethanol) was introduced to initiate SWNT growth. For our system the alcohol pressures inside the growth chamber during SWNT synthesis were 1.3kPa.

The produced SWNTs have an average diameter of 1.9-2.0 nm and are several micrometers in length.^[29] An FE-SEM image of VA-SWNTs produced by the ACCVD method is shown in Figure 1-13.

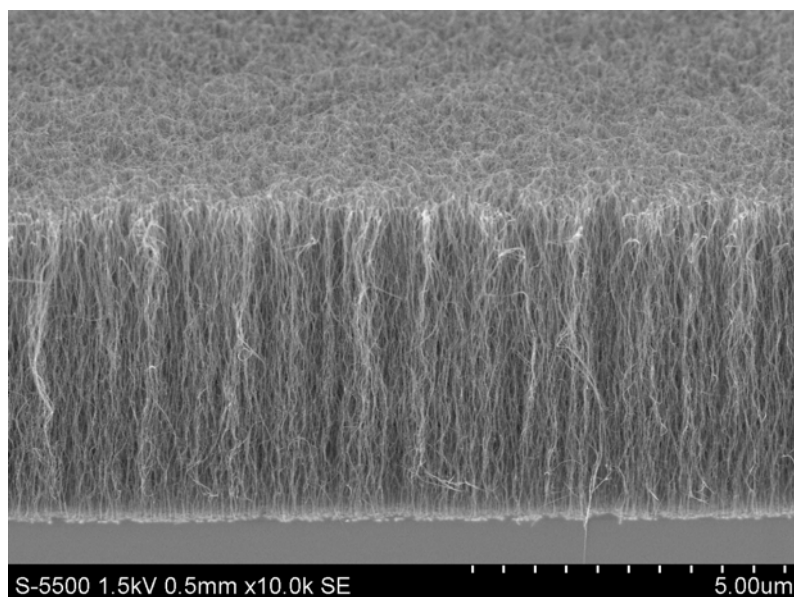


Figure 1-13. A typical SEM image of VA-SWNTs grown on quartz substrate from ACCVD.

After this first success in producing VA-SWNTs, such forest-like structures were also obtained by other groups using different methods, including water-assisted super-growth,^[30] microwave plasma CVD,^[31] O₂-assisted CVD,^[32] and etc..^[33-36] The key here is just how to form mono-dispersed catalyst with small diameters (for achieving single-shell) uniformly on a substrate in high density (for achieving vertical alignment).

When SWNTs get assembled into aligned structure, their anisotropic properties are enhanced. Therefore, such aligned structures have been used to study the fundamental properties of SWNTs. At the same time, many potential applications basing on this unique and beautiful structure have been demonstrated. A short overview will be given in a next section.

1. 6 Applications of vertically aligned carbon nanotubes

Before starting this section, it is worth noting that people have already been able to produce vertically aligned multi-walled carbon nanotubes (VA-MWNTs) since 1998 (6 years

earlier than the first report of VA-SWNTs) using various CVD approaches.^[37-39] Some of the concepts proposed for VA-MWNTs also apply to VA-SWNTs. In this part, the general advantages resulted from *alignment* of CNTs will be reviewed (though the unique applications of SWNTs that is not achievable for MWNTs will also be emphasized). Since there are tremendous work related to this topic, they are categorized into three aspects. In each subsection, several examples will be given.

1.6.1 Enhanced performance

When CNTs get orientated identically in their axis direction, the first appeal is that their properties, such as high electrical, thermal conductivity, high strength and modulus, will be enhanced. For example, in a CNT/polymer composite, thermal conduction along the direction in which CNTs are aligned in the matrix will be significantly enhanced.^[40] The incensement will be larger than the case when random CNTs are used, where large thermal resistance remains at CNT-CNT boundaries.^[41] Same things happen in applications using the electrical conductivity of CNTs.^[42] There are even reports showing even when such aligned CNTs are dispersed, the performance in enhancing thermal and electrical conductivity of a composite will be better than originally random CNTs.^[43] Possible mechanism is that such aligned CNTs usually grow much longer, millimeter or even centimeter long CNT can be obtained. When (probably only when) CNTs are aligned on fiber, the elastic modulus and strength of such hybrid architectures is also increased.^[44, 45]

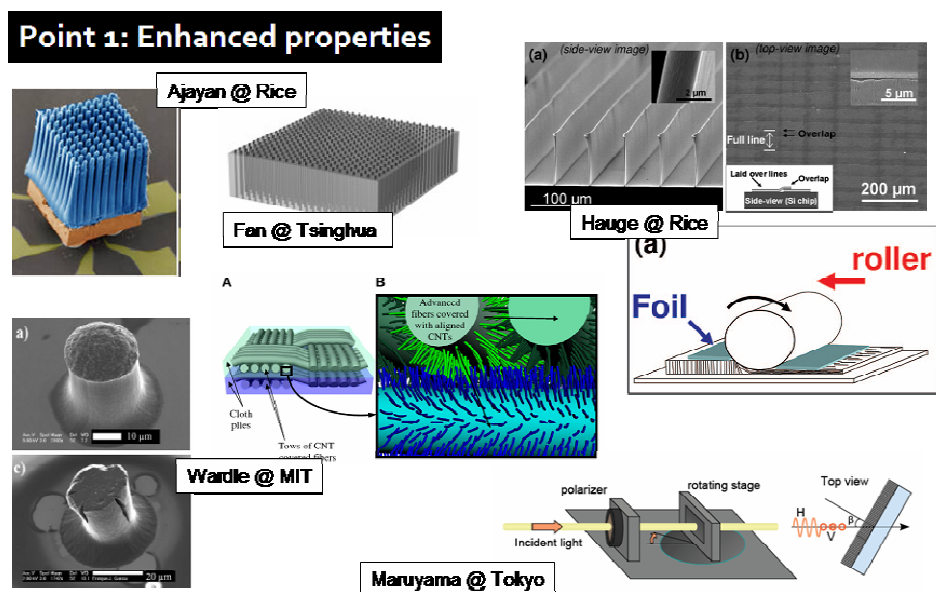


Figure 1-14. Examples showing when CNTs are orientated identically their performance in many applications will be enhanced.

An aligned SWNT array is also a good platform to study the optical properties of SWNTs. For example, the absorption and excitation of a SWNT by a photon is polarization sensitive. For one SWNT, the study on this topic will be hard due to sample preparation and SWNT allocation. For a film consisting of aligned SWNTs, however, such polarization dependence will be easily observed in Raman spectroscopy or optical absorption.^[46, 47] There have been recently techniques forming horizontally aligned SWNT sheets from VA-SWNT patterns.^[48] Such sheets can be easily fabricated into large area and even used as a wafer for lithography.^[49] SWNT cantilever terahertz polarizer^[50] has been achieved.

1.6.2 Unique phenomena

Among the properties and applications of CNTs, there are some that were not achieved or never expected before CNTs get aligned. One example is drawing continuous yarns from a VA-CNT forest. Though the mechanism is still mysterious, many applications have been

proposed, such as polarizer,^[51] multi-functional CNT yarns/films,^[52, 53] artificial muscle, TEM grid,^[54] and loudspeaker.^[55] It is believed only super aligned MWNTs can be spin into such type of continuous yarns.^[56] VA-SWNTs, if spinnable, will undoubtedly generate more applications.

Another interesting example is mimic “gecko foot” using aligned CNT structures. The dry adhesion of CNT structure was not expected before the first report in 2005. Yurdumakan et al. demonstrated an adhesion strength of 200 times stronger than that of the observed average of a gecko’s foot by dipping an AFM tip into the MWCNT bundle.^[57] Later, Zhao et al. achieved dry adhesion between MWCNT array surfaces and various target surfaces over millimeter-sized contact areas.^[58] The adhesive strengths were measured over 10 N/cm² in the normal direction and about 8 N/cm² in the shear direction with glass surface. By patterning the growth and transferring the VA-CNT micro-structure, based on the hierarchical structure found on the foot of a gecko lizard. The gecko tape can support a shear stress (36 N/cm²) nearly four times higher than the gecko foot and sticks to a variety of surfaces, including Teflon. For the first time, a macroscopic flexible patch that can be used repeatedly with peeling and adhesive properties performs better than the natural gecko foot.^[59] Such synthetic foot can be also self-cleaned.^[60] Dai et al. have achieved a record recently using CNT arrays that are dominated by a straight body segment but with curly entangled top. Macroscopic adhesive forces of ~100 N/cm², almost 10 times that of a gecko foot, and a much stronger shear adhesion force than the normal adhesion force, were obtained.^[61] They claimed this anisotropic force distribution is due to the shear-induced alignments of the curly segments of the nanotubes. It is worth noting that most of the experiments above were demonstrated on MWNTs, SWNTs patterns, if fabricated controllably in a better manner, may yield more striking performance.

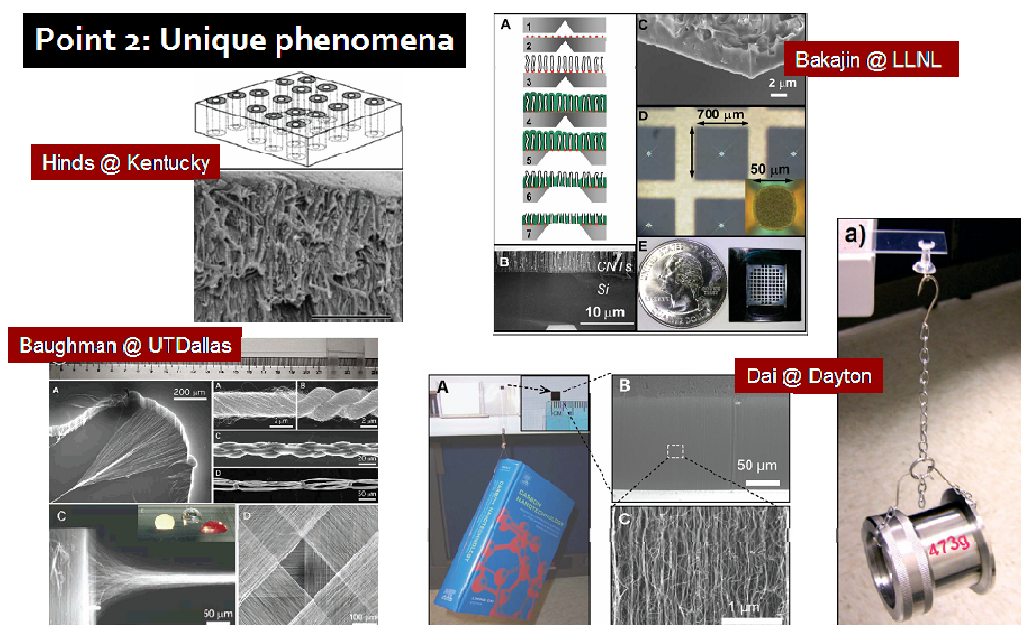


Figure 1-15. Examples showing when CNTs are orientated identically they may generate unique properties that can be utilized for novel applications.

In recent years, numerous simulations of water transport through SWNTs have suggested not only that water occupies the SWNT channels, but also that fast molecular transport takes place, far in excess of what continuum hydrodynamic theories would predict if applied on the length scale of 1-2 nm.^[62, 63] However, it is not until when SWNTs were aligned into a film that people experimentally proved measured gas flow exceeds predictions of the Knudsen diffusion model by more than an order of magnitude.^[64] More importantly the measured water flow exceeds values calculated from continuum hydrodynamics models by more than three orders of magnitude and is comparable to flow rates extrapolated from molecular dynamics simulations.^[65] The gas and water permeabilities of the nanotube-based membranes are also several orders of magnitude higher than those of commercial polycarbonate membranes, despite having pore sizes an order of magnitude smaller. These membranes enable fundamental studies of mass transport in confined environments, as well as more energy-efficient nanoscale filtration.

1.6.3 Convenient platform

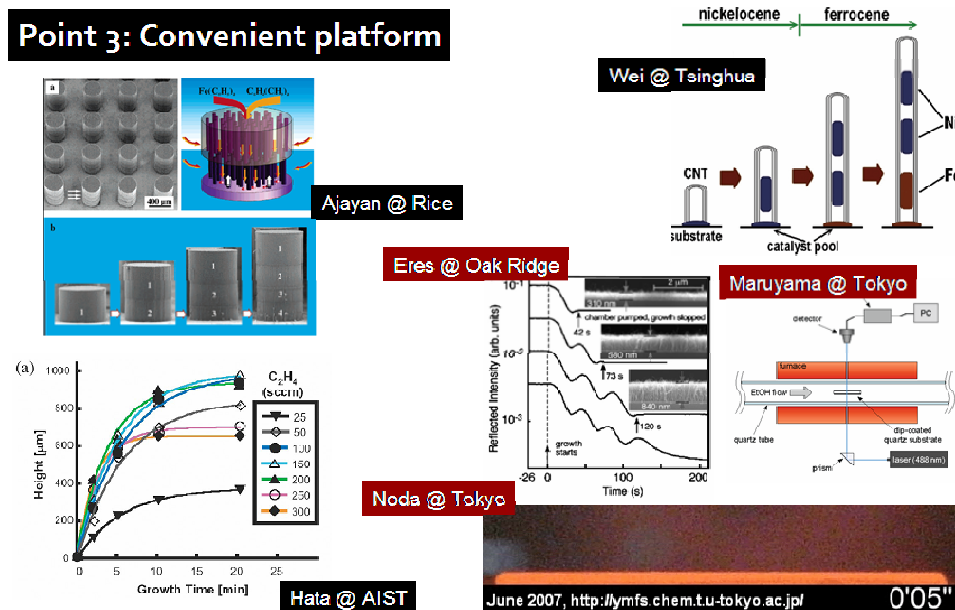


Figure 1-16. Examples showing aligned CNT arrays are very convenient for studying the growth mechanism and kinetics.

When CNTs grow on a flat substrate and self-assemble into a macroscopic film, it becomes more convenient to study the growth behavior on such aligned CNTs than on those random networks. For example, the catalyst can be easily located in such aligned structure. The thickness of the film can be easily measured by various methods. This value, which is believed to be similar to the CNT length inside an array, can be used to resolve the growth kinetics. Figure 1-16 summarized some related work done on aligned CNT arrays.

It is widely believed that the growth of a CNT follows so-called Vapor-Liquid-Solid (VLS) model.^[66] The metal catalyst could either sit on the substrate (root growth) or move upwards along with the CNT by staying at the top (tip growth).^[67] A classic work was done using isotope labeling, where Liu et al. showed conclusively MWNTs in their thermal CVD process follow root growth mechanism.^[68] More importantly, they also confirmed that multiple shells of a MWNT were formed at the same time (rather than one layer by another).

Similar results were obtained by Ajayan Group where another layered growth approach was used.^[69] These results indicate that the carbon precursors (also catalyst precursor in a ferrocene process) needs to diffusion through the thick as grown film, which initiated the intensive discussion on the catalyst behavior and diffusion-limited growth (to be continued in this thesis).^[70, 71] The aligned CNTs have accelerated the progress in studying the growth mechanism of CNTs.

Since CNT length in a vertically aligned array can be easily measured, the time-resolved grow kinetics of CNTs can be obtained after enough CVD runs for different durations. This information is important for understanding when and why CNT stop the growth. Further, it becomes more convenient when various smart techniques were proposed to *in situ* measure/record the film thickness. These approaches, including reflectivity measurement,^[72] layered growth,^[73] laser absorption,^[74] direct optical imaging, make the parametric study on CNT growth behavior magnitude more efficient. Maruyama et al proposed the exponential decay of the SWNT growth, and studied the effect of temperature and pressure on the growth rate and catalyst life time.^[75] Similar work was done on MWNTs by Eres et al using their reflectivity measurement.^[76] However, Noda et al recently found a different behavior where CNT length extends linearly for several minutes while stops suddenly within 10 seconds. The same phenomenon was reported by Hart et al., who claimed the sudden growth termination is related to the morphology change at the root of an array.^[77] There have also been models proposed where people attempts to explain certain behavior or generalize various growth kinetics.^[78-80] More discussion are still ongoing and also to be continued in this thesis.

Chapter 2 Root growth mechanism and diffusion limit

2.1 Background

A single-walled carbon nanotube (SWNT)^[2, 3] is a novel one-dimensional material possessing attractive electric, mechanical, and thermal properties.^[81] Driven by the potential applications of SWNTs, many methods have been proposed to synthesize SWNTs.^[16, 19-23, 30-32] Among these, alcohol catalytic chemical vapor deposition (ACCVD) can yield high-quality SWNTs at moderate temperatures.^[16] It is also the first method by which vertically aligned SWNT arrays were obtained.^[23] However, the incomplete understanding of the growth mechanism in this process, such as insufficient information about the catalyst status and position during growth, hinders the full control over the final product.

Isotope labeling is a powerful technique for identifying the reaction pathway in chemical reactions. It has been used to identify the catalyst location, i.e. to determine whether root growth or tip growth^[67] occurs in the synthesis of multi-walled carbon nanotubes (MWNTs), and also the growth sequence of graphene layers in MWNTs.^[68, 82] One challenge in applying this isotope method to ACCVD is that, due to the high ethanol flow rate, the percentage of supplied ethanol converted into the final SWNT product is typically as low as 0.04%. This low efficiency makes the use of an isotope-labeled carbon source prohibitively expensive. Therefore, an improvement in the efficiency of ethanol use in the current ACCVD method is necessary.

Isotope-labeled aligned SWNTs are also useful for identifying the different vibration modes in Raman spectroscopy studies, as the presence of isotopes changes the phonon energy while keeping the electron structure unaltered.^[83, 84] A bulk material with a controlled isotope

concentration, or a sequenced nanotube junction might also be interesting regarding thermal conductivity in SWNTs.^[85]

In this chapter, I present the successful synthesis of aligned ¹³C labeled single-walled carbon nanotube (SWNT) arrays from alcohol by a modified no-flow chemical vapor deposition (CVD) method that makes efficient growth possible using a small amount of carbon source. The synthesis of high-quality SWNTs by this alternative method was confirmed by resonance Raman spectroscopy, which also showed that the quality of the grown SWNTs is uniform in growth direction. The synthesis of ¹³C labeled SWNTs provides solid evidence for the root growth mechanism in alcohol catalytic CVD, which agrees well with the transmission electron microscopy (TEM) observations

After confirming the root growth mechanism, Feedstock and byproduct diffusion in the root growth of aligned carbon nanotube arrays is discussed. A non-dimensional modulus is proposed to differentiate catalyst-poisoning controlled growth deceleration from one which is diffusion controlled. It is found that, at current stage, aligned multi-walled carbon nanotube arrays are usually free of feedstock diffusion resistance while single-walled carbon nanotube arrays are already suffering from a strong diffusion resistance. The method presented here is also able to predict the critical lengths in different CVD processes from which carbon nanotube arrays begin to meet strong diffusion resistance, as well as the possible solutions to this diffusion caused growth deceleration.

2.2 Root growth or tip growth

2.2.1 Characterization of VA-SWNT from noflow condition

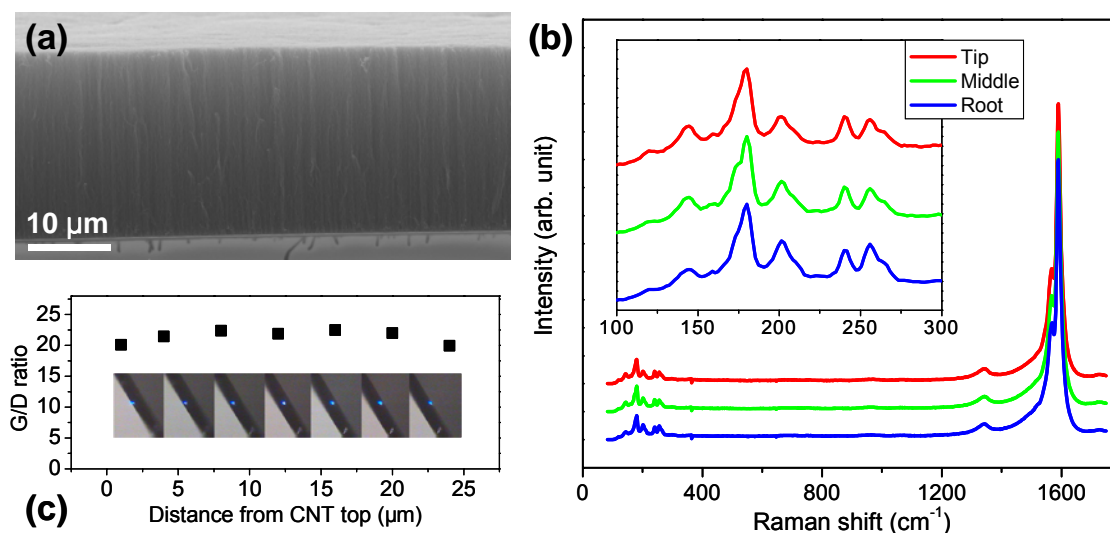


Figure 2-1: (a) SEM image of the as-grown aligned SWNTs obtained from no-flow CVD, (b) Raman spectra at different positions along the height of the SWNT array measured by keeping the incident light polarization perpendicular to SWNT growth direction, (c) ratio of G/D peak intensities at different positions along the SWNT arrays. The inset shows optical microscope images showing the corresponding incident laser positions.

Figure 2-1(a) shows a typical SEM image of an array of 25 μm aligned SWNTs grown by 10 min no-flow CVD. One significant difference between the no-flow condition and conventional CVD is that, as there is no refreshment of gas inside the chamber, the gas composition continually changes during growth. Accordingly, the quality of the SWNTs at different heights in the array might vary. Additionally, the SWNT growth by-products, e.g., H₂O, might also have a more significant impact than in conventional CVD. Therefore, the as-grown arrays were characterized by micro-Raman spectroscopy, which allowed me to obtain spectra from several small regions (approximately a few μm²) along the height of the array. All spectra obtained from different locations on the film, as shown in Figure 2-1(b),

gave clear and similar-shaped peaks at radial breathing mode (RBM) region. The intensity ratio of G-band to D-band varied only from 20 to 23 (Figure 2-1(c)), which suggests that the SWNT quality is uniform from the top to the root. Transmission electron microscopy (TEM) observation also confirmed that the arrays are comprised of SWNTs with little amorphous carbon; no MWNTs were found. Notably, the absence of constant ethanol replacement in the chamber resulted in some difference in the growth curves, but the reason for this is still being investigated.

In this process, the most attractive feature of the no-flow condition is that the conversion rate of ethanol to SWNTs is much higher than in the conventional CVD method. As the ethanol flow rate in conventional ACCVD is typically 450 sccm, 10 min CVD usually consumes around 9 g ethanol but yields only about 2 mg SWNTs on both sides of the substrate, that is, the carbon conversion rate is as low as 0.04%. However, for the no-flow condition, a similar amount of SWNTs can be obtained merely from about 10 mg ethanol enclosed inside the chamber. The carbon conversion rate was thereby estimated to be as high as 40%. Thus, no-flow CVD enabled us to grow SWNTs from small amounts of ethanol, which is critical for the successful synthesis of aligned ^{13}C SWNT arrays from our 0.5 g of ^{13}C ethanol and also for the cost performance of future advances in SWNT mass production.

Figure 2-2(a) shows a typical Raman spectrum of a 4 μm aligned SWNT film obtained in 1 min using 0.02 g of ^{13}C ethanol. As only 0.01 to 0.02 g of ethanol is needed for one CVD run, more than 20 samples of ^{13}C aligned SWNTs can be produced with 0.5 g of ethanol. The G band, D band, and RBM peaks in the Raman spectrum are all shifted by $\sqrt{12/13}$ from the ^{12}C position (dashed line), confirming the apparent isotope effect. This shift is due to the larger atomic mass of ^{13}C , which results in a different phonon energy. As the electronic structure of the isotope does not change, the optical absorption spectra in Figure 2-2(b) show little difference in the peak positions. However, there is a shift of the plasmon peak to a lower

energy, which may be caused by poor alignment.^[47] It was also noted that the catalyst lifetime for the ^{13}C case is usually shorter than when using conventional ^{12}C ethanol, and thereby the ^{13}C SWNT film is usually thinner than a conventional ^{12}C SWNT one. The incubation time required to initiate the CNT growth was also noted in case of ^{13}C ethanol but it never happened for conventional ^{12}C ethanol under similar pressure. These features of ^{13}C ethanol case might be caused by the impurities in the as-purchased ^{13}C ethanol, as isotope-labeled molecules are not expected to behave very differently in chemical reactions.

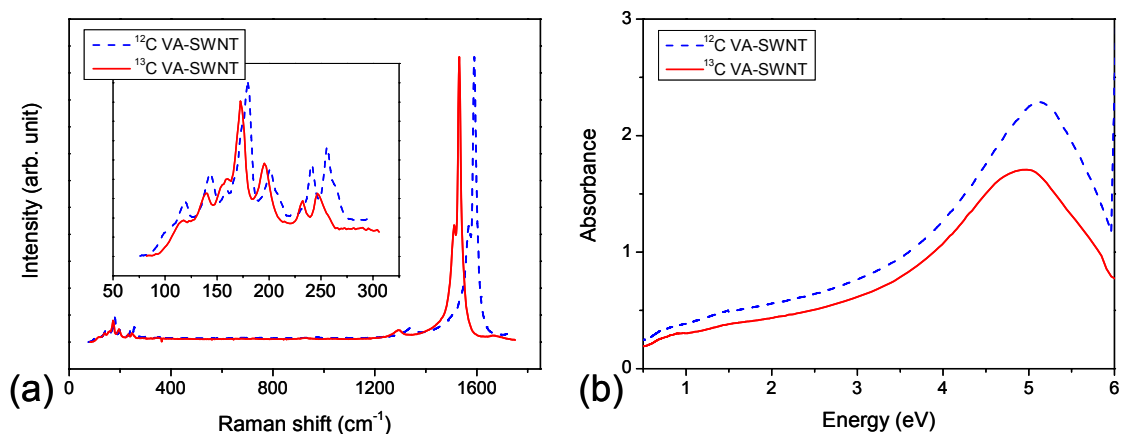


Figure 2-2: (a) Raman and (b) optical absorption spectra of the ^{13}C (red and solid lines) and ^{12}C (blue and dashed lines) vertically aligned SWNT (VA-SWNT) arrays, showing (a) the shifted phonon energy and (b) the similar electronic

2.2.3 Isotope labeling and root growth

As well as the pure ^{13}C carbon nanotubes, I also grew ^{12}C - ^{13}C SWNT junctions, which are interesting for understanding the SWNT growth mechanism or studying the thermal conductivity of SWNTs. Figure 2-3(a) shows an example of a ^{12}C - ^{13}C junction, synthesized by first feeding ^{12}C ethanol, followed by evacuating the chamber and then feeding ^{13}C ethanol. From the growth curve obtained from *in situ* optical absorption shown in Figure

2-3(b), the entire array contains 8 μm of ^{12}C and 1 μm of ^{13}C nanotubes. As the ^{12}C is fed before the ^{13}C , the location of this 1 μm ^{13}C can be used to clarify whether the SWNTs are grown from the root of the array or from the tip. Figure 2-3(c) shows the change in Raman spectra along the array. It is clearly shown that ^{13}C can only be detected near the root of the SWNT array; this is solid evidence for the root growth mechanism, shown by the schematic in the inset of Figure 2-3(b). However, it is also worth noting that, before introducing ^{13}C ethanol, we evacuated the chamber for 30 s to remove the residual ^{12}C ethanol. This short pause in growth might have an effect on the catalyst particles, e.g., they might form discontinuous layers as reported before.^{21,22} Therefore, I conducted a similar “pause-restart” experiment with only conventional ^{12}C ethanol, and it was found that most of the time no obvious interface is formed in such a short pause, and that after restarting, the SWNTs reached a similar growth rate to that before. This suggests that the influence of such a short growth pause might be not so significant. However, even this 30 s pause affected the catalyst by causing some SWNTs to be renucleated or the growth mode to be changed, the current location of ^{13}C (near the root) still confirms the catalyst particles were originally at the root of the SWNTs. This negligible effect of the short pause for conventional ^{12}C ethanol also confirms that the lower growth rate for the second stage of growth shown in Figure 2-3 is probably only because of some impurities in ^{13}C ethanol rather than due to the short pause in growth.

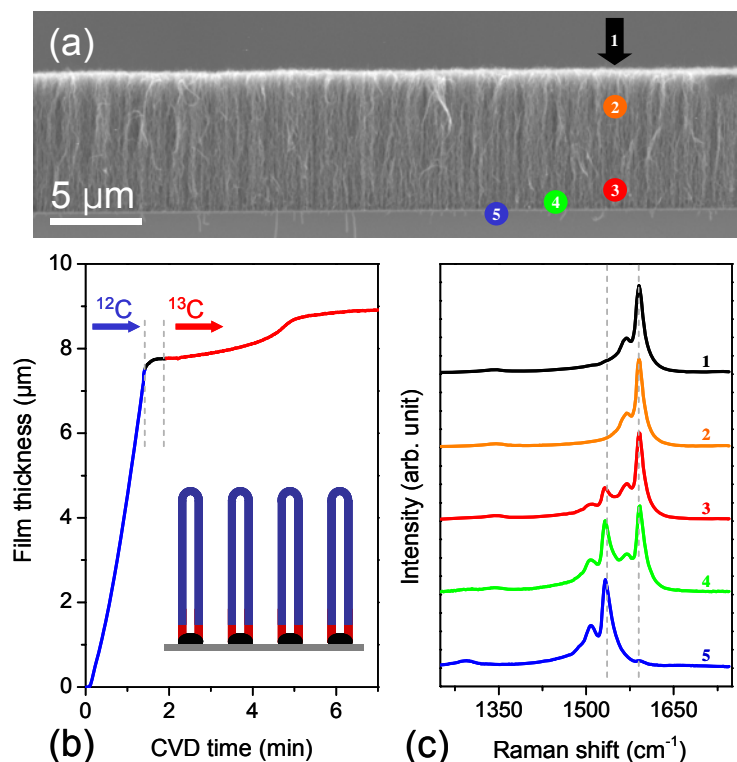


Figure 2-3: (a) SEM image, (b) growth curve from *in situ* optical absorption, and (c) cross-sectional Raman spectra across a ^{12}C - ^{13}C junction. The arrow and spots in (a) represent the positions of the incident light. The inset schematic in (b) illustrates the junction structure in the case of root growth.

This result is also consistent with TEM observation. A typical TEM image in Figure shows most of the catalyst particles are usually located at one edge of the array, which is identified as the root region according to the results of this study. The other edge, i.e., the tip region, was usually clean and metal species were seldom observed. The reason why the root model is usually found to be dominant in the case of vertical growth, which has also been confirmed in other CVD processes,^[68-71, 82, 86] might need further investigation.

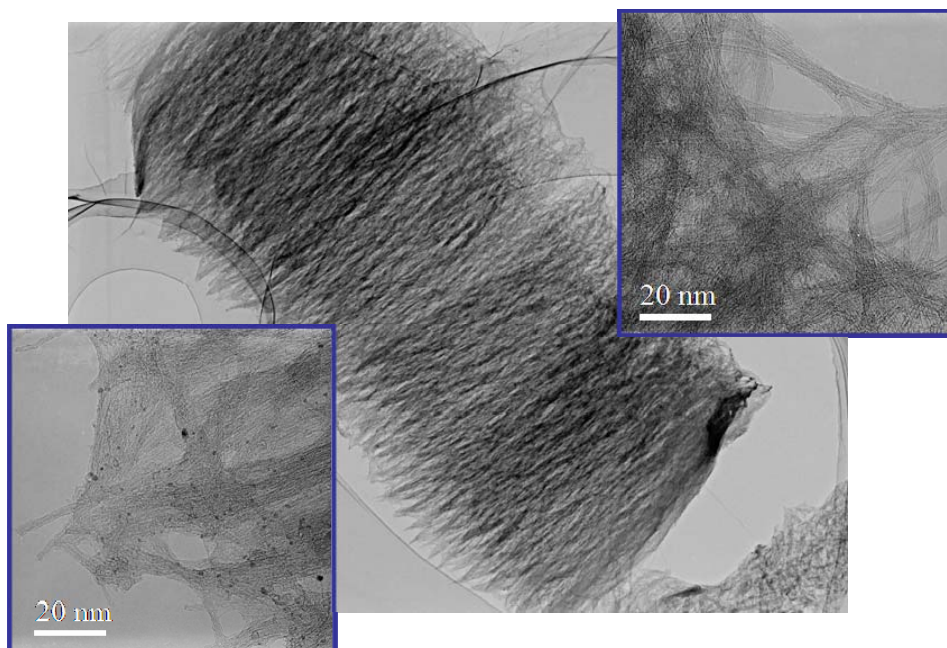


Figure 2-4. Typical TEM image of an aligned SWNT array, where catalyst particles are not found near the root part of the array.

To summarize this section, I succeeded in the growth of ^{13}C enriched, aligned SWNT arrays by no-flow CVD, for which the carbon conversion efficiency from ethanol to SWNTs was as high as 40%. The sequential feeding of two types of isotope-labeled ethanol resulted in the formation of ^{12}C - ^{13}C SWNT junctions, which provided concrete evidence for the root growth mechanism of SWNTs synthesized by ACCVD. Clarification of the root growth model is critical in understanding the growth and catalyst deactivation mechanisms in ACCVD. It also affords better control when producing aligned SWNT arrays with tailored morphologies.

2.3 Diffusion limit or Catalyst deactivation

Vertically aligned carbon nanotube (CNT) arrays grown on flat substrates^[23, 30, 31, 37-39, 87], in which all the nanotubes are of similar orientation and length, offer an ideal platform to study CNT growth mechanisms and kinetics. Since 1996^[37], various chemical vapor deposition (CVD) methods, including floating catalytic CVD^[39], plasma enhanced CVD^[87] and thermal CVD^[38] have been proposed to synthesize aligned multi-walled carbon nanotube (MWNT) arrays. Lately, alcohol catalytic CVD^[23] (ACCVD), water assisted CVD^[30], microwave plasma CVD⁷, etc. are used to produce vertically aligned single-walled carbon nanotube (SWNT) arrays. These processes usually involve different catalysts, carbon sources and operation parameters, resulting in products with different morphologies and qualities. However, none of these CNT growth processes can overcome the gradual deceleration and eventual termination of growth. Two typical growth curve in ACCVD and ferrocene CVD are shown in Figure 2-5. The ability to understand and thereby to overcome the underlying deactivation mechanisms becomes one of the most critical steps to develop nano-scale tubes into real macroscopic materials.

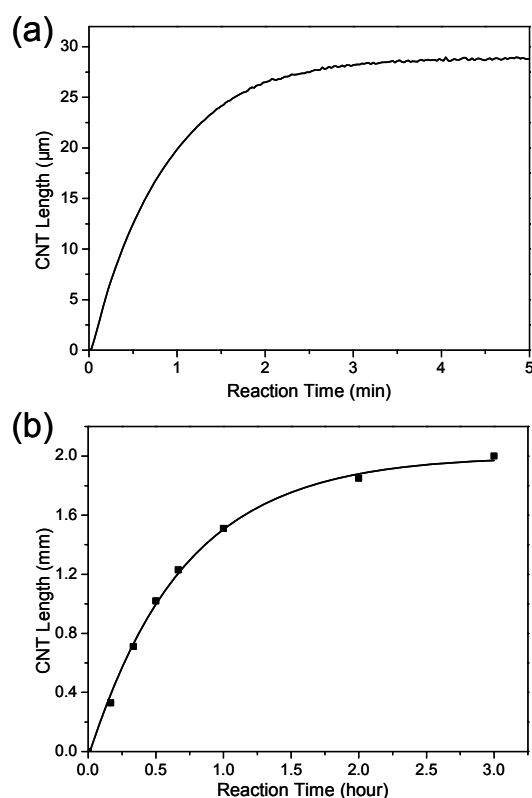


Figure 2-5. Time dependent growth of vertically aligned (a) SWNT arrays from ACCVD and (b) MWNT arrays from floating CVD, both of which show decelerating growth behavior over time.

Recently, many groups have affirmed the root growth mode of their vertically aligned CNTs (including what I found in last section.), indicating that the feedstock molecules have to diffuse through the thick CNT array, reach the substrate where catalysts are located, and then contribute to the CNT growth.^[69, 70, 73, 88] In this bottom-up growth process, the diffusion resistance of the feedstock from the top to the root arises as an obstruction, and can act as a unique decelerating growth mechanism. Existence of a feedstock diffusion resistance means that concentration of the carbon source at the CNT root should be lower than the bulk concentration. Previously, Zhu et al.^[89] fitted experimentally-obtained film thicknesses with the square root of growth time, and stated that the growth deceleration is attributed to the strong diffusion limit of feedstock to the CNT root. However, Hart et al.¹⁵ claimed later that their growth curve can be accurately described by either diffusion limit or catalyst

deactivation, suggesting that only fitting is not sufficient to clarify a diffusion controlled process from a catalyst deactivation controlled (catalyst decay) one. Furthermore, if the process is in the transition region, i.e. not completely diffusion controlled, root square fitting is no longer available. Here, I propose a method of using a non-dimensional modulus to quantitatively evaluate the degree of feedstock diffusion resistance (no diffusion resistance regime, transient regime, and strong diffusion limit regime). ACCVD¹⁶ grown single-walled carbon nanotubes (SWNTs)^{5,17-20} were used as a typical example of this method, and were found to be essentially free of feedstock diffusion resistance. The byproduct back diffusion¹⁹, which has never been taken into account previously, can also be estimated by the present method. Considering the similar diffusion behavior in different CVD processes, five of the most frequently used systems are also discussed. The results agree well with the currently available experimental results.

Vertically aligned SWNTs were synthesized on Co/Mo dip-coated²¹ quartz substrates at 800 °C from ethanol as a carbon source. MWNT arrays were grown on quartz substrates at 800 °C with simultaneous feeding of cyclohexane and ferrocene²². Details of the growth processes can be found in our previous work.^{17,22} The lengths of as-grown CNT arrays were measured by SEM (JSM-7000 and JSM-7401), and average diameters were determined by TEM (JOEL 2010).

2.3.1 General 1D diffusion model

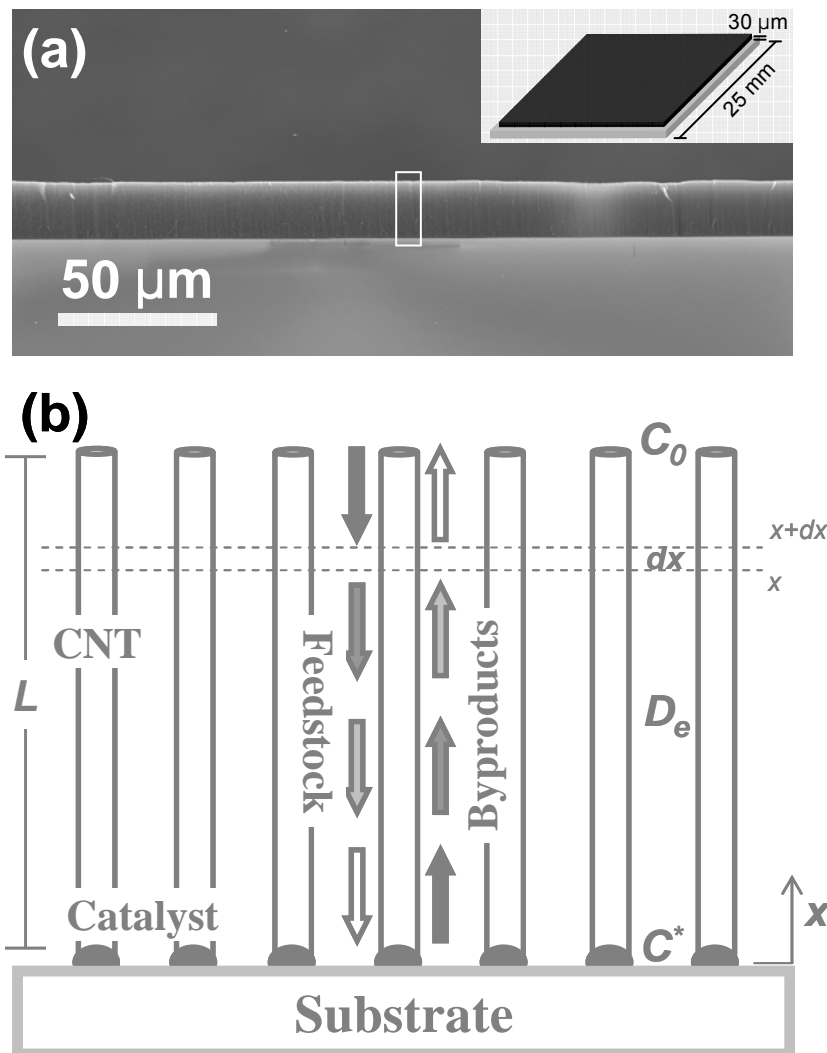


Figure 2-6. (a) SEM micrograph of vertically aligned SWNT arrays from ACCVD, inset at top-right is a schematic of a CNT film on substrate, suggesting the different dimensions of film size and thickness; (b) schematic presentation describing the diffusion of feedstock as well as gas product during the root growth of CNT arrays.

First, it is worth clarifying the concept of diffusion limit that is to be discussed below. Figure 2-6 presents the root growth process of aligned CNT arrays. As carbon source is being decomposed and extruded into solid CNT on catalyst. The concentration of feedstock molecules (e.g. ethanol in ACCVD) at the CNT root, which chemically determined the reaction rate, will be much lower than top (bulk concentration) if feedstock molecules are not

diffusing fast enough from top to root. Similarly, if the byproduct molecules generated by CNT growth can not diffuse fast, their concentration will also be higher at CNT root than near the top. This concentration difference at the root and top of a CNT array is the origin of diffusion limit. Other facts, such as catalyst oxidation, aggregation, reaction with substrate, formation of amorphous soot or graphitic structure on catalyst particles, are attributed to the catalyst poisoning (causing smaller k_s as to be discussed later), although some of them, e.g. soot formation, also prohibit carbon source from reaching catalyst. Also, I only consider one-dimensional diffusion (along the tube axis) inside CNT array. The diffusion from the sides of the forest is neglected because of the following two reasons. First, the side diffusion distance, i.e. the width of the vertically aligned CNT film (~25 mm) is usually much larger than the top diffusion distance, i.e. the film thickness (usually several millimeters at most). Second, side diffusion is probably more difficult due to the higher collision frequency in the anisotropic structure of the vertically aligned CNT array. Therefore, in a small sliced CNT array region dx (as indicated by dashed lines in Figure2-6b), the difference in the amount of feedstock diffusing in from the top and diffusing out from the bottom should be what is consumed inside this dx region. At CNT-substrate interface, although microscopically (at molecular level) not all collisions between feedstock molecule and catalyst can result in CNT growth, the macroscopic net diffusion flux equals to the CNT formation rate (either expressed by the reaction rate $k_s SC^{*m}$ or the macroscopic growth rate $aS dL/dt$) when in equilibrium. Following basic diffusion theory, Fick's Law (diffusion flux is proportional to concentration gradient), and reaction theory^[90], this process can be expressed by

$$D_e S \left(\frac{dC}{dx} \right)_{x+dx} - D_e S \left(\frac{dC}{dx} \right)_x = 0 \quad (\text{inside of CNT forest}), \quad (1)$$

and

$$D_e S \left(\frac{dC}{dx} \right)_{x=0} = k_s SC^{*m} = aS \frac{dL}{dt} \quad (\text{root of CNT forest}), \quad (2)$$

where D_e is the effective diffusion coefficient, S film area, x normal coordinate from substrate, L length of CNT array, k_s surface reaction constant of carbon source to CNT, C^* effective feedstock concentration at the CNT root, m reaction order, and a structure-dependent constant of CNT array. Here, I emphasize that, although CNT growth can be divided into detailed steps, i.e. first feedstock decomposition, then carbon diffusion inside metal and final carbon precipitation, all these steps are treated as together here and k_s is the reaction constant of the overall process from carbon source to CNTs. In other words, k_s represents the dependence of overall CNT growth rate on carbon source concentration. This is also the only growth constant that can be obtained directly from experiments. Equation (1) is solved as $\frac{d^2C}{dx^2} = 0$

or $\frac{dC}{dx} = \text{const}$ and means that the feedstock concentration is linearly decreasing from top to

root, thus, equation (2) can be modified to

$$D_e S \frac{C_0 - C^*}{L} = k_s S C^{*m} = a S \frac{dL}{dt}. \quad (3)$$

Therefore, as soon as I know the reaction order m and the reaction coefficient k_s , the effective concentration C^* can be found from equation (3), and then the time-dependent growth curve can be determined from an integration of equation (3).

Experiments were carried out under different ethanol pressures to investigate the growth order in the ACCVD method. It is found that the initial growth rate is almost proportional to the ethanol concentration²⁰ (see supporting information), suggesting $m = 1$, which is also found to be approximately valid in other processes (e.g. for water assisted super growth^[91]).

If k_s can be constant, the effective concentration C^* is calculated as $C^* = \frac{D_e C_0}{D_e + L k_s}$. Then,

equation (3) becomes

$$a \frac{dL}{dt} = k_s C^* = k_s \frac{D_e C_0}{D_e + L k_s} \quad (4)$$

By integrating equation (4), time-dependent growth curve is deduced as

$$L = \sqrt{\left(\frac{D_e}{k_s}\right)^2 + \frac{2D_e C_0}{a} t} - \frac{D_e}{k_s}. \quad (5)$$

This equation can be proportional to either t (no diffusion limit) or $t^{1/2}$ (strong diffusion limit), depending on the values of $\frac{2D_e C_0}{a} t$ and $\frac{D_e}{k_s}$ (see supporting information). It is similar to what is widely used in silicon oxidation, the so-called ‘‘Deal-Grove’’ relationship^[92], as discussed previously.^[89] One can, in principle, also predict the growth curve of a CNT array provided that all the parameters listed above are known. However, a big difference between growth of a CNT array and silicon oxide is that, in most cases, the catalyst for CNT growth undergoes catalyst poisoning. Therefore, k_s in CNT growth is also a time-dependent parameter, unlike in silicon oxidation, where k_s is constant. This means that equation (5) only predict the ideal growth curve where catalyst activity does not decay.

To enable a simple estimate on the existence of a diffusion limit for a certain system and CNT length, I can define a non-dimensional number φ by

$$\varphi = \frac{k_s L}{D_e}. \quad (6)$$

This number represents physically the ratio of catalytic capability to diffusive capability. Then, the ratio of effective concentration to bulk concentration, η (usually called the effective factor) can be correlated with φ via a simple function from equation (3) as

$$\eta = \frac{C^*}{C_0} = \frac{D_e}{k_s L + D_e} = \frac{1}{\varphi + 1}. \quad (7)$$

This factor allows us to quantitatively characterize the degree of the diffusion limit. When φ is small (e.g. <0.1), it is much easier to diffuse than to react, thus the effective factor will be nearly 1 ($\eta >0.9$), indicating there is little diffusion resistance. In contrast, when φ is large

(e.g. >9), it is more difficult to diffuse than to react, thus the effective factor η will be nearly zero (<0.1) and the overall reaction will be dominated by the diffusion rate. The in-between situation is what I mentioned before as the transition regime, where the growth curve will be proportional to neither t nor $t^{1/2}$.

In ACCVD synthesis, the carbon feedstock at top of the SWNT array is constantly refreshed, and therefore the byproduct concentration can be treated as zero due to the high ethanol flow rate. Thus if I assume that one C_2H_5OH molecule produces one byproduct molecule, e.g. H_2O or H_2 , after decomposition ($A \rightarrow CNT + B + \dots$), the byproduct concentration at the CNT root can be also revealed as a single function of φ ,

$$C_B^* = C_0 \times \sqrt{\frac{M_B}{M_A}} \times \left(\frac{\varphi}{\varphi + 1} \right). \quad (8)$$

According to the above discussion, as long as I know D_e and k_s , the influence of diffusion can be concluded simply from the value of φ for a certain CNT length L . The average diameter of SWNTs produced by ACCVD is about 2 nm, and the density of the as-grown film is about 0.04 g/cm^3 . Therefore, the average distance between adjacent SWNTs can be easily calculated to be 8.8 nm. As the mean free path of ethanol in this process is about 16000 nm, much larger than the distance between SWNTs, it can be concluded that the ethanol diffusion resistance is mainly due to the ethanol-CNT collisions, i.e. in the range of Knudsen diffusion. Thereby, the diffusion coefficient can be estimated from collision theory if assuming CNT tortuosity as diffusion channel tortuosity.^[93] As for k_s , I can use the initial value at $t=0$ when the CNT growth is free of diffusion resistance. With the estimated D_e and experiment-derived k_s , φ is calculated to be 0.054 ($\ll 1$) for 30 μm SWNT arrays in ACCVD. This means the ethanol concentration at the CNT root, where the catalyst is located, is almost the same as the concentration at the CNT top (95% from equation (7)). The vertical distribution of ethanol concentration in the array is plotted in Figure 2-8a as A-SWNT. Thus,

this process is catalyst deactivation controlled rather than diffusion controlled. After I peel the as-grown film off the substrate, most of the catalysts remain on the substrate, but the substrate is not active for a second growth. This confirmed that the catalyst poisoning contributed to the growth deceleration, which agrees with above calculation of ϕ . We know H_2O is a byproduct of ethanol decomposition, estimating through equation (8) reveals the concentration of water at the CNT root is several hundred ppm. Considering the previous report on the critical role of H_2O or O_2 on the growth of SWNT^[30, 32], I plot the concentration distribution of H_2O in Figure 2-8a. This result is interesting, but currently I am not sure if this water concentration is critical for successful SWNT nucleation, or its relation to catalyst deactivation in ACCVD. Further work is needed in this area.

One may notice the above discussion on the feedstock diffusion is versatile and valid for all the first-order growth methods of aligned CNTs, applying to both SWNTs and MWNTs. Therefore, with the available data in the literature, I am able to estimate the degree of diffusion resistance in other CVD processes used to grow aligned CNT forests. The only difference here is when estimating the effective diffusion coefficient for MWNT arrays, the molecular diffusion should also be taken into account because the mean free path is comparable to the inter-tube distance for MWNT arrays, as listed in Tab. 1.

2.3.2 First order reaction confirmed by experiment

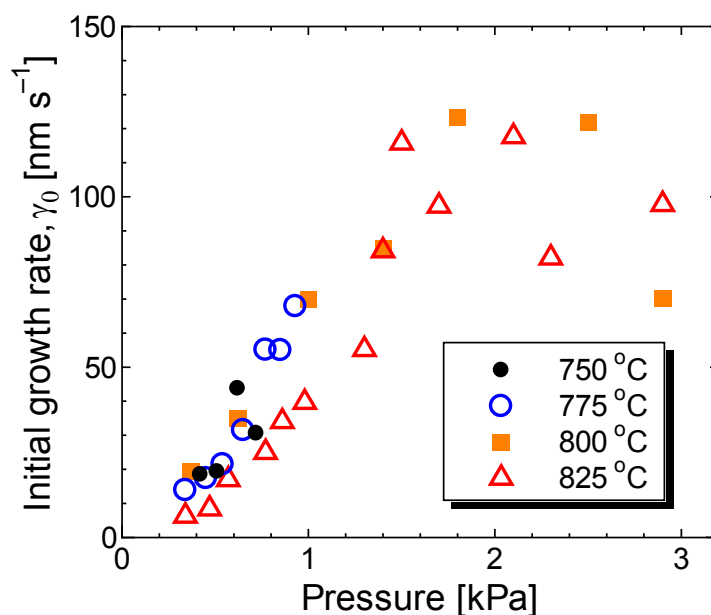


Figure 2-7. Relationship of initial growth rate of aligned SWNT arrays in ACCVD and the feedstock (ethanol) pressure, confirming the approximate first-order growth under different temperatures.

Using the in situ optical absorption technique proposed before, we have studied the effect of pressure on the initial growth rate of SWNTs in ACCVD.^[94] Clearly in Figure 2-6 that the initial growth rate increase almost linearly to the pressure. This indicates that this process is close to 1st order reaction to ethanol pressure and therefore the above discussion should be valid for ACCVD. After carefully checking other processes, I found all existing data are also show 1st order behavior, particularly in low pressure range (which is critical here).

2.3.3 Results for SWNT and MWNT

I analyzed four other CVD processes: a 2 mm MWNT array by floating CVD^[95] (F-MWNT), a 2.5mm SWNT array by super growth by Hata et al.^[30, 91, 96] (S-SWNT), a 2.5 mm SWNT array by microwave plasma CVD by Zhong et al.^[31, 97, 98] (P-SWNT), and a 400 μ m MWNT by thermal CVD by Zhu et al.^[70, 89] (T-MWNT). The results are compared with

our 30 μm SWNT array produced by ACCVD (A-SWNT) in Table 2-1. It can be seen that, k_s and D_e , the two key parameters to determine ϕ , and thus the degree of diffusion difficulty, have quite large difference among various CVD processes, especially between SWNT and MWNT arrays. D_e in SWNTs is usually one order of magnitude lower than that in MWNT because SWNTs are much more densely packed than MWNT (the inter-tube distance is smaller). Reaction constants are obtained experimentally from equation $r=k_sSC$. Larger k_s for SWNT growth is due to the lower carbon source concentration (C) but similar CNT growth rate (r). One possible physical reason for this different growth constant might be the higher catalytic activity for smaller metal particles in absorbing and decomposing hydrocarbon molecules. Because of these differences, it is suggested that, for mm-scale SWNTs, ϕ is usually much larger than 1 and, even if there is no catalyst poisoning, the growth rate of mm-scale SWNT arrays will still drop to only 10% due to the strong feedstock diffusion resistance. However, as the concentration at the root of array is of little difference from the bulk concentration, above 90%, even when there is no catalyst deactivation (if considering a decrease of k_s in real systems, the concentration would be higher), the diffusion resistance seems to not be the dominant reason for the decreasing growth in MWNT arrays. The feedstock concentration distribution in these CNT arrays is presented in Figure 2-8a. As the ϕ is simply L dependent, I can also predict the critical length, as shown in Figure 2-8b, above which diffusion problem begins to take an effect. It seems one might not need to worry about diffusion resistance for MWNTs before one can grow almost 10 cm to 1 m high CNT arrays, unless the diffusion phenomenon inside a CNT array is much different from classic Knudsen theory.

Table 2-1. System parameters and as-calculated φ and η .

Parameters	Abb.	Unit	A-SWNT	S-SWNT	P-SWNT	T-MWNT	F-MWNT
Temperature	T	(K)	1073	1023	873	1023	1073
Molecular weight	M	(-)	46	28	16	28	84
Density	-	(g/cm	0.041	0.037	0.067	0.014	0.082
CNT Diameter	-	(nm)	2	3	2	10	29
Number density	-	(m ⁻²)	8.5E15	5.2E15	1.4E16	3E14	2.1E13
Porosity	ρ	(-)	0.973	0.963	0.956	0.976	0.986
Inter-tube distance	-	(nm)	8.8	10.9	6.5	48	189
Mean free path	λ	(nm)	16000	206	5500	196	91
Growth rate	-	(m/s)	2E-7	3.75E-6	5E-8	1.2E-6	5E-7
Reaction constant	k_s	(m/s)	2.4E-3	9.2E-3	5.7E-3	1.2E-4	3.5E-4
Diffusion coefficient	D_e	(cm ² /	0.013	0.020	0.015	0.085	0.169
Length	L	(mm)	0.03	2.5	2.5	0.4	2
Proposed number	φ	(-)	0.054	11.3	9.7	0.0057	0.042
Effective factor	η	(-)	0.949	0.081	0.093	0.994	0.960

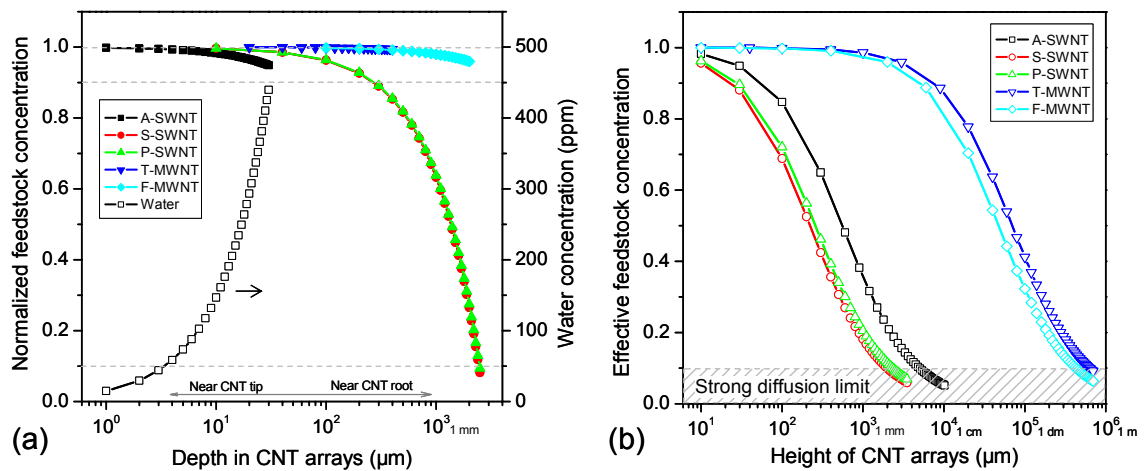


Figure 2-8. (a) Carbon source and by-product concentration distribution in various vertically aligned CNT arrays. A-SWNT: 30 μm SWNT from ACCVD; S-SWNT: 2.5 mm SWNT from water-assisted super growth; P-SWNT: 2.5 mm SWNT from microwave plasma CVD; T-MWNT: 400 μm MWNT from thermal CVD; F-MWNT: 2 mm MWNT from floating CVD; Water: water concentration inside 30 μm SWNT from ACCVD. (b) Relationship of the CNT array height and the effective feedstock concentration at the array root, predicting the critical height above which these various CNT arrays will meet the strong diffusion resistance.

2.3.4 Solution for a diffusion-limited process

From equation (6), the influences of different parameters on the diffusion behavior can be investigated, and strategies to overcome the diffusion limit for the SWNT growth can also be revealed. Increasing D_e and decreasing k_s or L are all possible ways to decrease ϕ . However, the influences of these parameters are very limited because to bring diffusion limited processes to the reaction controlled region one usually needs to decrease ϕ by two orders of magnitude, as expressed in Equation (7). One promising approach is to pattern the continuous CNT film into pillar-like or sheet-like micron structure to allow easy side diffusion, as demonstrated by Zhong et al.^[98] However, I found this strategy didn't work for F-MWNT in yielding longer CNT arrays.^[98] This means there exists strong diffusion resistance in P-SWNT but not in F-MWNT, which agrees well with the above calculated results on these

two situations. One may also notice the edge of the CNT arrays produced by the “super growth” method is usually higher than the center part of the array. This might also be an evidence for the diffusion limit in this process. Besides Zhong’s strategy, gradually increasing the feedstock partial pressure during the growth so as to keep the effective concentration at the CNT root constant might be another way to overcome this diffusion limit caused growth decay.

As to the error in this calculation, it is unavoidable since the influences of some factors, e.g. the bundle structure of SWNTs, the conversion rate of feedstock to CNT, tortuosity of diffusion channel (I assume it to be 1.5 in all cases) are simplified or excluded in the above discussions. However, as mentioned above, error within one order of magnitude in estimate of ϕ will not lead to a significant difference in concluding the extent of the diffusion limit. As the largest error lies on the calculation of D_e , further work on direct measurement of D_e is undergoing. Nevertheless, ϕ is helpful in understanding the role of growth parameters on the diffusion limit and the different diffusion behaviors inside SWNT and MWNT arrays.

To summarize this part, I have presented a versatile model for one-dimensional diffusion during the root growth of aligned CNT arrays. The proposed non-dimensional modulus can be used to quantitatively evaluate the degree of the diffusion limit of feedstock, as well as byproduct molecules. The results show that, for mm-scale SWNT arrays, the feedstock concentration at the root of the array is much lower than the bulk concentration, while for mm-scale MWNTs the decreasing growth can not be attributed to a diffusion limit. The results generated from the model agree well with experiment data. Possible strategies to grow longer CNTs in those diffusion limited processes can be revealed.

2.4 Sub-millimeter long VA-SWNTs from ACCVD

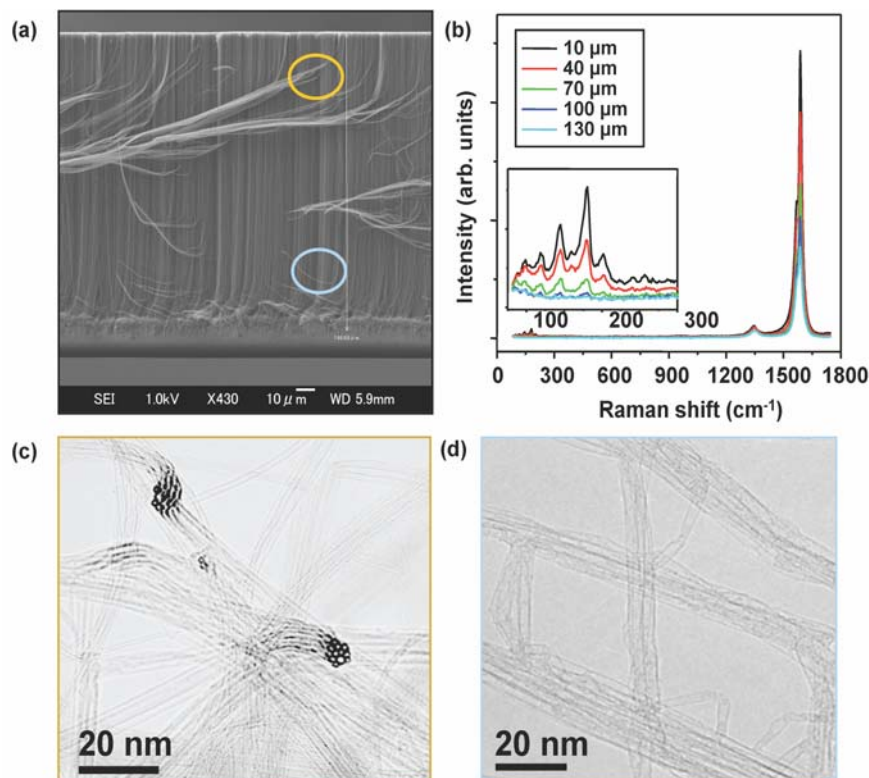


Figure 2-9 (a) SEM image of a VA-SWNT array with thickness of 150 μm obtained by pre-treating the SiO_2 substrate with oxygen plasma prior to dip-coating; (b) resonance Raman spectra (488 nm excitation) from different positions along the array, showing a intensity decrease in G-band and RBM peaks; typical TEM image of SWNTs near (c) top and (d) root of a thick array.

Although the typical height of our VA-SWNT arrays is approximately 10 μm , much taller arrays can be obtained by several approaches. I found that the decomposition of ethanol is critically important for this growth process. The detailed and practical analysis of the decomposition of ethanol is discussed in a published paper.^[99]

An alternative method is the modification of the substrate surface chemistry. Figure 2-9a shows a 150 μm VA-SWNT array synthesized under the aforementioned standard CVD conditions. This was achieved by exposing the substrate to O_2 plasma prior to dip-coating, which resulted in the surface of Si/SiO₂ substrate being terminated by a carboxyl group. Since

the OH-terminated surface is more hydrophilic than an as-delivered, clean, untreated surface, our first speculation was that perhaps more catalyst was loaded onto the surface due to the increased hydrophilicity. However, simply increasing the concentration of the catalyst in the dip-coating solutions and using an un-treated surface resulted in no significant growth promotion. This is probably because of the chemisorbed state of our metal acetate molecules onto specific surface sites.^[27] The surface concentration of metal atoms is very weakly dependent on the concentration of the solution, as seen in Figure 1(b) where the concentration was changed by two orders of magnitude.

Though the mechanism is still not well understood, the successful synthesis of long (> 100 μm) SWNTs is consistent with the conclusion made in the previous section. Catalyst deactivation rather than the diffusion is the rate controlling step in the growth of our SWNTs.

2.5 Summary

This chapter is to understand what causes the growth decay and how to achieve sustained grown long SWNTs. I have presented the successful synthesis of aligned ^{13}C labeled single-walled carbon nanotube (SWNT) arrays from alcohol by a modified no-flow chemical vapor deposition (CVD) method that makes efficient growth possible using a small amount of carbon source. The synthesis of high-quality SWNTs by this alternative method was confirmed by resonance Raman spectroscopy, which also showed that the quality of the grown SWNTs is uniform in growth direction. The synthesis of ^{13}C labeled SWNTs provides solid evidence for the root growth mechanism in alcohol catalytic CVD, which agrees well with the transmission electron microscopy (TEM) observations

After confirming the root growth mechanism, Feedstock and byproduct diffusion in the root growth of aligned carbon nanotube arrays is discussed. A non-dimensional modulus is proposed to differentiate catalyst-poisoning controlled growth deceleration from one which is diffusion controlled. It is found that, at current stage, aligned multi-walled carbon nanotube

arrays are usually free of feedstock diffusion resistance while single-walled carbon nanotube arrays are already suffering from a strong diffusion resistance. The method presented here is also able to predict the critical lengths in different CVD processes from which carbon nanotube arrays begin to meet strong diffusion resistance, as well as the possible solutions to this diffusion caused growth deceleration.

Chapter 3 Growth acceleration and ethanol decomposition

This chapter deals with several phenomena that are later found crucial to the quality of SWNTs grown. First, addition of only 1% of acetylene into ethanol was found to enhance the growth rate of single-walled carbon nanotubes (SWNTs) by up to ten times. This accelerated growth, however, only occurred in the presence of ethanol, whereas pure acetylene at the same partial pressure resulted in negligible growth and quickly deactivated the catalyst. The dormant catalyst could be revived by reintroduction of ethanol, indicating that catalyst deactivation is divided into reversible and irreversible stages. Since the thermal decomposition of ethanol also yields some amount of acetylene, the possible contribution to the formation of SWNTs from these decomposed gases is also discussed. The effect of carbon precursor on the quality of SWNTs obtained is also demonstrated.

3.1 Background and motivation

The excellent properties of single-walled carbon nanotubes (SWNTs), particularly chirality-dependent electrical conductivity,^[2] make them one of the most exciting materials in nanoscience and nanoengineering. Accordingly, many potential applications of SWNTs have been proposed.^[100] After the successful synthesis of random SWNTs by various methods,^[19-21] the focus shifted to assembling these one-dimensional tubes into vertically-aligned arrays, which offer at least two intrinsic advantages. First, aligned arrays possess preferable and sometimes unique properties, such as anisotropic electrical and thermal transport, and polarization-dependent optical absorption.^[47] These anisotropic materials have the potential for improving performance in existing applications or the development of novel applications.

Patterned field emission arrays,^[38] continuous carbon nanotube (CNT) yarns,^[51] high thermal conductive polymer composite,^[41] super-compressive cushion material,^[101] multi-functional nano-channel filter^[102, 103] have been achieved using vertically aligned multi-walled carbon nanotubes (MWNTs). The other intrinsic advantage of an aligned array is that it offers an ideal platform to study the growth mechanism and kinetics, as reported before^[86, 91, 104] and to be further discussed in this article. This is because all the SWNTs have lengths approximately equal to the height of the array.

Historically, the first vertically aligned MWNT array was synthesized in 1996.^[37] However, it was not until recently that vertically-aligned SWNT arrays were obtained, first from alcohol catalytic chemical vapor deposition (ACCVD),^[23] and followed soon after by many other methods including water-assisted CVD,^[30] microwave plasma CVD,^[31] and hot-filament CVD.^[32] Recent investigations have also improved our understanding of SWNT growth behavior.^[74, 86, 91, 105, 106] We previously developed an *in situ* optical absorption measurement that allows for convenient real-time measurement of the film thickness.^[74] This technique revealed, for the first time, *in situ* growth kinetics of a VA-SWNT array. It provided sub-second resolution and much more direct information to the previously black-box approach to studying the growth process. The *in situ* measurement setup is shown in Figure 3-1a, where a laser is passed through the SWNT array, and the thickness is determined from the absorption. Figure 3-1b shows a typical growth curve obtained from this technique. The SWNTs grow very fast at the beginning but the growth rate decreases with time, effectively stopping within 10 min. The diminishing growth rate can be fitted almost perfectly by an exponential decay, which can be expressed in terms of an initial growth rate and a decay time constant.^[104] The detailed influences of CVD parameters, such as temperature and growth pressure, have been reported elsewhere.^[94]

Here I investigate the influence of various species on ACCVD synthesis of VA-SWNTs. A small amount of acetylene (approximately 1% partial pressure) was found to accelerate the

growth rate by almost ten times, as revealed by a distinct change in the growth rate determined from *in situ* optical absorption. Additionally, the inherent contribution of acetylene, which can be produced by thermal decomposition of ethanol, to ACCVD is also quantitatively investigated.

Vertically aligned SWNTs were synthesized at 800 °C using ethanol as a carbon source and a Co/Mo combination as a catalyst.^[27] The catalyst was dip-coated onto quartz using a two-step procedure, as described in our previous work.^[94] The substrate was then annealed in air at 400 °C for 3 min before heated to 800 °C under a 300 sccm Ar/H₂ flow (3% H₂, Ar balance) at a pressure of 40 kPa. Upon reaching the growth temperature, the Ar/H₂ flow was stopped and 450 sccm of ethanol was introduced at 1.3 kPa to start SWNT growth. Additive species, typically acetylene at 0.3 to 14 sccm, were introduced 30 s (long enough to estimate the growth rate before the turning point on a growth curve) after the introduction of ethanol. The growth behavior was monitored *in situ* by passing a 488 nm laser through the quartz substrate, as shown in Figure 1a, and the thickness of the SWNT array was determined from the real-time absorption measurement.^[74] The as-grown samples were characterized by SEM (JEOL 7000F, operated at 3 kV), TEM (JEOL 2000EX, operated at 120 kV), and Raman spectroscopy (488 nm excitation).

3.2 Acetylene accelerated ACCVD

3.2.1 Effect of different species

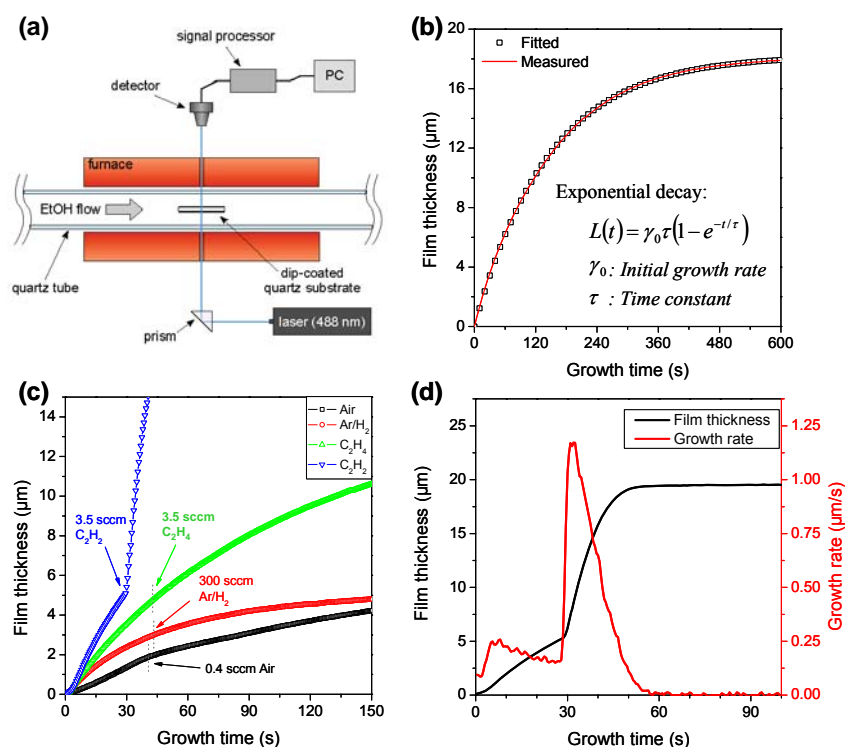


Figure 3-1. (a) Schematic of in situ optical absorption measurement; (b) a typical growth curve obtained from optical absorption, which can be fitted by an exponential decay; (c) influence of various additive species on the growth of aligned SWNTs; (d) VA-SWNT film thickness (black line) and growth rate (red line) showing acceleration of SWNT growth by addition of acetylene.

The influence of various additive species on SWNT growth was determined by introducing different gases into the growth stage of a SWNT array. Using the *in situ* absorption measurement technique was very convenient and straightforward because the effect of additive species is quickly and directly obvious by how they change the growth rate. With this method, the influence of different precursors should be apparent immediately after their introduction, at a known catalyst condition. This gives more reliable results than any *ex situ* methods where catalyst activity may vary among different substrate CVD runs. Several typical examples are presented in Figure 1c. The ethanol flow rate for all cases was 450 sccm

(standard cubic centimeters per minute). When 0.4 sccm of air ($< 0.1\%$ of the ethanol flow) was introduced into the chamber, the growth rate decreased slightly, but was not completely terminated. Similar results were observed for the addition of water ($\leq 5\text{ vol}\%$) into the ethanol. This confirms the robustness of our ACCVD; possible leaks and small amounts of impurities in the precursor will not cause complete failure of SWNT formation, but only affect the final SWNT yield.

3.2.2 Acetylene acceleration

Addition of 300 sccm of Ar/H₂ (3% H₂) resulted in neither acceleration nor deceleration of the growth. The synthesis reaction was, however, very sensitive to the addition of even a small amount of acetylene. Figure 3-1c shows a clear growth enhancement resulting from the addition of only 3.5 sccm acetylene (0.8 vol%). As the derivative of the growth curve gives the growth rate (Figure 3-1d), it is clear that, within seconds, the growth rate increased from 0.15 to 1.2 $\mu\text{m/s}$, an eightfold increase. There was no noticeable change, however, from the addition of a similar amount of ethylene (Figure 3-1c) or methane (not shown), two popular carbon sources used for SWNT growth.

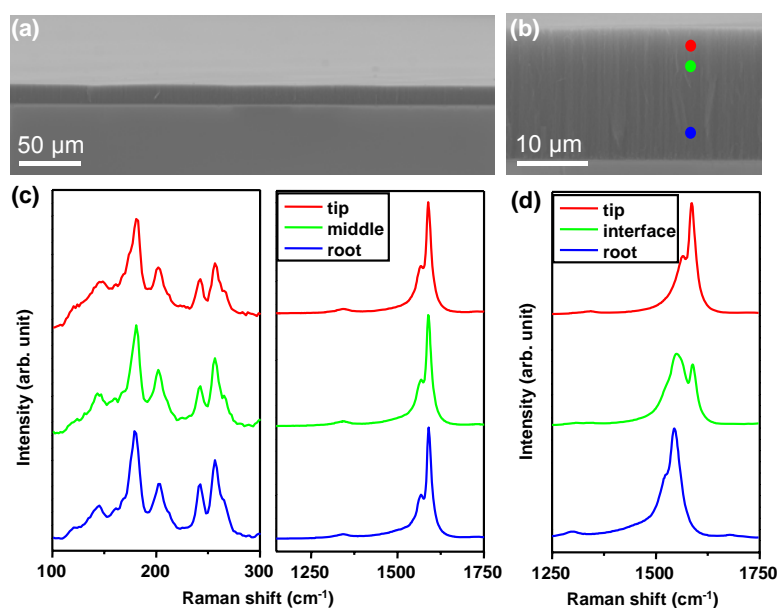


Figure 3-2. SEM images of as-grown SWNT arrays from ACCVD boosted by (a) 12C acetylene and (b) 13C acetylene; (c) Raman spectra taken from different positions of an acetylene-accelerated SWNT array, showing almost identical G-bands and radial breathing mode peaks; (d) G-band of a SWNT array accelerated by 13C acetylene.

Figure 3-2a shows a typical SEM image of an acetylene-accelerated VA-SWNT array. The SWNTs are well-aligned, and the thickness ($\sim 20 \mu\text{m}$) agrees well with the estimate from laser absorption. Since the acetylene was introduced when the array had reached $5 \mu\text{m}$ in height, the upper $5 \mu\text{m}$ of the aligned SWNT array was produced from ethanol, and the remaining $15 \mu\text{m}$ primarily from acetylene. The VA-SWNT array shown in Figure 3-2b was synthesized in a similar fashion, and a similar growth enhancement was observed. In this case, however, isotope-modified 1,2-¹³C acetylene was used. To characterize the quality of these SWNTs, Raman spectra were obtained from different positions along the cross-section of the SWNT array. For normal acetylene (Figure 3-2c), similar spectra were obtained from the upper 1/4, the center, and the lower 1/4 of the array. TEM observation also confirmed that the arrays consist of SWNTs with little amorphous carbon and no MWNTs. As there is no significant difference, in the different regions, it is probable that there was no interruption of growth when acetylene was introduced, and the SWNTs maintained their original

chiralities.^[107] For the isotope-modified case (Figure 3-2d), however, a shift of all Raman peaks was observed in the lower part of the SWNT array, due to the reduced phonon energy caused by the introduction of the heavier ^{13}C isotope.^[84] The G-band shifted from 1590 (^{12}C) to 1544 cm^{-1} , which suggests a ^{13}C content of over 80%. This again illustrates the high reactivity of acetylene.

3.2.3 Possible mechanism

The first question that arises regarding this acetylene-boosted growth is whether acetylene alone can grow SWNTs at similar low concentrations but in the absence of ethanol. To test this I performed CVD with pure acetylene at the same low pressures as when ethanol was present. The results are presented in Figure 3-3a, and are compared with a typical ethanol CVD case. The growth curves suggest some carbon deposition, but the reaction stopped within 20 s. Although Raman spectroscopy confirmed the presence of well-graphitized carbon (spectra not shown), the yield was negligible when compared to conventional ACCVD. This shows that ethanol is necessary to initiate growth, which can later be accelerated by acetylene.

The next natural question which arises is whether or not acetylene can sustain growth initiated by ethanol. This was investigated by introducing the gases in different stages, as shown in Figure 3-3b. SWNT growth was initiated by ethanol (blue line), and maintained for 30 seconds. The ethanol was then stopped and the chamber evacuated, followed immediately by introduction of acetylene (red line). The acetylene initiated a very small growth spurt, but the catalyst quickly became inactive. This indicates that ethanol is necessary throughout the entire growth process, both for cap formation and to sustain growth. Interestingly, reintroduction of ethanol in addition to the already-present acetylene (purple line in Figure 3-3b) recovered the activity of the acetylene-poisoned catalysts, despite showing no signs of activity for more than 60 seconds. Longer exposure to pure acetylene was found to reduce the

degree to which the catalyst could be recovered by reintroduction of ethanol, with recovery being impossible after more than five minutes.

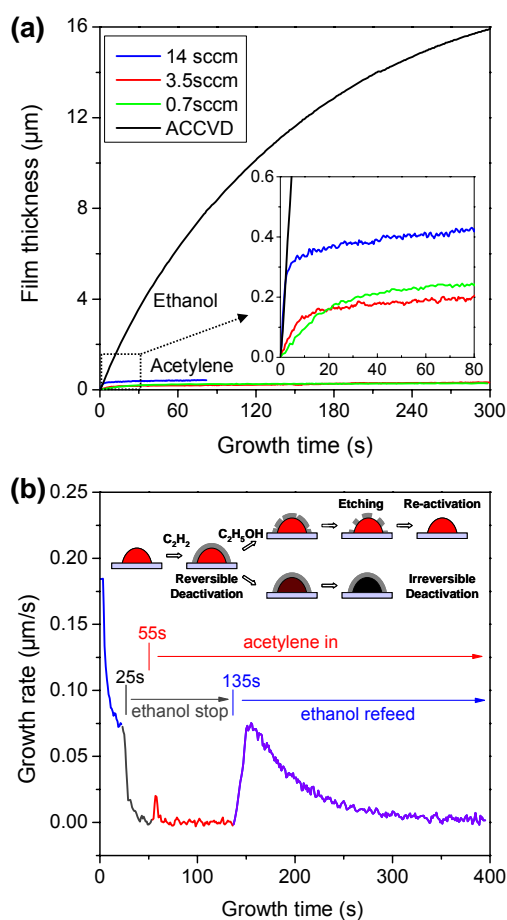


Figure 3-3. (a) Growth curves of CVD with pure acetylene at different flow rates showing almost negligible yield and fast poisoning of the catalyst; (b) CVD started with ethanol but continued with pure acetylene, showing similar fast catalyst deactivation, but the activities of those apparently deactivated catalysts could be recovered by ethanol. A possible schematic presentation of this deactivation and re-activation process is shown as an inset.

The high reactivity of acetylene is not surprising, but it is interesting that in this case it cannot work alone, and that ethanol can recover the deactivated catalyst. One possible mechanism causing this catalyst deactivation by acetylene and re-activation by ethanol is shown in the inset of Figure 3-3b. It is now widely realized that O-containing species like alcohol,^[16, 108] H_2O ,^[30] CO_2 ,^[109] can prolong the catalyst lifetime and significantly increase the yield when hydrocarbons are used as the carbon sources to grow SWNTs. The mechanism is

believed to be the ability of those O-containing species in removing soot structures formed on the catalyst. Recent direct TEM imaging of the metal particles unambiguously showed that carbon coating deactivated the catalyst and H₂O may remove this coating.^[110] Therefore, in the current case, when acetylene is used but ethanol is absent, acetylene may generate considerable amount of amorphous carbon coating on the catalyst, which prohibits further interaction between carbon source and catalyst. Something more I can learn from this experiment is that there might be two stages of deactivation. First, when ethanol stops and a carbon layer forms quickly, the catalyst is likely only inactive rather than completely deactivated. The inactive catalyst could be recovered by removing this amorphous carbon coating. However, after prolonged exposure to such a highly-reactive carbon source and a high-temperature environment, this amorphous layer may form a more stable graphitic layer, or form a carbide particle, after which the catalyst would become irreversibly deactivated, and could not be recovered by exposure to ethanol. According to our experience, the time needed for this irreversible deactivation is several minutes. I suspect this process because at our growth conditions, ethanol is believed to efficiently remove amorphous carbon,^[16] but does not damage graphitic carbon, e.g., SWNTs.^[104] Additionally, as long as there is no carbon source available to the catalyst, e.g., in an Ar/H₂ atmosphere, the catalyst can be kept active at CVD temperatures for 60 minutes or longer. This effectively rules out catalyst-substrate interactions or aggregation of metal particles^[111] as potential deactivation mechanisms.

3.2.4 Revealing other reaction pathways to SWNTs

The concentration of acetylene in the present work is approximately 10 Pa, which is much lower than most previous studies. However, when changing the flow rate of acetylene, I found only 0.35 sccm acetylene (1 Pa) was needed to double the growth rate of 1.3 kPa of ethanol. Quantitatively, the efficiency of collisions between ethanol molecules and catalyst

nanoparticles (k_1 reaction constant) is at least 1000 higher than those involving acetylene molecules (k_2). The growth enhancement factor, defined as $(R_{ethanol+acetylene}/R_{ethanol})-1$, is shown in Figure 3-4a, and increases almost linearly at very low acetylene partial-pressure. This indicates that SWNT growth in conventional ACCVD is limited by surface reactions rather than carbon diffusion in/on the metal nanoparticle, as the catalyst clearly have potential to produce SWNTs at a much faster rate.

As most feedstock species undergo some degree of thermal decomposition before reaching the catalyst, understanding the reaction pathway and the actual reacting species are important in improving understanding of the CVD processes and control over the final SWNT product. The primary byproducts of ethanol thermal decomposition at 800 °C are ethylene and water,^[112, 113] but existing of small amounts of acetylene is also predicted by CHEMKIN and further supported experimentally by our FT-IR results (to be discussed later). Since acetylene has shown to be highly active, even in very low concentration, the apparent activity of ethanol may come partly from acetylene, thus one must consider is a third possible reaction pathway, with rate k_3 , in Figure 3-4a. Also, although ethylene is not as active as acetylene, as the main product from the decomposition, ethylene is around two orders of magnitude more concentrated than acetylene. The possibility of ethylene or even some radicals (though they are really low in concentration and easy to collide and react with SWNT walls when diffusion inside the array) as other hidden precursors should not be excluded. More work is needed to quantitatively determine the contribution by these indirect pathways to SWNT synthesis.

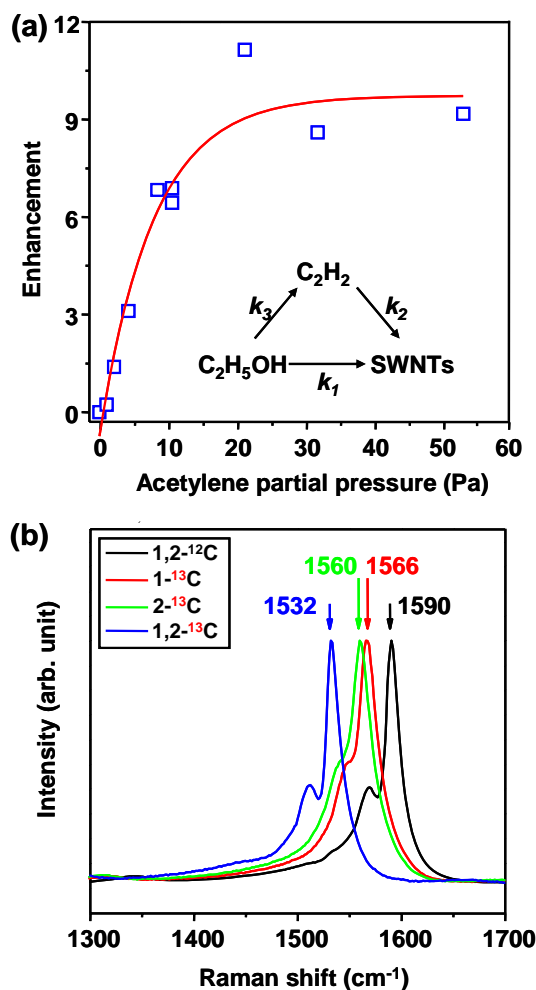


Figure 3-4. (a) Influence of the acetylene flow rate on the degree of growth enhancement, as only about 0.1% of acetylene can reach similar growth of 450 sccm of ethanol; (b) Raman spectra of SWNTs grown from four types of ethanol with different isotope configurations, showing that the second carbon contributes more to SWNT formation. This confirms that not all SWNTs form from decomposed ethanol.

Then the next important question is whether or not ethanol always needs to decompose into acetylene or ethylene in order to grow SWNTs. The following isotope experiment confirmed that ethanol is not a starting material merely but also contributes to the formation of SWNT directly. The ratio of the contribution between ethanol and decomposed gas (acetylene or ethylene) can be even adjusted.

Since ethanol has an asymmetric molecular structure, labeling the two carbon atoms by using isotopes makes it possible to qualitatively determine the contribution of acetylene or ethylene to SWNT synthesis. I synthesized SWNTs using normal 1,2- ^{12}C ethanol and three

isotope-modified versions: 1-¹³C, 2-¹³C, and 1,2-¹³C ethanol. Using a no-flow condition,^[105] where a fixed amount of ethanol is sealed in the chamber and therefore has sufficient time to decompose before forming SWNTs, Raman spectra indicate that 2-C (the carbon atom opposite the OH group, ~55%) contributes slightly more than the 1-C (~45%) to the final product (Figure 3-4b). Both acetylene and ethylene are produced by breaking the C-O bond in ethanol, and are perfectly symmetric in structure thus are expected to have equal contribution from the 1-¹³C and 2-¹³C. This result indicates that ethanol is directly reacting with the catalyst in ACCVD, and is not simply the starting material. The contribution from ethanol increases when using the standard constant-flow case, and the unequal contribution of two different carbon atoms becomes even larger (~70% 2-C incorporation into the final product)^[114] using a fast-flow condition (*e.g.*, by injecting through a nozzle). This is expected, as the faster flow reduces the degree of thermal decomposition prior to arrival at the catalyst, and confirms that the ratio of the various chemical pathways to SWNT formation is altered by the extent of ethanol decomposition. Therefore, it appears here that at different flow rate, the formation of SWNTs follow different pathways due to the different gas composition around the catalyst. In order to understand this process better, it would be helpful to have some quantitative analysis on the decomposition ethanol, which determines the catalyst atmosphere.

3.3 Thermal decomposition of Ethanol

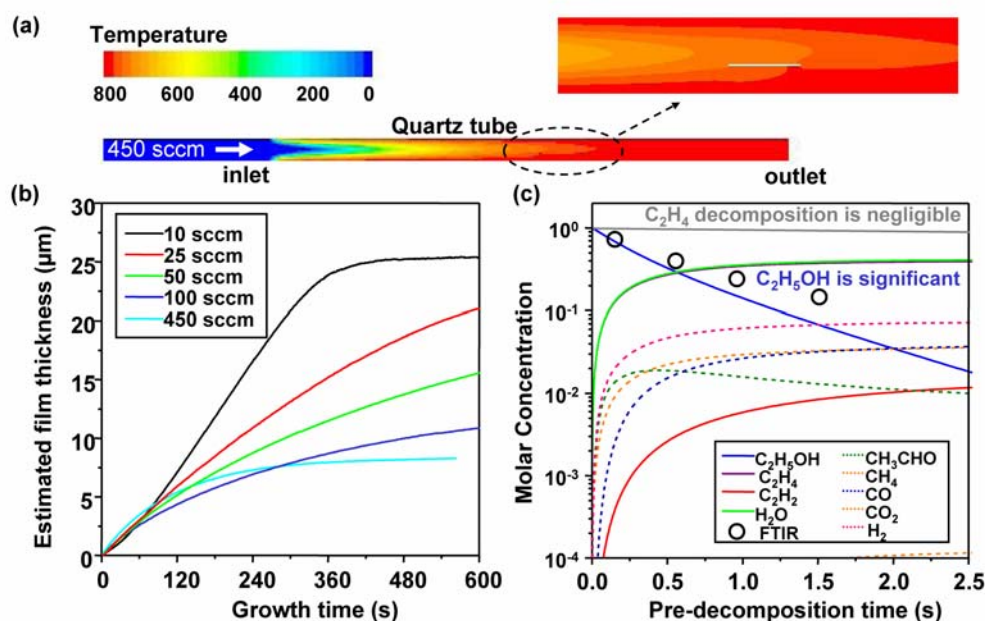


Figure 3-5 (a) Temperature distribution inside the quartz tube during CVD. (b) Growth curves at 800 °C for different ethanol flow rates show a change for slow flow rates. (c) Ethanol decomposition curves calculated by CHEMKIN, and experimentally measured ethanol concentrations (circles) by FTIR spectroscopy.

We have previously investigated the influence of CVD temperature and pressure on the synthesis of VA-SWNTs by ACCVD.^[75] However, since ethanol thermally decomposes at typical growth temperatures,^[115] the actual catalyst environment can be significantly affected by the gas flow rate, even when the furnace temperature is unchanged. Figure 3-5a shows the temperature profile based on a numerical calculation using the FLUENT software package for an ethanol flow rate of 450 sccm through a 60 cm furnace maintained at a temperature of 800 °C. The dashed oval indicates the position of the substrate, and is found to be approximately 20 °C cooler than the furnace temperature. Thermal decomposition of ethanol under these conditions was also calculated, and the concentrations of ethanol and various chemical species produced by its thermal decomposition are shown in Figure 3-5c. Under these conditions,

ethanol almost completely decomposes in 2.5 seconds. The residence time in the chamber, however, is only 0.1 s, thus the ethanol concentration near the catalyst should be more than 90%. In the case of a slower flow rate the gas would be heated to the furnace temperature by the time it arrives at the substrate (due to the shorter entrance length), thus slightly increasing the local temperature at the catalyst. Much more importantly, a slower flow would increase the residence time of ethanol in the heated region. As a result, a more significant portion of the ethanol would have thermally decomposed before reaching the catalyst. This is evidenced experimentally by the growth curves presented in Figure 3-5b, which correspond to different ethanol flow rates under otherwise identical conditions. As the flow rate decreases the catalyst lifetime increases significantly, enhancing SWNT growth. This is likely due to an increase in the production of C_2H_4 and H_2O . In most cases the general growth behavior is typical exponential decay,^[75] but when the flow rate is very slow (i.e., <25 sccm) the growth process changes significantly, as shown by the topmost black curve in Figure 3-5b. In this case the growth rate is nearly constant for approximately three minutes and then suddenly stops. This catalytic sudden-death has been reported elsewhere,^[72, 77, 116] but the mechanism still remains as an open question in this field.

Since the calculation is well supported by the distinct growth curves at different flow rates, I have been convinced that the decomposition of ethanol plays an important role on the local catalyst environment and therefore the growth kinetics or even the SWNTs grown.

To verify the calculation results by CHEMKIN, I measured experimental the gas composition using FTIR. Typical spectra of ethanol decomposed for different time (controlled by different ethanol flow rate) are shown in Figure 3-6. It is of no doubt that acetylene is one of the products of ethanol decomposition. Hence, acetylene must be contributing to the SWNT formation. However, ethylene, though much less active than acetylene, is one of the main products. If neglecting the effects of trace amount of radicals, ethanol, ethylene and acetylene must be the most important three precursors in ACCVD.

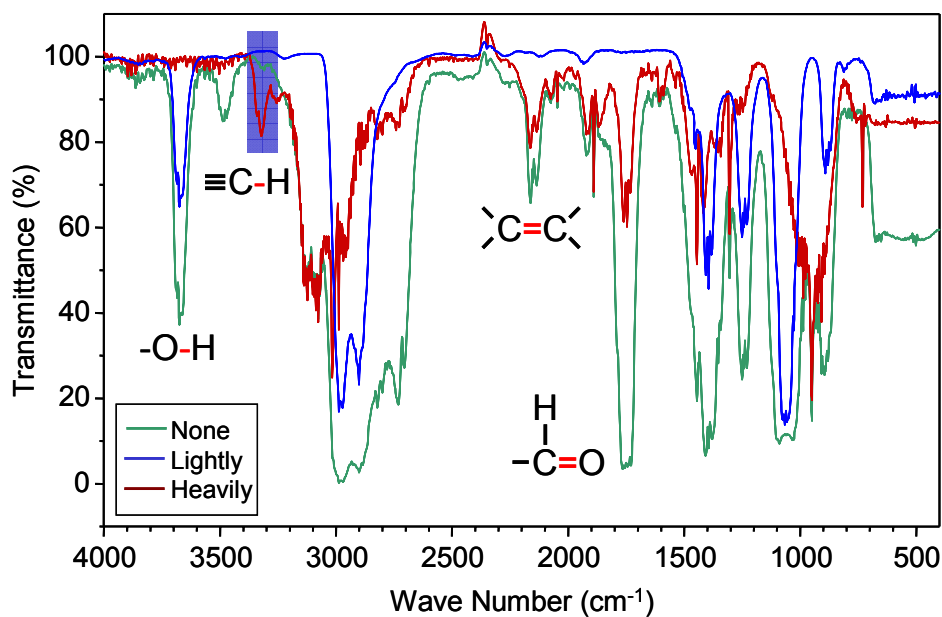


Figure 3-6. Experimental FT-IR spectra of ethanol with different decomposition degree (none, lightly, and heavily decomposed), showing acetylene is one of the products from thermal decomposition of ethanol in typical CVD conditions.

I also find that in the low-flow and no-flow cases, when ethanol is thoroughly decomposed, the SWNTs contain more amorphous carbon than those formed more directly from ethanol, as shown in Figure 3-7. Further work is needed to fully understand the difference between various precursors and quantify their contributions.

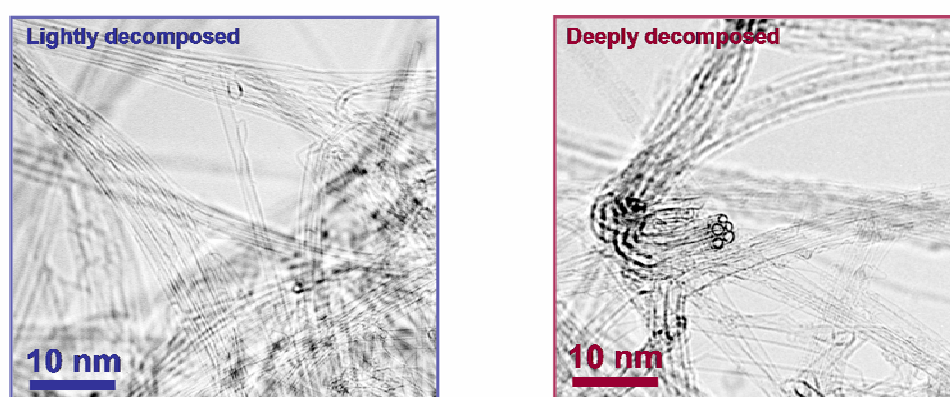


Figure 3-7. Typical TEM images of SWNTs grown from lightly and heavily decomposed ethanol.

3.4 Summary

In summary, I investigated acetylene-acceleration of ACCVD, in which a small concentration of acetylene in addition to ethanol was found to significantly enhance the growth rate of SWNTs. The very high activity of acetylene (estimated to be 1000 times that of ethanol) also suggests a possible fast chemical pathway from ethanol to SWNT formation. However, this fast growth only occurred in the presence of ethanol; pure acetylene at the same partial pressure resulted in negligible growth, deactivating the catalyst in a few seconds. However, these dormant catalyst particles could be reactivated by reintroduction of ethanol. This indicates that catalyst deactivation is divided into reversible and irreversible stages, and also shows the ability of ethanol to preserve catalyst activity throughout the synthesis process. As thermal decomposition is common to almost all CVD systems, it is important to understand quantitatively which species are actually present and their respective roles in contributing to SWNT growth. Further investigation in this direction should not only result in a more complete understanding of the synthesis and catalyst deactivation mechanisms, but also better control of the entire synthesis process.

Chapter 4 Diameter control of VA-SWNTs

In this chapter I demonstrate the ability to tune the average diameter of vertically-aligned single-walled carbon nanotubes (VA-SWNTs) between 1.4 and 2.5 nm by modifying the catalyst recipe. This was achieved by changing both the relative and absolute amounts of Co and Mo in our bimetal catalyst, with an abundance of Mo promoting the synthesis of SWNTs with smaller diameters. I also find that the diameter distribution is not uniform throughout the array, and increases with longer synthesis time. This is confirmed by resonance Raman spectroscopy, TEM observations, and decomposed optical absorption spectra, which reveal the absorption contribution from different portions of a VA-SWNT array.

4.1 Background and motivation

The single-walled carbon nanotube (SWNT) is the most promising material candidate for future devices and novel applications due to its chirality-tunable electron conduction and outstanding mechanical and transport properties.^[2, 81] Many efforts have been made^[19-21, 23, 117, 118] to synthesize SWNTs with controlled structure and morphology. Among the methods that have been proposed, chemical vapor deposition (CVD) possess great potential in terms of scalability and good control over the product,^[21] thus has become the dominate method for SWNT synthesis.

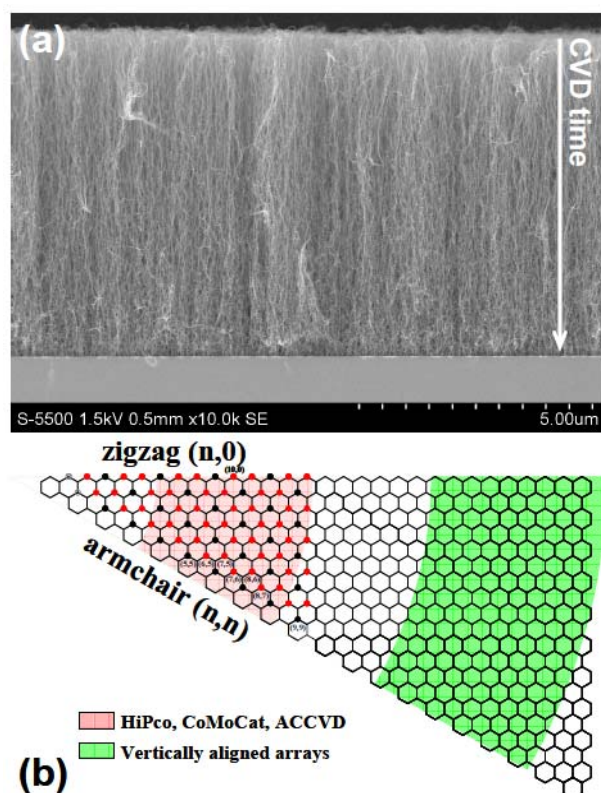


Figure 4-1. (a) A typical SEM image of a vertically aligned SWNT array grown on a quartz substrate. The clear morphology evolution can be noticed; (b) A graphene lattice showing the chirality range of typical random (indicated in red) and vertically aligned (indicated in green) SWNTs.

The diameter of a SWNT affects its mechanical, chemical and especially electronic or optical properties.^[119] SWNTs with smaller diameters (approximately 1 nm) have a larger band gap and are more mechanically stable than larger SWNTs (e.g. dia. >2 nm). Furthermore, they are also more easily measurable by spectroscopic methods such as resonance Raman spectroscopy and photoluminescence excitation.^[118] Various CVD techniques such as HiPco^[22], CoMoCat, and ACCVD^[16] have been successful in producing SWNTs with diameter around 1 nm, and these samples have been widely used as standard samples in SWNTs. However, most vertically-aligned SWNT arrays produce SWNTs synthesized to date have the average diameter of ~ 2 nm.^[23, 30-32] or even larger (~ 3 nm). Although such large-diameter SWNTs may have advantages in some applications, both the

optical and electronic applications become more difficult as the diameter becomes larger (namely, as both oscillator strength and electronic bandgap become smaller). There have been several attempts to control the diameter of vertically aligned SWNTs by changing the catalyst preparation or CVD parameters.^[33, 120, 121] These previous works were successful in changing the diameter to some extent, but primarily in the range of 2 nm or larger.

The difficulty of diameter control lies not only in the synthesis but also the characterization. Resonance Raman spectroscopy is a powerful tool since the peak frequency of the radial breathing mode (RBM) is uniquely determined by the SWNT's diameter. However, unless a wide range of excitation energies are used, Raman spectra contain only limited information about the true diameter distribution in bulk SWNTs due to the following two mechanisms: First, the Raman scattering intensity from SWNTs is strongly dependent on the diameter. Specifically, it decreases as the diameter becomes larger due to the squared dependence on the oscillator strength that is inversely correlated with the diameter.^[122] Second, the Raman scattering process is resonant process, hence investigates only limited chirality SWNTs that are in resonance with the incident light energy. Photoluminescence has proved to be a useful technique for identifying the specific chiralities of SWNTs. However, this technique is limited only to semiconducting SWNTs, and more importantly, the sample preparation step (ultrasonication and ultracentrifugation) in general changes the chirality and diameter distribution in the original sample. For the purposes of overall characterization, optical absorption is less diameter and chirality dependent than other methods, giving more comprehensive information of the true diameter distribution. In this work, I show that the average diameter of vertically aligned SWNTs can be arbitrarily tuned between 1.4 and 2.5 nm by adjusting the catalyst recipe. The average diameter was determined by optical absorption spectra as well as high-resolution TEM observations. I also show that the diameter of SWNTs along the growth direction is not uniform, as evidenced by carefully decomposed

optical absorption spectra. TEM observations and Raman spectra obtained from different locations along the height of the array are consistent with the absorption results. These results provide insight into the SWNT growth mechanism and catalyst behavior on a flat substrate.

4.2 Quantitative evaluation along a SWNT array

4.2.1 Cross-sectional Raman scan

The advantage of a VA-SWNT array not only lies in the anisotropy of its properties, but it also provides a nice platform to study the growth process of SWNTs. Much work related to the formation mechanism and growth kinetics has been demonstrated.^[68, 74, 76, 123, 124] Vertically aligned SWNTs normally obey a root growth mechanism,^[68, 69, 71, 86, 105] and an exponential decay of the growth rate has been reported for different methods. It has also been reported that the morphology and quality of the SWNTs can change along the array,^[77, 125] indicating that the catalyst may be changing during the CVD process.

In the high-resolution SEM image of a typical sample shown in Figure 4-1a, it appears that the upper portion of the array (which grows first) is better aligned than the root, which has also been seen previously. This difference is much more obvious in higher magnification images where the bundle size also appears to decrease.

Resonance Raman spectra taken from the side of this array (Figure 4-2a) indicate a shift toward larger SWNTs near the root. However, due to the reasons mentioned above, it is difficult to obtain accurate and quantitative information of the diameter distribution in a SWNT sample.

4.2.2 Decomposed UV-vis-NIR optical absorption

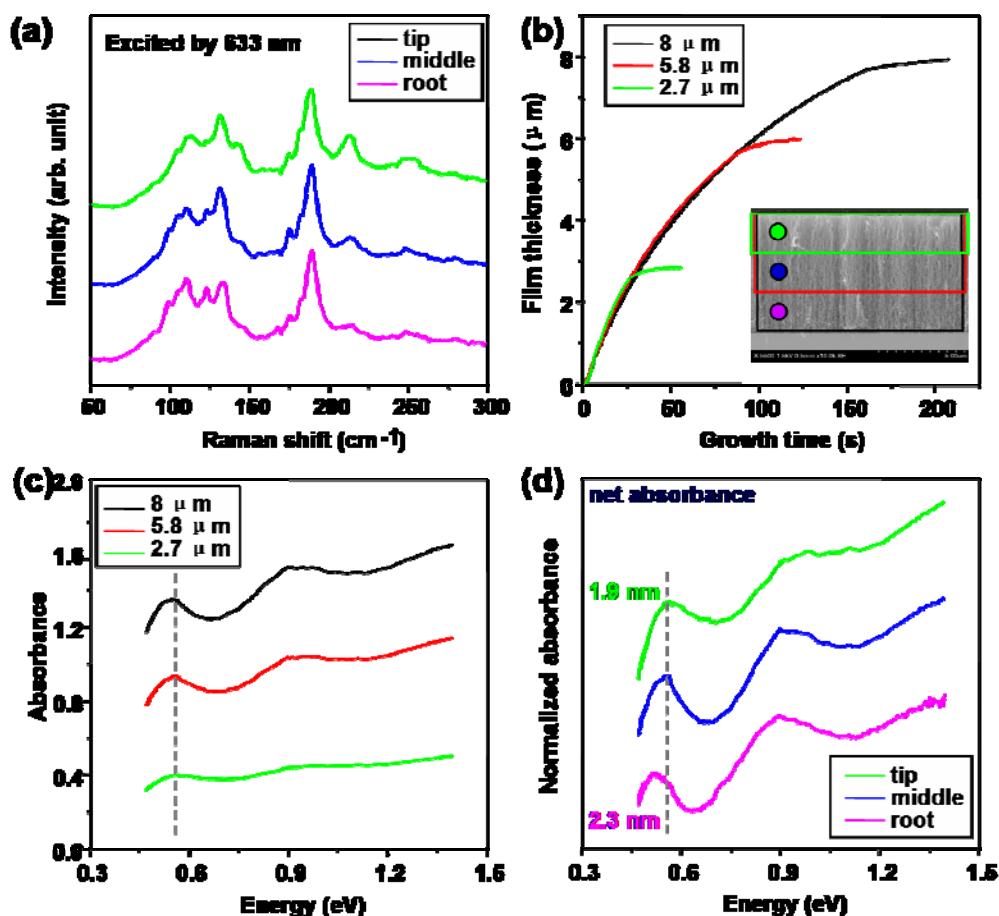


Figure 4-2. (a) Raman spectra scanned from the cross-section of a typical aligned SWNT array taken by 633 nm laser with a top-notch filter, showing that the diameter of SWNTs at root seems to be larger than the ones at the tip; (b) the growth curves of three samples grown at strictly same condition but for different CVD time, with the inset showing the morphology of SWNTs corresponding to these three samples; (c) optical absorption spectra of the these three samples; (d) net/absolute absorption spectra of the different parts of one SWNT array (obtained by subtracting the data in (c)), showing the quantitative diameter change during one CVD.

For a more quantitative characterization, I synthesized three VA-SWNT arrays under strictly identical conditions, changing only the CVD time. As shown by the growth curves in Figure 4-2b, these three arrays exhibit almost exactly the same growth behavior, having nearly identical growth rates and catalyst deactivation times, but were allowed to grow to different heights. Therefore, one can expect all three VA-SWNT arrays to have very similar

properties and morphologies. Absorption spectra corresponding to each of these arrays are shown in Figure 4-2c, in which little difference is seen in the E_{11} and E_{22} peak positions. Assuming the only difference in these SWNT arrays is their height, then the 6 μm array (red box in Figure 4-2b) is essentially two 3 μm arrays (green box in Figure 4-2b) stacked on top of each other. Hence, subtracting the spectrum of the 3 μm array from the spectrum of the 6 μm array is considered to yield the absorption contribution of the bottom half of the 6 μm array, which should closely resemble that of the 3 μm array. Decomposing the spectra in this fashion results in the spectra shown in Figure 4-2d, where the spectrum labeled “top” is simply the spectrum from the 3 μm array, the “middle” spectrum is the spectrum of the 6 μm array minus the spectrum of the 3 μm array, and likewise the “root” spectrum is the difference between the spectra of the 8 μm and 6 μm arrays. The peak positions in Figure 4-2d are clearly different, indicating that the morphology is *not* uniform, and that the SWNTs at the root of the array (synthesized later) have larger diameters than those at the top (synthesized earlier). The diameter increase was approximately 20% in this case.

In the following, I discuss the mechanism of this diameter change during CVD. One possible reason for this change is that the smaller catalyst particles (yielding smaller diameter SWNTs) may have shorter catalytic lifetime than larger ones, therefore exist only at the beginning of the CVD process, and in the later stage they may have been detached at their roots from the substrate, moving up in still-growing array. The average diameter in the array therefore increases accordingly. However, this process should induce significant internal stress in the array, which could result in halting the growth of the array. Another, more probable explanation is that some catalyst aggregation and/or ripening could be occurring at the growth temperature, causing the diameters of all the SWNTs to increase. Since not every catalyst particle is able to produce a SWNT an abundance of metal should be present at the substrate surface. This trend is exaggerated in taller arrays. Through HR-TEM observation of

a 200 μm thick VA-SWNT array, I found that the top of the array contains SWNTs with diameter ranging 1-3 nm, typical for ACCVD. The root part, on the other hand, was found to contain SWNTs with diameters as large as 5 nm. Images of catalyst nanoparticles at the root of the array (still attached to some of the SWNTs) were also considerably larger than the typical^[27] size of 2 nm. Since catalyst particles this large are not produced by the standard catalyst preparation process, this strongly indicates metal aggregation and/or ripening of the catalyst nanoparticles. With these vertically aligned SWNT samples, this change can be clearly and quantitatively demonstrated. The most obvious way to minimize catalyst diffusion/ripening, thus inhibit the diameter change in an array, is to use lower growth temperatures, shorter growth time, and, most effectively, higher Mo concentration to suppress the diffusion of Co atoms. Preliminary results show better uniformity can be achieved by this approach, but this investigation is still ongoing. Quantifying the diameter change along an array is helpful to understand results of other characterizations, which is to be presented in the next section.

4.3 Diameter tailoring

4.3.1 Effect of CVD parameters

Figure 4-3 presents resonance Raman and optical absorption spectra of samples grown at various CVD temperatures and pressures using our standard catalyst recipe. Although a clear difference is seen in the RBM region of the Raman spectra (Figure 4-3a), indicating an increase in small-diameter SWNTs at reduced temperature and increased pressure, the position of the E_{11} and E_{22} peaks in the optical absorption spectra (Figure 4-3b), remain unchanged. This indicates that although more small-diameter SWNTs may have been synthesized at these conditions, the percentage of these SWNTs in the entire sample is still

small. A significant difference in the overall diameter distribution should be obvious in the absorption spectra.

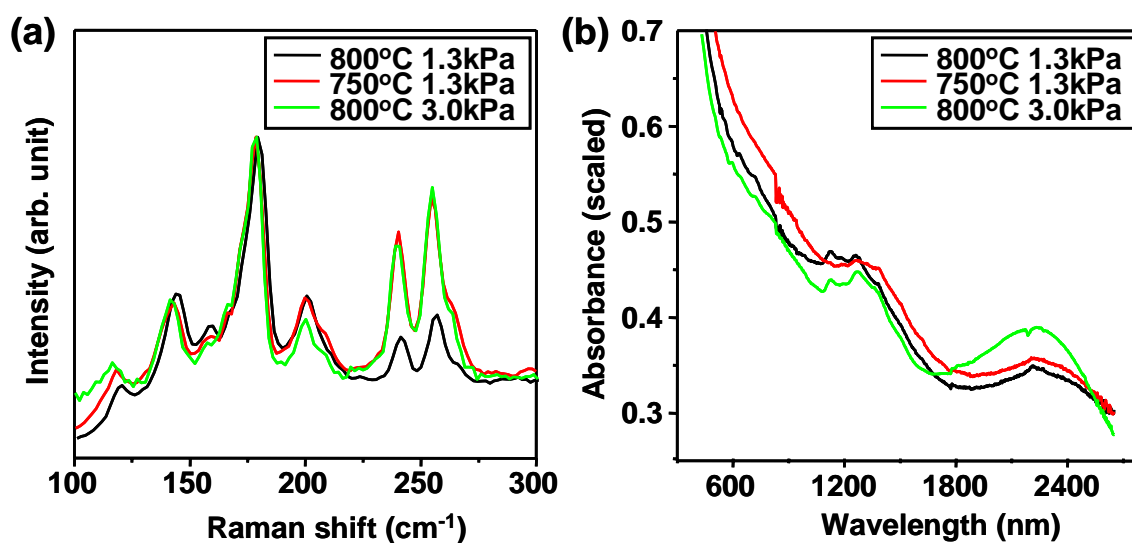


Figure 4-3. (a) Raman and (b) UV-vis-NIR optical absorption spectra of aligned SWNTs grown at different temperature and pressure, showing clearly different Raman RBM peak intensity but similar absorption peaks position.

4.3.2 Effect of catalyst recipe

It has been well recognized that the diameter of a SWNT is strongly dependent on the size of the catalyst nanoparticle from which it grows.^[126] Therefore, controlling the catalyst size is the most straightforward approach to tailor the SWNT diameter. This can be achieved by adjusting both the catalyst preparation and the supporting substrate. One difference in the growth of SWNTs on a flat substrate compared to the use of other catalyst supporting materials, such as zeolites, is that the latter uses the substrate to restrict the size of the catalyst particle. On a flat substrate, however, the nanoparticles can more easily migrate and aggregate at high temperature during CVD. The introduction of a secondary supporting species, such as molybdenum^[27] or alumina^[30], has been often employed and deposited on the

surface of substrates as intermediating layers to suppress migration of the metal catalyst nanoparticles.

4.3.2.1 UV-vis-NIR optical absorption

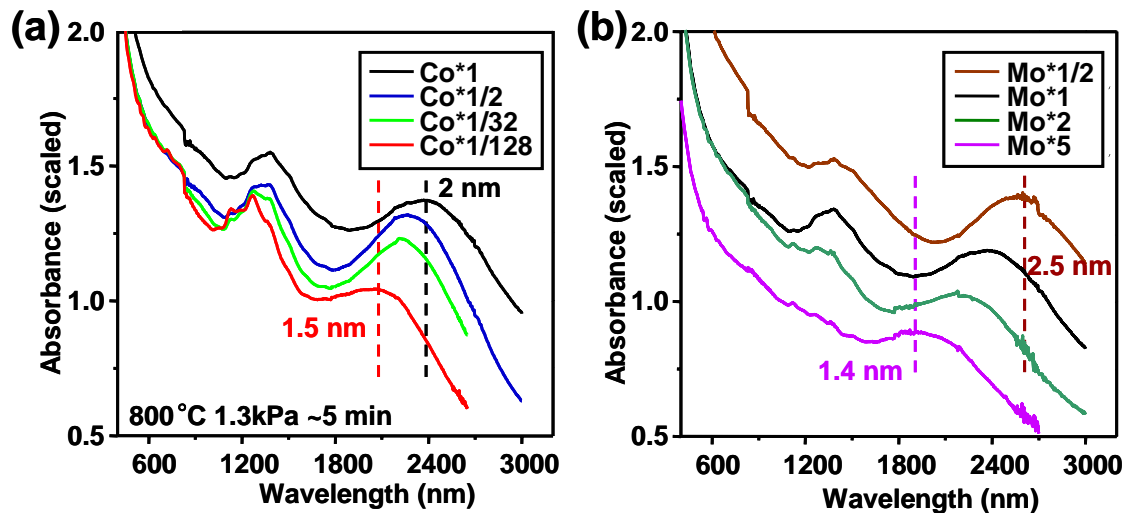


Figure 4-4. (a) UV-vis-NIR optical absorption spectra of aligned SWNTs grown from different catalyst recipe. The concentration of the catalyst solution is normalized by a standard value of 0.01% for both cobalt acetate and molybdenum acetate.

Since Co is the catalytically active species in ACCVD, changing the amount of Co is the most straightforward way to modify the final catalyst size. As shown in Figure 4-4a, reducing the absolute amount of Co from our standard recipe resulted in a blueshift of the E_{11} peak in the absorption spectrum, indicating a smaller average SWNT diameter. Although the absorption spectrum might not reflect the real distribution, the change in the average diameter is obvious. As can be seen in Figure 4-4a, the average diameter was reduced from 2.0 to 1.5 nm, but this relatively small change required a decrease in the amount of Co to 1/128. Figure 4-4b shows the optical absorption spectra of VA-SWNTs grown from different Mo concentration, showing that the diameter of the SWNTs is much more sensitive to the amount of Mo. The average diameter changed over a wider range, from 2.5 to 1.4 nm, by changing

the amount of Mo by a factor of ten. This agrees well with the hypothesis that Mo forms an oxide that strongly interacts with Co, reducing its mobility at high temperatures^[27].

4.3.2.2 Raman spectroscopy

Figure 4-5 shows the result of Raman scattering measurement, showing agreement with this conclusion. Two significant differences can be observed in the Raman scattering spectra of the samples from the reduced-Co recipe. First, in the RBM range, peaks at higher frequency were enhanced in the sample grown using the least amount of Co, which indicates the increased population of small-diameter SWNTs. Second, an emergence of more intense Breit-Wigner-Fano (BWF) features in the G-band region with reduced Co amount, indicating the increased population of small-diameter metallic SWNTs. Similar results have been obtained for the increased-Mo case.

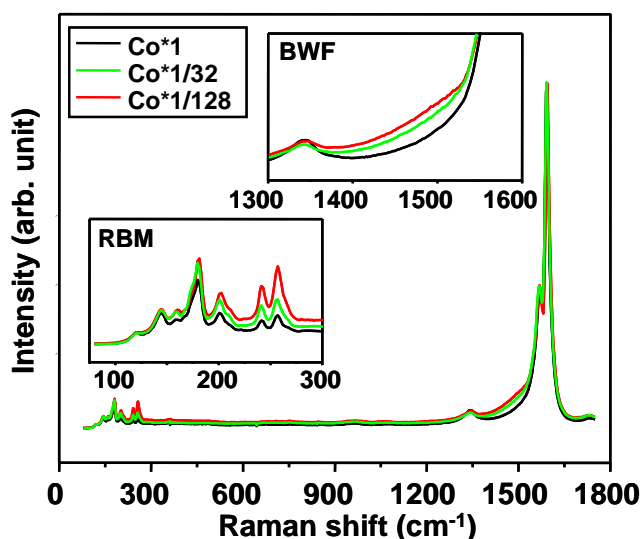


Figure 4-5. Raman spectra of vertically aligned SWNTs obtained from ACCVD with reduced Co amount on the quartz substrate, showing consistent results with the optical absorption data on the existence of smaller diameter SWNTs.

4.3.2.3 TEM and histogram

Figure 4-6 shows two typical high-resolution TEM (HR-TEM) images of (a) a standard SWNT array, and (b) a small-diameter array (1/128 Co). It is clear that the SWNTs in Figure 4-6b have smaller diameters than those in Figure 4-6a. Diameters of more than 150 SWNTs measured from the HR-TEM measurement are plotted in Figure 4-6c. This shows that the average diameter for this sample (b) is around 1.2 nm, which is slightly smaller than the average value determined from optical absorption (1.4 nm).

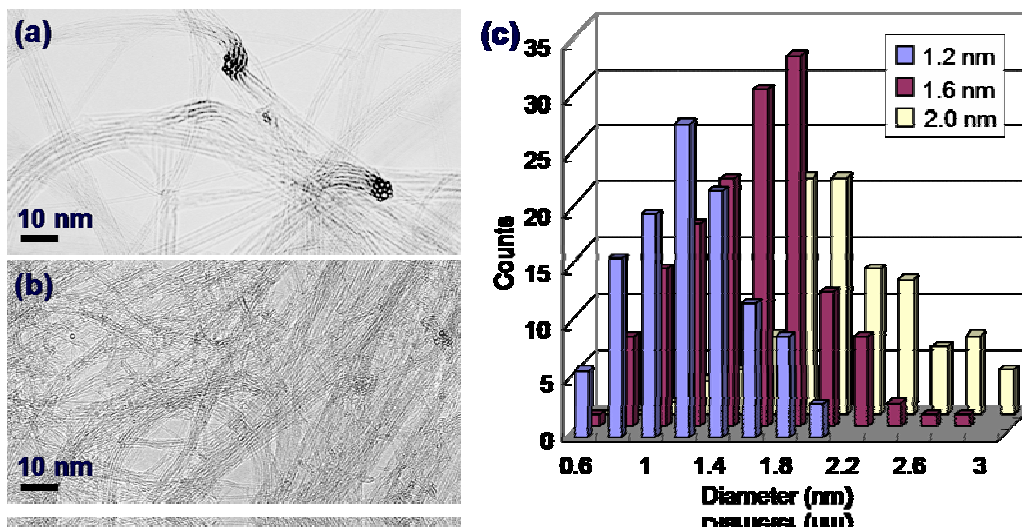


Figure 4-6. Typical (a) TEM images and (b) diameter histogram of normal (~2 nm) and small-diameter (~1.6, 1.2 nm) vertically aligned SWNTs.

The observation shown in Figure 4-2 helps to understand the data presented for Figure 4-6. The difference between diameter estimates based on optical absorption and HR-TEM measurements is likely because the former averages the entire array, whereas the latter is only representative of a local region that is not necessarily representative of the entire array. Nevertheless, the results shown in Figure 4-6 indicate that it is possible to synthesize VA-SWNTs with diameters as small as 1.2 nm. Perhaps with better control over the catalyst preparation and CVD process, this small diameter can be maintained. Since large-diameter SWNTs are typically more defective, and less rigid than small-diameter SWNTs, the

diameter increase may also explain the morphology evolution at the cross-section of the array. The SWNTs with smaller diameters form well-aligned bundles near the top, but as the diameter increases the SWNTs become kinked and poorly aligned, when the CVD is continued to the end of the growth process. Also, so-called G-to-D ratio in Raman spectra has been observed to decrease toward the bottom of the array.

4.4 Summary

To summarize, I present a comprehensive study on the diameter control of our vertically aligned SWNT arrays grown from Co/Mo bimetallic catalyst. Optical absorption shows that the average diameter can be tailored over a wide range by changing the catalyst recipe. The tendency agrees well with both Raman scattering spectra and, more importantly, the result obtained from HR-TEM observation. I also showed that the diameter of the SWNTs tends to increase during synthesis. Quantitatively, a difference of 20% was found in this study. This non-uniformity gives insight into how to accurately characterize the diameter distribution and quality of such vertically aligned SWNTs. I speculate that the diameter increase could be a universal phenomenon in SWNT catalytically synthesized on flat substrates, but comparison with other methods is necessary to support this hypothesis.

Chapter 5 High-precision patterned growth

In the liquid-based dip-coating, hydrophilicity of Si/SiO₂ substrate is found to be critical for the successful deposition of catalyst and hence SWNT growth. When the surface is functionalized by self-assembly monolayer (SAM) and becomes hydrophobic, no catalyst remains and no SWNT grows. This concept can be utilized to localize the growth of SWNTs at designed regions where SAM were selectively removed. Patterned high-quality as-grown SWNTs with different morphologies can be obtained by this facile, scalable and accurate method.

5.1 Background and motivation

The excellent properties of carbon nanotubes (CNTs), particularly chirality-dependent electrical conductivity of single-walled carbon nanotubes (SWNTs), make them one of the most attractive building blocks for the next generation nano-devices.^[100] Localizing the growth of CNTs, therefore, has attracted much attention, since it is a critical step for the fabrication of on-substrate devices.^[38, 127-131] The conventional way is to pattern catalyst by sputtering or evaporation of metal through a physical mask or a pre-exposed photoresist layer.^[38, 41] This conventional MEMS technique is, although effective, normally complicated and expensive. Another classic concept to control the CNT location was demonstrated in ferrocene-based floating chemical vapor deposition (CVD) using the growth selectivity between SiO₂ and Si (or metal).^[128, 129] However, floating CVD was not very successful in yielding SWNTs on substrate. More importantly, all these previous techniques normally contain multi-step treatments. High resolution, low cost, easy fabrication and large throughput can never be achieved at the same time. A method with great potential to achieve

these is the liquid-based dip-coating, which possesses great advantages in cost and scalability to prepare dense nano-particles on a substrate.^[23, 26] The dip-coating method, combined with alcohol catalytic CVD (ACCVD), has been successful in synthesizing high-quality random and aligned SWNTs. However, the deposition mechanism of the dip-coating is so far not well understood and no compatible strategy has been found to localize the growth in this process.

In this chapter, I firstly show that the conventional concept of using SiO₂ patterned Si substrates to selectively grow 3D carbon nanotube structures can also be applied to a dip-coating method. High-quality vertically aligned single-walled carbon nanotube (SWNT) patterns can be easily obtained by this protocol. Apart from the sintering of catalyst into Si at high temperature, the difference in surface wettability between Si and SiO₂ also plays an important role in this selective growth, which leads me to a novel method of patterning the growth on chemically modified surfaces. By forming hydrophilic/hydrophobic patterns on a silicon substrate by self-assembled monolayer^[132] (SAM) surface functionalization, catalyst is deposited and thus SWNTs grow only in the regions where surface is highly hydrophilic. The all-liquid-based procedure allows one to bypass conventional complicated fabrications and yield controlled patterns consisting of high-quality as-grown SWNTs.

5.2 SWNT growth on Si/SiO₂ patterns

The conventional concept of using the different growth behavior of CNTs on Si and SiO₂ to form CNT pattern was only successful in producing multi-walled CNTs in the ferrocene-based process. Here I borrow this concept and show that similar growth selectivity can also be obtained when dip-coating is used for catalyst preparation. SWNTs grow only in SiO₂ regions of a Si and SiO₂ patterned substrate.

SWNT arrays were grown on SiO₂ patterned Si substrates using ethanol as a carbon source and Co as the catalyst.^[16, 23] A 50 nm thick SiO₂ layer was patterned on a Si wafer using standard UV lithography combined with HF etching. The catalyst was loaded onto the substrate by the previously reported dip-coating process.^[26, 75] Only cobalt acetate was used here as the catalyst precursor. We recently found vertically aligned SWNT arrays can still be obtained when Mo is absent, as long as the parameters are well optimized. ACCVD was performed at 700-800 °C with an ethanol flow of 450 sccm at a pressure of 1.3 kPa. The as-grown SWNTs were characterized using scanning electron microscopy (SEM, accelerated at 1 kV) and Raman spectroscopy (excitation laser wavelength 488 nm). Catalyst morphologies on the substrate surface were imaged by atomic force microscopy (AFM).

Figure 5-1a shows typical top-view SEM images of an electrode-shaped SWNT pattern. It is clear that SWNTs grow only in regions where an oxide layer is present. No growth was observed in areas where the oxide layer had been etched by HF. The SWNT structures can form lines, hexagons (Figure 5-1c) or other shapes depending on the pre-designed pattern. The resolution of this method is limited by the ability of obtaining oxide area on a Si wafer. In this experiment, a linewidth of several micrometers was achieved using UV lithography. If other higher resolution techniques (e.g. electron-beam lithography, scanning probe oxidation) were used, finer SWNT structures may be obtained. The convenience in this approach is that the region where SWNTs grow can be well controlled by pre-fabrication; dip-coating was performed on the entire substrate and no further processing (e.g., lift-off) was needed.

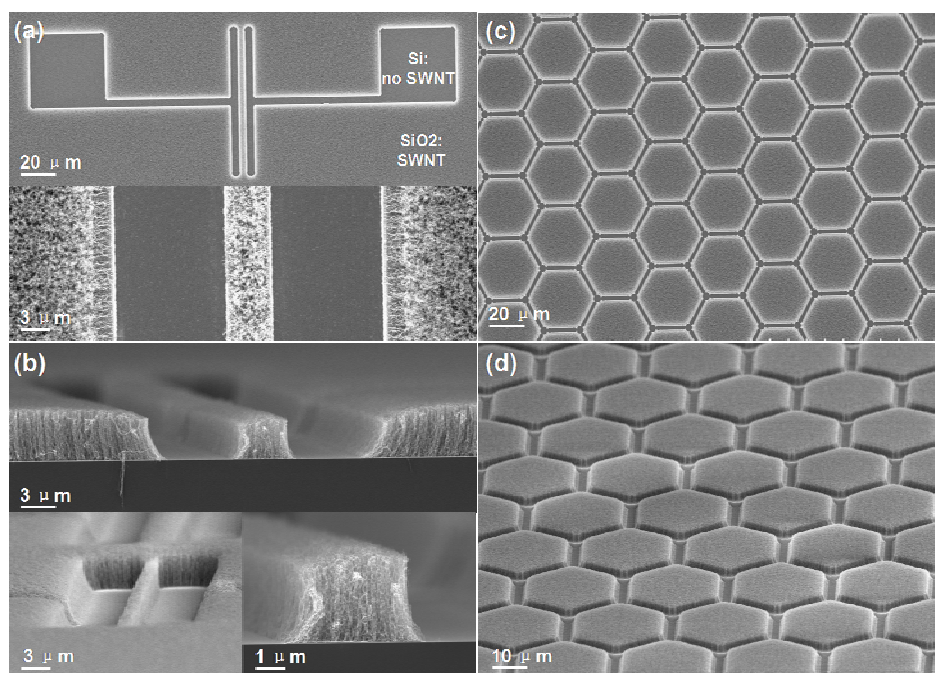


Figure 5-1. (a) Top and (b) side view SEM images of an electrode-shaped pattern, where SWNTs only grow in the SiO₂ regions. (c) Top and (d) side view images of hexagon-shaped patterns. The growth behavior of SWNTs at the edges is slightly different from in the center of a vertically aligned forest.

The cross-sectional view of a pattern (Figure 5-1b) confirmed the alignment of the obtained SWNTs. However, SWNTs can also grow into random networks if the catalyst density is significantly decreased. Both edges of a line pattern always exhibit transition regions, where the SWNTs are not perfectly perpendicular to the substrate. Apart from these few micrometers, the alignment is essentially the same as in vertically aligned SWNT arrays. The formation of such transition regions is very likely due to the different wetting behavior of liquid at the edge (more discussion on this edge effect later). Further study is needed to understand and control this phenomenon.

Raman spectroscopy is a powerful tool to evaluate the existence and quality of SWNTs. Typical Raman spectra are presented in Figure 5-2. For a patterned SWNT stripe with the spacing of larger than 10 micrometers, it is easy to focus the laser in the SWNT and non-SWNT areas, as shown in the inset optical microscope images. In the SiO₂ region, where

SWNTs are expected to grow, strong and clear peaks are observed around 1592 cm^{-1} (G-band) and in the range from 100 to 300 cm^{-1} (radial breathing mode, RBM). A clear split of the G-band and the strong intensity of RBM peaks confirm the existence of SWNTs. A weak D-band at 1344 cm^{-1} indicates that the SWNTs are well crystallized. In contrast, neither G-band nor RBM peaks were detected in the Si regions. This indicates there are almost no SWNTs grown on Si, which is consistent with SEM observations. A sharp peak at 520 nm , attributed to bulk silicon, is observed in both Si and SiO_2 regions. It is also worth noting that, due to the strong resonance effect, Raman spectroscopy, particularly RBM peaks, only shows information from a limited number of SWNTs in the entire array. Further characterization by transmission electron microscopy (TEM) revealed only SWNTs. The diameter range is from $1\text{-}3.5\text{ nm}$, with a mean value slightly larger than 2 nm . When Co/Mo bimetal catalyst was used, however, the average diameter can be reduced.^[75, 94, 133]

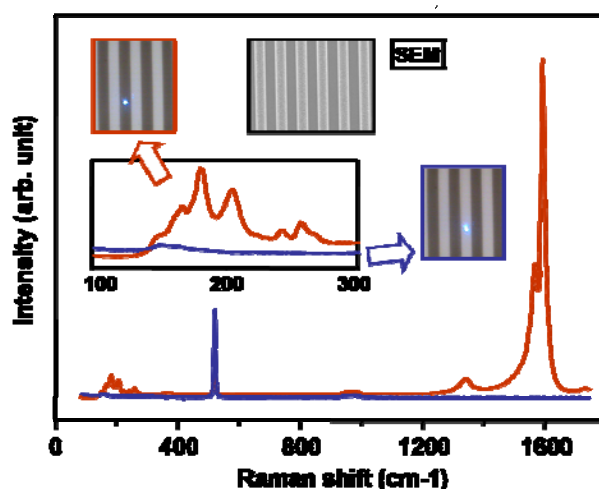


Figure 5-2. Raman spectra from Si (blue) and SiO_2 (red) regions, showing that high-quality SWNTs are obtained on SiO_2 but almost no SWNTs grow on Si. The inset shows optical microscope and SEM images of linear SWNT patterns.

The growth selectivity of CNTs on Si and SiO_2 was believed to be due to the higher reactivity of metal with Si at high temperature. The sintering of Fe into a Si substrate at 800°C has also been directly observed by TEM.^[111] I believe such catalyst sintering will also

happen in our process if the catalyst were uniformly deposited on both Si and SiO₂ surfaces. However, since dip-coating is a wet process, the difference in surface potential (i.e., wettability) may also play a critical role. SiO₂ is very hydrophilic, having a water contact angle of nearly 0°. Si, on the other hand, is relatively hydrophobic, with a water contact angle of approximately 90°. This may also introduce some difference even in the dip-coating stage, meaning that catalyst may be selectively deposited on the oxide layer from the very beginning.

The difference in catalyst deposition is first evidenced by the temperature dependence of the selectivity between Si and SiO₂. Some reports have claimed that at lower temperature (e.g., 700°C), CNTs can also nucleate on a Si surface.^[129, 134] This is because the diffusion of metal into Si is considerably slowed. However, in our process no SWNTs were obtained at 700 or 750°C, which indicates that the reaction between metal and substrate may not be the dominant issue here.

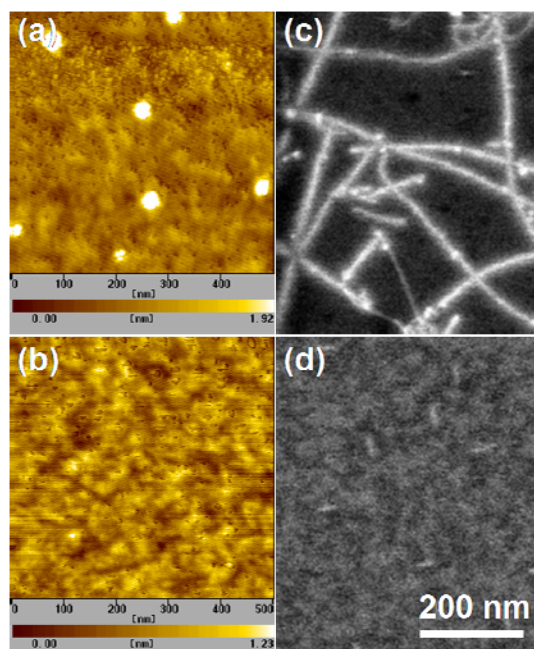


Figure 5-3. AFM images of (a) SiO₂ and (b) Si surface prior to CVD synthesis of SWNTs; SEM images of (c) SiO₂ and (d) Si surfaces after CVD. Catalyst deposition and SWNT growth occur on SiO₂ but growth on Si is considerably suppressed.

Direct evidence was obtained by AFM imaging of the surface of Si and SiO₂ after catalyst preparation. Figure 5-3 shows the surface morphologies before and after CVD. In this case the catalyst density is low so that each particle can be clearly resolved. Interestingly, after calcination at 400°C, particles with diameter around 2 nm were already formed on the SiO₂ surface. On the Si surface, however, no apparent particles were observed. This confirms that clear differences exist even before reduction of catalyst at high temperature. Since oxide is not expected to react with the Si wafer, especially at only 400 °C, the difference should result directly from dip-coating. SEM images of the surface after CVD are consistent with AFM observations; the density of SWNTs grown after CVD is similar to that of the particles formed after calcination. No SWNTs were observed on Si.

The surface-wettability induced selective deposition of catalyst is also supported by the edge shape seen in Figure 3-1b. If there were no difference in wetting and drying of the catalyst solution between Si and SiO₂ catalyst particles would be expected to form uniformly on the entire surface, including the Si-SiO₂ boundary. In this case, the vertical alignment of the SWNT forest grown on a SiO₂ pattern should be perfect, i.e., no edge effect should be observed.

Finally, I propose some other strategies to tailor the surface wettability of SiO₂ to confirm its intrinsic effect on catalyst deposition by dip-coating. One effective approach to change SiO₂ from hydrophilic to hydrophobic is chemically modulating the termination group using a self-assembled monolayer (SAM). One advantage generated from this one-molecule-thick (~2 nm) covering is that the topography effect (which may affect the dip-coating when SiO₂ is 50 nm higher than Si) is reduced to a minimum. Thus, if similar selective deposition of catalyst happens in such a system, the wettability difference between Si and SiO₂ must play an important role. I found on SAM-functionalized surfaces, where the water contact angle is around 90°, the amount of SWNTs grown is considerably reduced. No

growth occurs when the substrate is fully covered by SAM, even if the substrate is entirely SiO_2 , thus changing only the surface wettability can also localize the SWNT growth to hydrophilic areas. Detailed experiments and discussion related to this topic will be shown from the next section.^[135] Patterned growth of SWNTs on SiO_2 will be important for the realization of nanotube-based applications, such as field-effect transistors, where an oxide layer is needed as a back gate.

I have shown that the classic concept of using SiO_2 patterned Si substrates to selectively grow 3D carbon nanotube structures can also be applied to a dip-coating method, and high-quality vertically aligned single walled carbon nanotube (SWNT) patterns were obtained easily by this approach. The reason for the different SWNT growth behavior on Si and SiO_2 not only lies in the lower stability of catalyst on Si at high temperature, but also in the different wetting behavior during the dip-coating stage. This leads me to a novel method of patterning the growth on surface modified substrates. This study broadens our understanding of liquid based dip-coating and provides one an alternative approach to fabricating 3D structures consisting of high-quality SWNTs.

5.3 Effect of surface wettability

Catalyst for the growth of SWNTs was prepared by a dip-coating process similar to previous section. Briefly, Si/ SiO_2 substrate (Si with 50 nm oxide layer in this case) was dipped into an ethanol solution containing catalyst precursor (0.01% wt. of Co acetate), soaked for 3-10 mins and then pulled up at a certain speed (6 cm/min maintained by a motor). The substrate is then calcinated in air at 400°C for 5 min. In order to study the intrinsic effect of surface wettability on the catalyst dip-coating, I modulated the surface from hydrophilic into hydrophobic by forming a SAM. The Si/ SiO_2 substrate was first cleaned by SC1 solution

at 75°C for 5 min, rinsed with DI water, and dried before it was dipped into a solution of toluene with 65 ppm octadecyltrichlorosilane (OTS) for 15 min. CVD growth of SWNTs was carried out in a quartz tube at 800°C using 1.4 kPa of ethanol as a carbon source. The as-grown sample was characterized by Raman spectroscopy (excited by 488 nm laser) and scanning electron microscopy (accelerated at 1 kV).

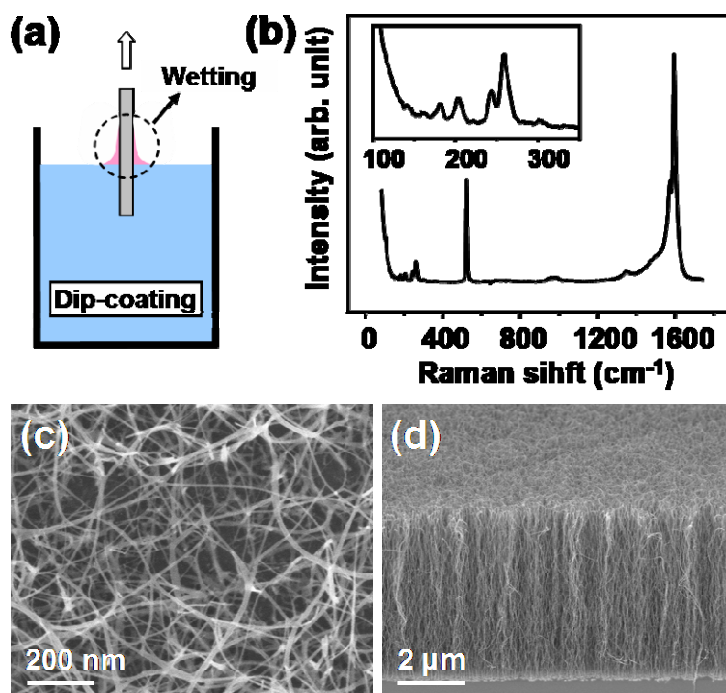


Figure 5-4. (a) Schematic of dip-coating process in case of a hydrophilic substrate with a meniscus formed; (b) Raman spectrum and SEM image taken from the top of typically grown random SWNTs on Si/SiO₂ surface; (d) cross-sectional view of a vertically aligned array grown from a similar method.

Figure 5-4a is a schematic of the dip-coating process. With a hydrophilic surface, a meniscus (indicated in red) is formed with a contact line typically located at 2-3 mm above the ethanol pool free surface. Before pulling up the substrate, the substrate is kept in the solution for 3-5 mins, thus the system is expected to be at equilibrium. Therefore, the catalyst deposition condition is expected to be determined by the wettability of the substrate. The initial equilibrium has been confirmed by preparing three substrates with different soaking time in ethanol (1 min, 3 min and 10 min). After CVD, no noticeable differences in SWNT

yield or quality were found among these three samples. This means that the effect of residence time on the catalyst formation during a dip-coating is negligible. Typical Raman spectrum of the grown sample presented in Figure 5-4b shows that the quality of SWNTs obtained from this method is high. The D-band intensity is small and clear RBM (radial breathing mode) peaks can be observed. The SWNTs can also grow into different shapes, e.g. random network in Figure 5-4c or vertically aligned array in Figure 5-4d, depending on the efficiency of the catalyst.

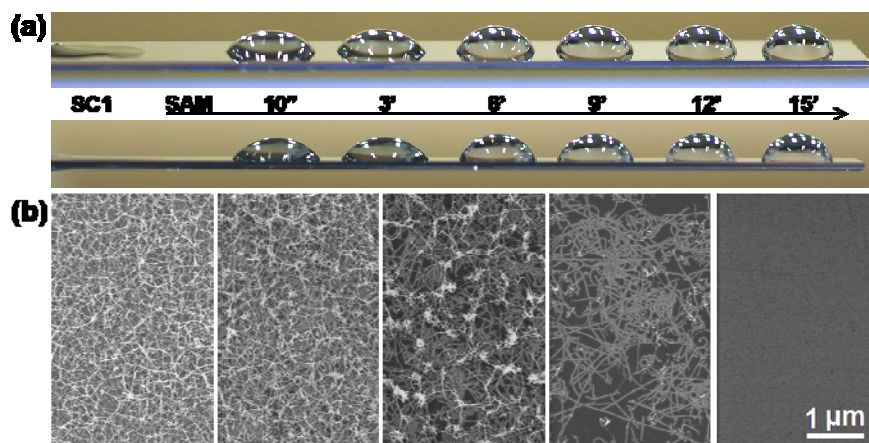


Figure 5-5. (a) Various contact angles of water droplets on Si/SiO₂ surface functionalized by OTS monolayer with different reaction time and therefore different SAM converge; (b) SEM images of SWNTs grown on substrate shown in (a) after catalyst dip-coating.

It is now interesting to check the effect of the substrate surface wettability on the formation of catalyst and consequently on the growth of SWNTs. Among the different methods to modulate the surface potential, forming SAM is a simple and nondestructive one.^[136] In addition, the theoretically perfect flatness of an SAM makes the topography-induced effect negligible. Figure 5-5a shows the profiles and contact angles of purified water droplet on the surface of Si/SiO₂ after reaction in OTS/toluene solution for different time durations. It is clear when the coverage of OTS increases, the originally very hydrophilic silicon surface (with almost 0° water contact angle) becomes more hydrophobic. After catalyst dip-coating

and SWNT growth on this substrate with gradually changed OTS coverage, the SEM images in Figure 5-5b taken at different positions clearly show that the density of SWNTs decrease from left to right. This indicates that the amount of catalyst deposited on the surface decreases when substrate becomes hydrophobic. Finally, no SWNTs were found on the substrate with 15 min SAM formation. Raman spectra taken at corresponding positions, shown in Figure 5-6, agree well with the SEM images. The G-band and RBM peaks gradually diminish in intensity and finally disappears.

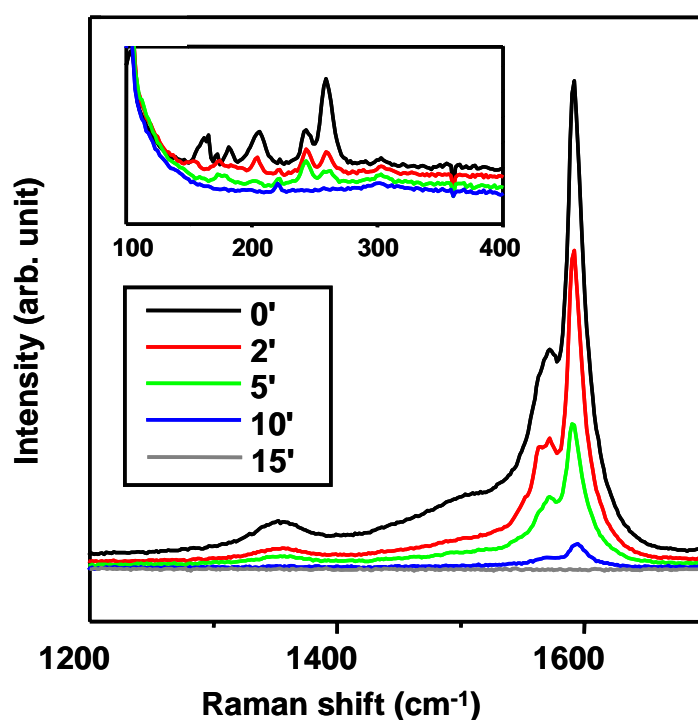


Figure 5-6 Raman spectra taken from SWNTs grown on substrate regions with different extent of OTS coverage. Decreasing intensity suggests that as the OTS coverage increases and the surface becomes more hydrophobic, fewer and fewer SWNTs are formed on the substrate.

In order to understand the mechanism how surface wettability changes the effect of dip-coating, I characterized the SAM covered surface by AFM. Clearly shown in Figure 5-7, the SAM growth follows a so-called “island” growth model. The SWNT yield is mainly determined by the area that is still not covered of the SAM, i.e. the area where catalyst deposited. A schematic of this process is shown in Figure 5-7d.

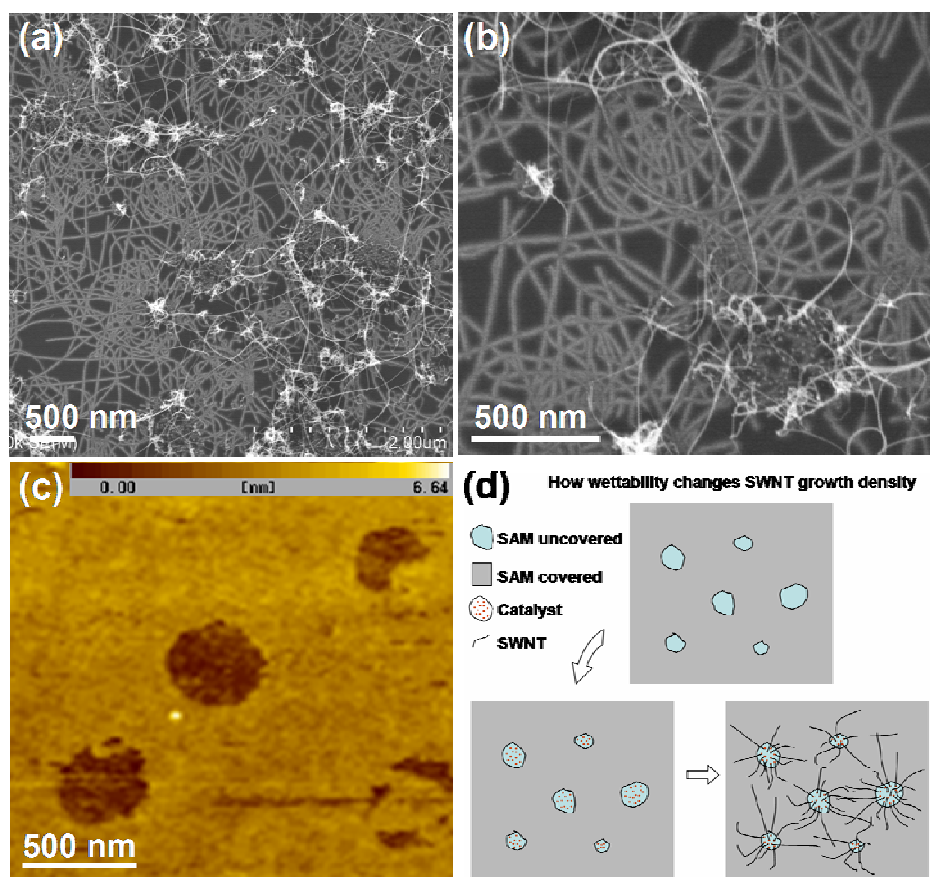


Figure 5-7. (a)(b) SEM images of SWNTs grown on a substrate where SAM is not fully covered (corresponding to the third stage in Figure 1b); (c) a typical AFM image of the partially-SAM-covered surface, indicating SAM formation follows so called “island” mechanism;^[136] (d) A schematic showing how surface wettability, i.e., SAM coverage, changes the density of SWNTs grown.

5.3 SWNT pattern obtained from UV lithography

The beauty of SAM lies in not only the easy fabrication and drastic change of surface energy (by only one layer of molecules), but also the reversibility of the SAM process. For example, deep UV (here 254 nm) was found able to remove the SAM effectively.^[136] The exposed surface can retrieve its hydrophilicity (water contact angle back to almost 0°) and SWNTs can grow on it again efficiently. Therefore, together with a masking technique, silicon surface with hydrophilic/hydrophobic patterns can be easily obtained. A schematic

showing the fabrication process is presented in Figure 5-8a. In our experiment, I used a line shape photomask for the UV exposure, and the obtained patterns after dip-coating and SWNT growth are shown in Figure 5-8b. Clearly at the regions that were exposed to UV radiation after SAM formation, dense SWNTs were obtained. On the other hand, in the masked areas, no catalyst was deposited since the surface hydrophobicity was maintained. Finally, the growth of SWNTs was successfully localized. Compared with the post-pattern techniques,^[137-139] which normally introduce some irreversible destruction and contamination (e.g. pre-dispersion with surfactant) to the SWNTs, these high purity and quality as-grown SWNTs can be expected to give better performances in device applications.

Apparently, this is a versatile strategy of catalyst patterning that can be applied to growth of SWNT with various morphologies. In Figure 5-8b, both random network and vertically aligned array of SWNTs were obtained (depending on the density of Co particles formed). It is also reasonable to believe that patterned catalyst prepared with this method is also suitable to yield horizontally aligned SWNTs, which may be more interesting for device applications. Fabrications of SWNTs with various other shapes and morphologies are ongoing.

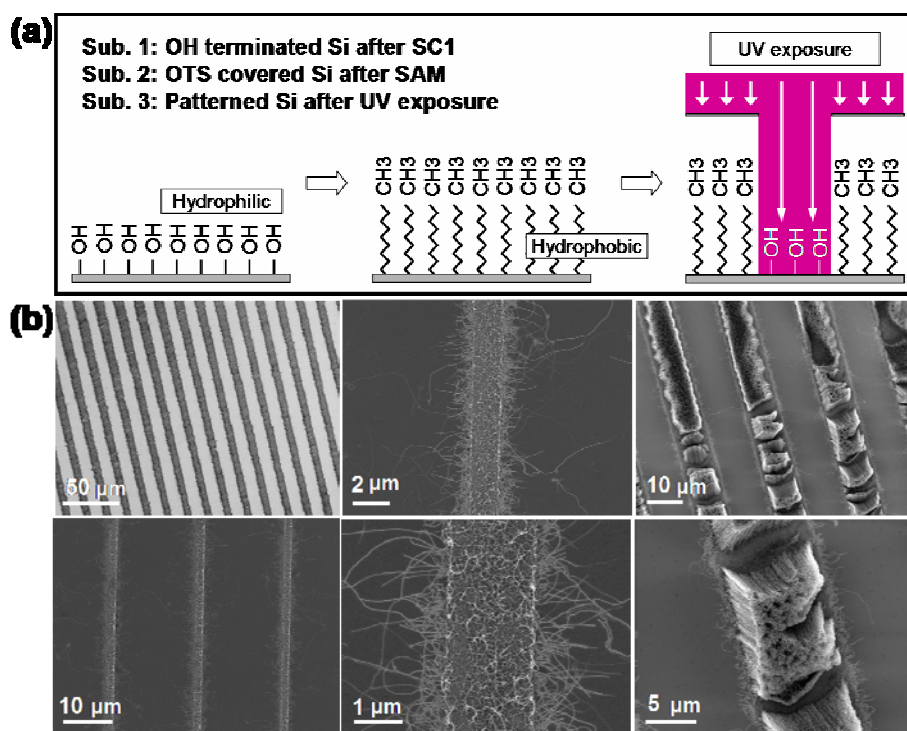


Figure 5-8. (a) Schematics describing the fabrication procedure of hydrophilic/hydrophobic patterns using a selective removal of OTS SAM by UV exposure; (b) SEM images of random and vertically aligned SWNT line-shape patterns.

This technique is probably the most fabrication-friendly method so far to directly grow SWNT patterns. It is more scalable compared with selective sputtering or evaporation methods. It is also worth emphasizing its potential in realizing patterns with high spatial resolution. Since only one step UV exposure is involved here, the accuracy of catalyst selective deposition can be controlled more easily than other multi-step MEMS-fabrication techniques.

5.4 SWNT patterns obtained from e-beam lithography

The OTS SAM can also be damaged by electron beam irradiation or direct scanning probe lithography.^[140] By dip-coating after selective removal of SAM by electron beam, the resolution of existing dry patterning techniques can be surpassed. Preliminary results show that when an electron beam with diameter of several nanometers is used for etching the SAM,

catalyst-coating and SWNT growth can be easily confined to a linear region with a width of 50 nm. Theoretically, OTS may be manipulated at the several-molecule width level, as demonstrated in Figure 5-9a. Using monolayer molecules as a resist also minimizes the amount of scattered electrons that sometimes broaden the exposed area. The ultimate resolution of one line scan may be as low as 10 nm.

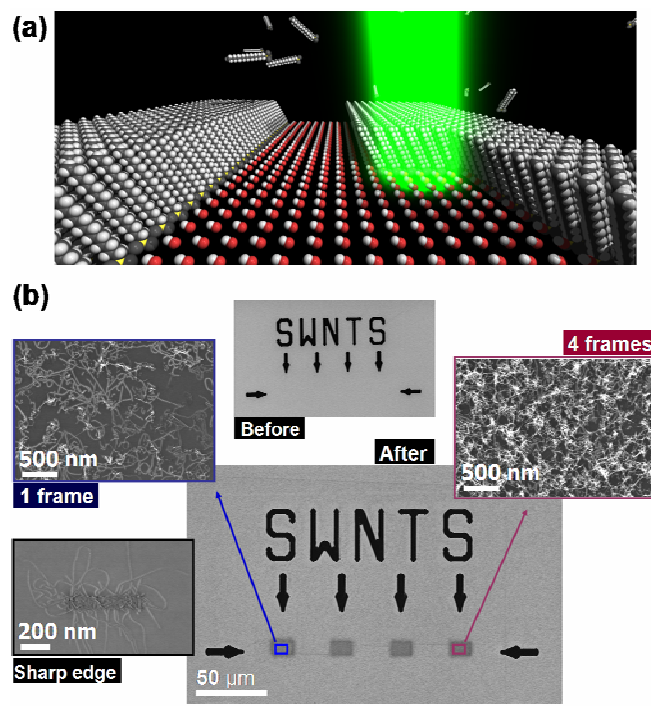


Figure 5-9. (a) Schematics describing the process of removing OTS by nanometer-size electron beam; (b) SEM images of SWNTs grown in the regions where OTS were selectively removed, suggesting the location and density of SWNTs can be controlled.

Another advantage of using the monolayer is that a small dose of electrons is sufficient to tailor the surface condition. This makes exposure using the beam of a commercial SEM is possible. Figure 5-9b shows one example of defining the growth area of SWNTs using a SEM. Arrow-shaped Si/SiO₂ patterns were first fabricated on the substrate to indicate the area where we want the SWNTs to grow. In those four gray boxes, the SAM was removed to different degree by increasing exposure to the electron beam. Enlarged images show SWNTs were obtained in these regions after CVD. (SWNTs look darker because they are more

conductive than the oxide layer.) The density of SWNTs grown may also be controlled by changing the dose (e.g. scanning times, current density, and acceleration voltage) to a given area. Since at low magnification and low current density the damage to the SAM is negligible, these conditions can be used to locate the desired area. Therefore, and most importantly, the patterning process becomes “visible” using this technique. For example, it would not be difficult to first look for pre-designed circuits, and then grow SWNTs at certain positions to bridge the electrodes. Finally, the current approach may also be utilized to pattern other nano-materials in a facile liquid-based way.

5.5 Summary

To summarize, I propose a surface-energy-difference driven selective deposition of catalyst for localized growth of SWNTs. For a SAM-patterned Si surface, catalyst particles deposit and SWNTs grow only on the hydrophilic regions. The presented all-liquid-based approach possesses significant advantages in scalability and resolution over state-to-the-art techniques, which I believe can greatly advance the fabrication of nano-devices using high-quality as-grown SWNTs.

Chapter 6 Conclusions and prospect

The synthesis of ^{13}C labeled SWNTs provides solid evidence for the root growth mechanism in alcohol catalytic CVD, which agrees well with the transmission electron microscopy (TEM) observations. A non-dimensional modulus is proposed to differentiate catalyst-poisoning controlled growth deceleration from one which is diffusion controlled. The calculation suggests that MWNT arrays are usually free of feedstock diffusion resistance while SWNT arrays are already suffering from a strong diffusion resistance. It also predicts the critical lengths in different CVD processes from which CNT begin to meet strong diffusion resistance.

Small concentration of acetylene in addition to ethanol was found to significantly enhance the growth rate of SWNTs. The very high activity of acetylene (estimated to be 1000 times that of ethanol) also suggests a possible fast chemical pathway from ethanol to SWNT formation. Thermal decomposition of ethanol is estimated by both calculation and experiment. Ethanol, ethylene and acetylene are found as the most important precursors for the formation of SWNTs in ACCVD. The relative ratio is critical for the quality of SWNT obtained.

The diameter distribution is not uniform throughout the array, and increases with longer synthesis time. CVD temperature and ethanol pressure have negligible effect on the average diameter of VA-SWNTs in ACCVD. However, the average diameter of VA-SWNTs can be tuned from 1.4 and 2.5 nm by modifying the catalyst recipe.

The conventional concept of using SiO_2 patterned Si substrates to selectively grow 3D carbon nanotube structures can also be applied to a dip-coating method. However, surface wettability strongly affects the catalyst deposition by dip-coating. The density of SWNTs

grown decreases when SiO₂ surface is functionalized by SAM and gets more hydrophobic. No SWNTs grow on SAM fully covered with SAM. This leads to a novel method for localizing the SWNT growth in a facile but precise way. When an e-beam is utilized, a 50 nm SWNT pattern can be easily obtained. The process is also visible in a conventional SEM.

Future work may be focused on:

- 1) Characterization and control the ratio between semi-conducting and metallic SWNTs in the VA-SWNT from ACCVD;
- 2) Revealing and quantifying the contribution of all precursors to SWNT formation;
- 3) Direct growth of narrow diameter and chirality distribution SWNTs;
- 4) FET performance of well-controlled as-grown SWNTs on substrate;
- 5) Fabrication of VA-SWNT composition and mass transport inside SWNT channels;
- 6) SWNT or other nano-material for energy conversion.

References

- [1] H. W. Kroto, J. R. Heath, S. C. O'Brien, R. F. Curl, R. E. Smalley, *Nature* **1985**, *318*, 162.
- [2] S. Iijima, T. Ichihashi, *Nature* **1993**, *363*, 603.
- [3] D. S. Bethune, C. H. Kiang, M. S. Devries, G. Gorman, R. Savoy, J. Vazquez, R. Beyers, *Nature* **1993**, *363*, 605.
- [4] S. Iijima, *Nature* **1991**, *354*, 56.
- [5] A. Oberlin, M. Endo, T. Koyama, *J. Cryst. Growth* **1976**, *32*, 335.
- [6] A. K. Geim, K. S. Novoselov, *Nat. Mater.* **2007**, *6*, 183.
- [7] R. Saito, A. Gruneis, G. G. Samsonidze, G. Dresselhaus, M. S. Dresselhaus, A. Jorio, L. G. Cancado, M. A. Pimenta, A. G. Souza, *Applied Physics a-Materials Science & Processing* **2004**, *78*, 1099.
- [8] M. S. Dresselhaus, P. C. Eklund, *Advances in Physics* **2000**, *49*, 705.
- [9] M. Lazzeri, S. Piscanec, F. Mauri, A. C. Ferrari, J. Robertson, *Phys. Rev. B* **2006**, *73*.
- [10] V. N. Popov, P. Lambin, *Physica Status Solidi B-Basic Solid State Physics* **2007**, *244*, 4269.
- [11] Y. Kawashima, G. Katagiri, *Phys. Rev. B* **1999**, *59*, 62.
- [12] S. Bandow, T. Hiraoka, T. Yumura, K. Hirahara, H. Shinohara, S. Iijima, *Chem. Phys. Lett.* **2004**, *384*, 320.
- [13] P. T. Araujo, S. K. Doorn, S. Kilina, S. Tretiak, E. Einarsson, S. Maruyama, H. Chacham, M. A. Pimenta, A. Jorio, *Phys. Rev. Lett.* **2007**, *98*.
- [14] L. T. Qu, F. Du, L. M. Dai, *Nano Lett.* **2008**, *8*, 2682.
- [15] L. Ding, A. Tselev, J. Y. Wang, D. N. Yuan, H. B. Chu, T. P. McNicholas, Y. Li, J. Liu, *Nano Lett.* **2009**, *9*, 800.
- [16] S. Maruyama, R. Kojima, Y. Miyauchi, S. Chiashi, M. Kohno, *Chem. Phys. Lett.* **2002**, *360*, 229.
- [17] M. S. Arnold, A. A. Green, J. F. Hulvat, S. I. Stupp, M. C. Hersam, *Nature Nanotechnology* **2006**, *1*, 60.
- [18] T. Omata, A. Suzuki, T. Sato, K. Minoshima, E. Nomaru, A. Murakami, S. Murayama, H. Kawahata, T. Maruyama, *Journal of Geophysical Research-Biogeosciences* **2008**, *113*.
- [19] C. Journet, W. K. Maser, P. Bernier, A. Loiseau, M. L. de la Chapelle, S. Lefrant, P. Deniard, R. Lee, J. E. Fischer, *Nature* **1997**, *388*, 756.
- [20] A. Thess, R. Lee, P. Nikolaev, H. J. Dai, P. Petit, J. Robert, C. H. Xu, Y. H. Lee, S. G. Kim, A. G. Rinzler, D. T. Colbert, G. E. Scuseria, D. Tomanek, J. E. Fischer, R. E. Smalley, *Science* **1996**, *273*, 483.
- [21] H. J. Dai, A. G. Rinzler, P. Nikolaev, A. Thess, D. T. Colbert, R. E. Smalley, *Chem. Phys. Lett.* **1996**, *260*, 471.
- [22] P. Nikolaev, M. J. Bronikowski, R. K. Bradley, F. Rohmund, D. T. Colbert, K. A. Smith, R. E. Smalley, *Chem. Phys. Lett.* **1999**, *313*, 91.
- [23] Y. Murakami, S. Chiashi, Y. Miyauchi, M. H. Hu, M. Ogura, T. Okubo, S. Maruyama, *Chem. Phys. Lett.* **2004**, *385*, 298.

- [24] Y. Murakami, Y. Miyauchi, S. Chiashi, S. Maruyama, *Chem. Phys. Lett.* **2003**, 374, 53.
- [25] Y. Shibuta, S. Maruyama, *Chem. Phys. Lett.* **2003**, 382, 381.
- [26] Y. Murakami, Y. Miyauchi, S. Chiashi, S. Maruyama, *Chem. Phys. Lett.* **2003**, 377, 49.
- [27] M. H. Hu, Y. Murakami, M. Ogura, S. Maruyama, T. Okubo, *J. Catal.* **2004**, 225, 230.
- [28] Y. Homma, Y. Kobayashi, T. Ogino, D. Takagi, R. Ito, Y. J. Jung, P. M. Ajayan, *J. Phys. Chem. B* **2003**, 107, 12161.
- [29] Y. Murakami, E. Einarsson, T. Edamura, S. Maruyama, *Carbon* **2005**, 43, 2664.
- [30] K. Hata, D. N. Futaba, K. Mizuno, T. Namai, M. Yumura, S. Iijima, *Science* **2004**, 306, 1362.
- [31] G. F. Zhong, T. Iwasaki, K. Honda, Y. Furukawa, I. Ohdomari, H. Kawarada, *Chem Vapor Depos* **2005**, 11, 127.
- [32] G. Y. Zhang, D. Mann, L. Zhang, A. Javey, Y. M. Li, E. Yenilmez, Q. Wang, J. P. McVittie, Y. Nishi, J. Gibbons, H. J. Dai, *Proc. Natl. Acad. Sci. U.S.A.* **2005**, 102, 16141.
- [33] Y. Q. Xu, E. Flor, M. J. Kim, B. Hamadani, H. Schmidt, R. E. Smalley, R. H. Hauge, *J Am Chem Soc* **2006**, 128, 6560.
- [34] G. Eres, A. A. Kinkhabwala, H. T. Cui, D. B. Geohegan, A. A. Puzos, D. H. Lowndes, *J. Phys. Chem. B* **2005**, 109, 16684.
- [35] S. Noda, K. Hasegawa, H. Sugime, K. Kakehi, Z. Y. Zhang, S. Maruyama, Y. Yamaguchi, *Japanese Journal of Applied Physics Part 2-Letters & Express Letters* **2007**, 46, L399.
- [36] L. Zhang, Y. Q. Tan, D. E. Resasco, *Chem. Phys. Lett.* **2006**, 422, 198.
- [37] W. Z. Li, S. S. Xie, L. X. Qian, B. H. Chang, B. S. Zou, W. Y. Zhou, R. A. Zhao, G. Wang, *Science* **1996**, 274, 1701.
- [38] S. S. Fan, M. G. Chapline, N. R. Franklin, T. W. Tomblor, A. M. Cassell, H. J. Dai, *Science* **1999**, 283, 512.
- [39] C. N. R. Rao, R. Sen, B. C. Satishkumar, A. Govindaraj, *Chem. Commun.* **1998**, 1525.
- [40] A. E. Aliev, C. Guthy, M. Zhang, S. Fang, A. A. Zakhidov, J. E. Fischer, R. H. Baughman, *Carbon* **2007**, 45, 2880.
- [41] H. Huang, C. H. Liu, Y. Wu, S. S. Fan, *Adv. Mater.* **2005**, 17, 1652.
- [42] N. Yamamoto, A. J. Hart, E. J. Garcia, S. S. Wicks, H. M. Duong, A. H. Slocum, B. L. Wardle, *Carbon* **2009**, 47, 551.
- [43] A. Moisala, Q. Li, I. A. Kinloch, A. H. Windle, *Composites science and technology* **2006**, 66, 1285.
- [44] E. J. Garcia, B. L. Wardle, A. J. Hart, N. Yamamoto, *Composites Science and Technology* **2008**, 68, 2034.
- [45] E. J. Garcia, A. J. Hart, B. L. Wardle, A. H. Slocum, *Adv. Mater.* **2007**, 19, 2151.
- [46] Y. Murakami, S. Chiashi, E. Einarsson, S. Maruyama, *Phys. Rev. B* **2005**, 71.
- [47] Y. Murakami, E. Einarsson, T. Edamura, S. Maruyama, *Phys. Rev. Lett.* **2005**, 94, 087402.
- [48] C. L. Pint, Y. Q. Xu, M. Pasquali, R. H. Hauge, *Acs Nano* **2008**, 2, 1871.
- [49] Y. Hayamizu, T. Yamada, K. Mizuno, R. C. Davis, D. N. Futaba, M. Yumura, K. Hata, *Nature Nanotechnology* **2008**, 3, 289.
- [50] L. Ren, C. L. Pint, L. G. Booshenri, W. D. Rice, X. F. Wang, D. J. Hilton, K. Takeya, I. Kawayama, M. Tonouchi, R. H. Hauge, J. Kono, *Nano Lett.* **2009**, 9, 2610.
- [51] K. L. Jiang, Q. Q. Li, S. S. Fan, *Nature* **2002**, 419, 801.
- [52] M. Zhang, K. R. Atkinson, R. H. Baughman, *Science* **2004**, 306, 1358.

- [53] M. Zhang, S. L. Fang, A. A. Zakhidov, S. B. Lee, A. E. Aliev, C. D. Williams, K. R. Atkinson, R. H. Baughman, *Science* **2005**, *309*, 1215.
- [54] L. Zhang, C. Feng, Z. Chen, L. Liu, K. L. Jiang, Q. Q. Li, S. S. Fan, *Nano Lett.* **2008**, *8*, 2564.
- [55] L. Xiao, Z. Chen, C. Feng, L. Liu, Z. Q. Bai, Y. Wang, L. Qian, Y. Y. Zhang, Q. Q. Li, K. L. Jiang, S. S. Fan, *Nano Lett.* **2008**, *8*, 4539.
- [56] K. Liu, Y. H. Sun, L. Chen, C. Feng, X. F. Feng, K. L. Jiang, Y. G. Zhao, S. S. Fan, *Nano Lett.* **2008**, *8*, 700.
- [57] B. Yurdumakan, N. R. Raravikar, P. M. Ajayan, A. Dhinojwala, *Chem. Commun.* **2005**, 3799.
- [58] Y. Zhao, T. Tong, L. Delzeit, A. Kashani, M. Meyyappan, A. Majumdar, *Journal of Vacuum Science & Technology B* **2006**, *24*, 331.
- [59] L. Ge, S. Sethi, L. Ci, P. M. Ajayan, A. Dhinojwala, *Proc. Natl. Acad. Sci. U.S.A.* **2007**, *104*, 10792.
- [60] S. Sethi, L. Ge, L. Ci, P. M. Ajayan, A. Dhinojwala, *Nano Lett.* **2008**, *8*, 822.
- [61] L. T. Qu, L. M. Dai, M. Stone, Z. H. Xia, Z. L. Wang, *Science* **2008**, *322*, 238.
- [62] G. Hummer, J. C. Rasaiah, J. P. Noworyta, *Nature* **2001**, *414*, 188.
- [63] A. Kalra, S. Garde, G. Hummer, *Proc. Natl. Acad. Sci. U.S.A.* **2003**, *100*, 10175.
- [64] J. K. Holt, H. G. Park, Y. M. Wang, M. Stadermann, A. B. Artyukhin, C. P. Grigoropoulos, A. Noy, O. Bakajin, *Science* **2006**, *312*, 1034.
- [65] H. Verweij, M. C. Schillo, J. Li, *Small* **2007**, *3*, 1996.
- [66] R. S. Wagner, W. C. Ellis, *Appl. Phys. Lett.* **1964**, *4*, 89.
- [67] S. B. Sinnott, R. Andrews, D. Qian, A. M. Rao, Z. Mao, E. C. Dickey, F. Derbyshire, *Chem. Phys. Lett.* **1999**, *315*, 25.
- [68] L. Liu, S. S. Fan, *J. Am. Chem. Soc.* **2001**, *123*, 11502.
- [69] X. Li, A. Y. Cao, Y. J. Jung, R. Vjatai, P. M. Ajayan, *Nano Lett.* **2005**, *5*, 1997.
- [70] L. B. Zhu, Y. H. Xiu, D. W. Hess, C. P. Wong, *Nano Lett.* **2005**, *5*, 2641.
- [71] R. Xiang, G. H. Luo, W. Z. Qian, Q. Zhang, Y. Wang, F. Wei, Q. Li, A. Y. Cao, *Adv. Mater.* **2007**, *19*, 2360.
- [72] D. B. Geohegan, A. A. Puzos, I. N. Ivanov, S. Jesse, G. Eres, J. Y. Howe, *Appl. Phys. Lett.* **2003**, *83*, 1851.
- [73] K. Liu, K. L. Jiang, C. Feng, Z. Chen, S. S. Fan, *Carbon* **2005**, *43*, 2850.
- [74] S. Maruyama, E. Einarsson, Y. Murakami, T. Edamura, *Chem. Phys. Lett.* **2005**, *403*, 320.
- [75] E. Einarsson, Y. Murakami, M. Kadowaki, S. Maruyama, *Carbon* **2008**, *46*, 923.
- [76] A. A. Puzos, D. B. Geohegan, S. Jesse, I. N. Ivanov, G. Eres, *Applied Physics a-Materials Science & Processing* **2005**, *81*, 223.
- [77] E. R. Meshot, A. J. Hart, *Appl. Phys. Lett.* **2008**, *92*, 113107.
- [78] J. H. Han, R. A. Graff, B. Welch, C. P. Marsh, R. Franks, M. S. Strano, *Acs Nano* **2008**, *2*, 53.
- [79] M. Picher, E. Anglaret, R. Arenal, V. Jourdain, *Nano Lett.* **2009**, *9*, 542.
- [80] M. Stadermann, S. P. Sherlock, J. B. In, F. Fornasiero, H. G. Park, A. B. Artyukhin, Y. M. Wang, J. J. De Yoreo, C. P. Grigoropoulos, O. Bakajin, A. A. Chernov, A. Noy, *Nano Lett.* **2009**, *9*, 738.
- [81] R. Saito, G. Dresselhaus, M. S. Dresselhaus, *Physical Properties of Carbon Nanotubes*, Imperial College Press, London **1998**.
- [82] M. Pinault, V. Pichot, H. Khodja, P. Launois, C. Reynaud, M. Mayne-L'Hermite, *Nano Lett.* **2005**, *5*, 2394.
- [83] F. Simon, C. Kramberger, R. Pfeiffer, H. Kuzmany, V. Zolyomi, J. Kurti, P. M. Singer, H. Alloul, *Phys. Rev. Lett.* **2005**, *95*, 017401.

- [84] Y. Miyauchi, S. Maruyama, *Phys. Rev. B* **2006**, *74*, 35415.
- [85] J. Shiomi, S. Maruyama, *Phys. Rev. B* **2006**, *74*, 155401.
- [86] T. Iwasaki, G. F. Zhong, T. Aikawa, T. Yoshida, H. Kawarada, *J. Phys. Chem. B* **2005**, *109*, 19556.
- [87] Z. F. Ren, Z. P. Huang, J. W. Xu, J. H. Wang, P. Bush, M. P. Siegal, P. N. Provencio, *Science* **1998**, *282*, 1105.
- [88] Mathieu Pinault, Vincent Pichot, Hicham Khodja, Pascale Launois, Ce'cile Reynaud, M. Mayne-L'Hermite, *Nano Lett.* **2005**.
- [89] L. B. Zhu, D. W. Hess, C. P. Wong, *Journal of Physical Chemistry B* **2006**, *110*, 5445.
- [90] O. Levenspiel, *Chemical Reaction Engineering, Second Edition*, WILEY-VCH, Weinheim, Germany 1972.
- [91] D. N. Futaba, K. Hata, T. Yamada, K. Mizuno, M. Yumura, S. Iijima, *Phys. Rev. Lett.* **2005**, *95*.
- [92] B. E. Deal, A. S. Grove, *J. Appl. Phys.* **1965**, *36*, 3770.
- [93] W. P. Zhou, Y. L. Wu, F. Wei, G. H. Luo, W. Z. Qian, *Polymer* **2005**, *46*, 12689.
- [94] E. Einarsson, M. Kadowaki, K. Ogura, J. Okawa, R. Xiang, Z. Zhang, Y. Yamamoto, Y. Ikuhara, S. Maruyama, *J. Nanosci. Nanotechnol.* **2008**, *8*, 6093.
- [95] R. Xiang, G. H. Luo, W. Z. Qian, Q. Zhang, Y. Wang, F. Wei, Q. Li, A. Y. Cao, *Advanced Materials* **2007**, *In press*.
- [96] D. N. Futaba, K. Hata, T. Namai, T. Yamada, K. Mizuno, Y. Hayamizu, M. Yumura, S. Iijima, *Journal of Physical Chemistry B* **2006**, *110*, 8035.
- [97] G. F. Zhong, T. Iwasaki, H. Kawarada, *Carbon* **2006**, *44*, 2009.
- [98] G. F. Zhong, T. Iwasaki, J. Robertson, H. Kawarada, *J. Phys. Chem. B* **2007**, *111*, 1907.
- [99] H. Oshima, Y. Suzuki, T. Shimazu, S. Maruyama, *Jpn. J. Appl. Phys.* **2007**, *47*, 1982.
- [100] S. Carbon Nanotubes: Advanced Topics in the Synthesis, Properties and Applications (Eds.: A. Jorio, M. S. Dresselhaus, G. Dresselhaus), *Springer*, 2007.
- [101] A. Y. Cao, P. L. Dickrell, W. G. Sawyer, M. N. Ghasemi-Nejhad, P. M. Ajayan, *Science* **2005**, *310*, 1307.
- [102] B. J. Hinds, N. Chopra, T. Rantell, R. Andrews, V. Gavalas, L. G. Bachas, *Science* **2004**, *303*, 62.
- [103] M. F. Yu, Y. H. Funke, J. L. Falconer, R. D. Noble, *Nano Lett.* **2009**, *9*, 225.
- [104] E. Einarsson, Y. Murakami, M. Kadowaki, S. Maruyama, *Carbon* **2008**, *46*, 923.
- [105] R. Xiang, Z. Zhang, K. Ogura, J. Okawa, E. Einarsson, Y. Miyauchi, J. Shiomi, S. Maruyama, *Jpn. J. Appl. Phys.* **2008**, *47*, 1971.
- [106] R. Xiang, Z. Yang, Q. Zhang, G. H. Luo, W. Z. Qian, F. Wei, M. Kadowaki, S. Maruyama, *J. Phys. Chem. C* **2008**, *112*, 4892.
- [107] Y. H. Wang, M. J. Kim, H. W. Shan, C. Kittrell, H. Fan, L. M. Ericson, W. F. Hwang, S. Arepalli, R. H. Hauge, R. E. Smalley, *Nano Lett.* **2005**, *5*, 997.
- [108] J. Warnatz, U. Maas, R. W. Dibble, *Combustion: Physical and Chemical Fundamentals, Modeling and Simulation, Experiments, Pollutant Formation, third edn.*, Springer, Berlin, **2001**, 257.
- [109] Q. Wen, W. Z. Qian, F. Wei, Y. Liu, G. Q. Ning, Q. Zhang, *Chem. Mater.* **2007**, *19*, 1226.
- [110] T. Yamada, A. Maigne, M. Yudasaka, K. Mizuno, D. N. Futaba, M. Yumura, S. Iijima, K. Hata, *Nano Lett.* **2008**, *8*, 4288.
- [111] Jung Y J, Wei B Q, Vajtai R, Ajayan P M, Homma Y, Prabhakaran K, Ogino T, *Nano Lett.* **2003**, *3*, 561.
- [112] G. Rotzoll, *Journal of Analytical and Applied Pyrolysis* **1985**, *9*, 43.

- [113] H. Sugime, S. Noda, S. Maruyama, Y. Yamaguchi, *Carbon* **2009**, *47*, 234.
- [114] S. Maruyama, Y. Miyauchi, *Electronic Properties of Novel Nanostructure (AIP Conf. Proc. 786)* **2005**, 100.
- [115] R. Xiang, E. Einarsson, J. Okawa, Y. Miyauchi, S. Maruyama, *J. Phys. Chem. C*, *in press*.
- [116] R. Andrews, D. Jacques, D. Qian, T. Rantell, *Acc. Chem. Res.* **2002**, *35*, 1008.
- [117] H. M. Cheng, F. Li, G. Su, H. Y. Pan, L. L. He, X. Sun, M. S. Dresselhaus, *Appl Phys Lett* **1998**, *72*, 3282.
- [118] L. X. Zheng, M. J. O'Connell, S. K. Doorn, X. Z. Liao, Y. H. Zhao, E. A. Akhadov, M. A. Hoffbauer, B. J. Roop, Q. X. Jia, R. C. Dye, D. E. Peterson, S. M. Huang, J. Liu, Y. T. Zhu, *Nat. Mater.* **2004**, *3*, 673.
- [119] Y. Sato, K. Yanagi, Y. Miyata, K. Suenaga, H. Kataura, S. Lijima, *Nano Lett.* **2008**, *8*, 3151.
- [120] T. Yamada, T. Namai, K. Hata, D. N. Futaba, K. Mizuno, J. Fan, M. Yudasaka, M. Yumura, S. Iijima, *Nature Nanotechnology* **2006**, *1*, 131.
- [121] M. G. Hahn, Y. K. Kwon, E. Lee, C. W. Ahn, Y. J. Jung, *Journal of physical Chemistry C* **2008**, DOI: 10.1021/jp8073877.
- [122] J. Jiang, R. Saito, K. Sato, J. S. Park, G. G. Samsonidze, A. Jorio, G. Dresselhaus, M. S. Dresselhaus, *Phys Rev B* **2007**, *75*.
- [123] L. M. Dell'Acqua-Bellavitis, J. D. Ballard, P. M. Ajayan, R. W. Siegel, *Nano Lett.* **2004**, *4*, 1613.
- [124] A. J. Hart, L. van Laake, A. H. Slocum, *Small* **2007**, *3*, 772.
- [125] S. Chakrabarti, K. Gong, L. Dai, *Journal of Physical Chemistry C* **2008**, *112*, 8136.
- [126] S. Helveg, C. Lopez-Cartes, J. Sehested, P. L. Hansen, B. S. Clausen, J. R. Rostrup-Nielsen, F. Abild-Pedersen, J. K. Nørskov, *Nature* **2004**, *427*, 426.
- [127] S. M. Huang, L. M. Dai, A. W. H. MAU, *Adv. Mater.* **2002**, *14*, 1140.
- [128] B. Q. Wei, R. Vajtai, Y. Jung, J. Ward, R. Zhang, G. Ramanath, P. M. Ajayan, *Nature* **2002**, *416*, 495.
- [129] R. Xiang, G. H. Luo, Z. Yang, Q. Zhang, W. Z. Qian, F. Wei, *Nanotechnology* **2007**, *18*, 415703.
- [130] A. Javey, H. J. Dai, *J. Am. Chem. Soc.* **2005**, *127*, 11942.
- [131] M. S. He, X. Ling, J. Zhang, Z. F. Liu, *J. Phys. Chem. B* **2005**, *109*, 10946.
- [132] A. Ulman, *Chemical Reviews* **1996**, *96*, 1533.
- [133] R. Xiang, Z. Yang, Q. Zhang, G. H. Luo, W. Z. Qian, F. Wei, M. Kadowaki, E. Einarsson, S. Maruyama, *J. Phys. Chem. C* **2008**, *112*, 4892.
- [134] Z. J. Zhang, Y. Zhou, Yue Y, *Appl. Phys. Lett.* **2005**, *87*, 223121.
- [135] R. Xiang, T. Z. Wu, E. Einarsson, Y. Suzuki, J. Shiomi, S. Maruyama, *J. Am. Chem. Soc.* **2009**, DOI: 10.1021/ja902904v.
- [136] S. Onclin, B. J. Ravoo, D. N. Reinhoudt, *Angew. Chem.* **2005**, *44*, 6282.
- [137] Z. F. Liu, Z. Y. Shen, T. Zhu, S. F. Hou, L. Z. Ying, Z. J. Shi, Z. N. Gu, *Langmuir* **2000**, *16*, 3569.
- [138] J. A. Bardecker, A. Afzali, G. S. Tulevski, T. Graham, J. B. Hannon, A. K. Y. Jen, *J. Am. Chem. Soc.* **2008**, *130*, 7226.
- [139] S. G. Rao, L. Huang, W. Setyawan, S. Hong, *Nature* **2003**, *425*, 36.
- [140] H. Sugimura, N. Nakagiri, N. Ichinose, *Appl. Phys. Lett.* **1995**, *66*, 3686.

Appendix

Further explanation of equation (5) in chapter 2.

All units are listed in Table 2-1.

Depending on the values of $\left(\frac{D_e}{k_s}\right)^2$ and $\frac{2D_e C_0}{a}t$,

$L = \sqrt{\left(\frac{D_e}{k_s}\right)^2 + \frac{2D_e C_0}{a}t} - \frac{D_e}{k_s}$ can be either proportional to t or $t^{1/2}$.

When $\left(\frac{D_e}{k_s}\right)^2 \ll \frac{2D_e C_0}{a}t$,

$$L = \sqrt{\left(\frac{D_e}{k_s}\right)^2 + \frac{2D_e C_0}{a}t} - \frac{D_e}{k_s} = \sqrt{\frac{2D_e C_0}{a}t} \propto t^{1/2};$$

When $\left(\frac{D_e}{k_s}\right)^2 \gg \frac{2D_e C_0}{a}t$

$$L = \left(\sqrt{\left(\frac{D_e}{k_s}\right)^2 + \frac{2D_e C_0}{a}t} - \frac{D_e}{k_s} \right) \times \frac{\sqrt{\left(\frac{D_e}{k_s}\right)^2 + \frac{2D_e C_0}{a}t} + \frac{D_e}{k_s}}{\sqrt{\left(\frac{D_e}{k_s}\right)^2 + \frac{2D_e C_0}{a}t} + \frac{D_e}{k_s}} = \frac{C_0 k_s}{a} t \propto t$$

Details of some calculations

Mean free path of molecules:

$$\lambda = \frac{RT}{\sqrt{2}\pi d^2 N_A p},$$

where R is the real gas constant, T is temperature, d the molecule diameter, N_A is Avogadro's number, and p is pressure.

Knudsen diffusion coefficient D_K (cm²/s):

$$D_K = 9700r \frac{\rho}{\tau} \left(\frac{T}{M} \right)^{1/2}$$

where r is the channel diameter (cm²/s), ρ is the porosity of the CNT membrane, τ is the tortuosity of diffusion channel, T is temperature (K), and M is molecular weight. Tortuosity τ in our estimation was approximated to 1.5 in all cases, because it is the typical value for aligned MWNTs (ref 93). As discussed in the main text, error here will not significantly affect in the overall conclusions, i.e. judging the existence (or not) of a diffusion limit from φ .

Molecular diffusion coefficient D_{AB} (cm²/s):

$$D_{AB} = 0.001858T^{3/2} \frac{(1/M_A + 1/M_B)^{1/2}}{P\sigma_{AB}^2\Omega_{AB}} \left(\frac{T}{M} \right)^{1/2}$$

where T is temperature (K), M molecular weight, P pressure (atm), σ mean molecular diameter (armstrong), and Ω collision integration. A and B stand for two components of the gas mixture in our calculation, which are the carbon source (e.g. C₂H₄ or C₆H₁₂) and a carrier gas (e.g. Ar).

Effective diffusion coefficient:

$$D_e = \left(\frac{1}{D_K} + \frac{1}{D_{AB}} \right)^{-1}$$

where D_k is the Knudsen diffusion coefficient and D_{AB} the molecular diffusion coefficient.

Further discussion on k_s

In equation (5)

$$L = \sqrt{\left(\frac{D_e}{k_s}\right)^2 + \frac{2D_e C_0}{a} t} - \frac{D_e}{k_s},$$

constant k_s (no catalyst deactivation) is required to fit/predict the time-dependent growth curve. However, in most cases, catalyst activity is always diminishing, which means this equation is too ideal to be applied to a real system.

In the present method, the initial reaction constant at $t=0$ (when there is no diffusion problem involved), k_{s0} was sufficient to exclude the diffusion limit for MWNT arrays and predict the CNT length for SWNT arrays. No complete information of catalyst decay is needed.

For the growth of mm-scale MWNT arrays, even when constant k_{s0} was used, φ is small and η is near unity. If there is some catalyst deactivation (k_s will decrease), φ will be even smaller. Therefore, even when the diffusion is maximized, there is no limit for these aligned MWNT arrays.

For the growth of mm-scale SWNT arrays, even if there is no catalyst deactivation (using k_{s0}), the growth will be slowed down by the feedstock diffusion limitation. Therefore, in a real case with catalyst deactivation, SWNT arrays might not be able to grow over several mm if keeping the bulk concentration constant.

Acknowledgements

First and foremost, this PhD would not have been possible without the generous funding from the Japanese Ministry of Education (Monbukagakusho), and for that I am most grateful. This support from the 21st Century COE and GCOE project allowed me to present results of this research at a number of domestic and international conferences.

I am very grateful to my thesis advisor, Professor S. Maruyama, who picked me up three years ago from Beijing and gave me this precious chance to study in his Lab. He has taught me too many things to begin to list here, and I thank him for his advice, patience and understanding. This three year experience in his group will benefit me the rest of my life.

It is very joyful to work with J. Shiomi, who advised me a lot and helped me start collaboration with many groups. I am also very lucky to have had the chance to work with Y. Murakami, who pioneered the growth of vertically aligned SWNTs and taught me many things. I also thank other members in Maruyama Lab., particularly E. Einarsson for the help on paper writing and POVray, and Z. Zhang for the assistance on Raman measurement. S. Chiashi, Y. Miyauchi, Kei-san, S. Aikawa, P. Zhao, J. Okawa, H. Okabe, T. Thurakitseree, ... also helped me a lot.

Much of this work would not have been completed without our collaborators. I appreciate the support from Prof. Y. Suzuki, Prof. T. Kitamori and Prof. J. Choi on MEMS fabrication. The constructive discussions with Prof. S. Noda, Prof. T. Okubo, Prof. Y. Ohno and Prof. F. Wei are also very helpful to this thesis.

I would like to thank all my Chinese friends, particularly T. Wu and P. Shen, in UT Fantuan, where we had not only joyful dinners but also brainstorming on research. Finally, I want to express my hearty gratitude to my fiancée, Ying, and my family for their understanding and encouragement.

Curriculum Vitae

PhD Course	<u>The University of Tokyo</u> , Dept. of Mechanical Engineering (Advisor: Prof. Shigeo Maruyama)	Oct 2006 - Present
Master of Eng.	<u>Tsinghua University</u> , Dept. of Chemical Engineering (Advisor: Prof. Guohua Luo, Prof. Fei Wei)	Sep 2003 - Jul 2006
Bachelor of Science	<u>University of Science and Technology of China</u> , Dept. of Chemical Physics	Sep 1999 - Jul 2003

Publication list

Patents

1. S. Maruyama, **R. Xiang**, A facile liquid strategy for localized growth of high-quality single-walled carbon nanotubes. 2009, submitted.
2. F. Wei, G. H. Luo, **R. Xiang**, Method for large-batch preparing overlength carbon nano pipe array and its apparatus, Chinese Patent 2006, CN1724343-A; CN1312033-C.

Peer-reviewed journals

1. **R. Xiang**, E. Einarsson, J. Okawa, Y. Murakami, J. Shiomi, S. Maruyama, Quantifying Hidden Species for the Catalytic Formation of Single Walled Carbon Nanotubes from Alcohol, in preparation.
2. **R. Xiang**, E. Einarsson, J. Okawa, Y. Murakami, J. Shiomi, S. Maruyama, Vertically Aligned Exclusively Single Walled Carbon Nanotubes with Tunable Diameter Distribution, to be submitted.
3. **R. Xiang**, E. Einarsson, H. Okabe, S. Chiashi, J. Shiomi, S. Maruyama, Patterned Growth of High-quality Single-walled Carbon Nanotubes from Dip-coated Catalyst, *Jpn. J. Appl. Phys.*, submitted
4. **R. Xiang**, T. Z. Wu, E. Einarsson, Y. Suzuki, J. Shiomi, S. Maruyama, "High-Precision Selective Deposition of Catalyst for Facile Localized Growth of Single Walled Carbon Nanotubes", *J. Am. Chem. Soc.*, 2009, 131, 10344.
5. **R. Xiang**, E. Einarsson, J. Okawa, T. Thurakitsee, Y. Murakami, J. Shiomi, Y. Ohno, S. Maruyama, "Identifying key parameters in controlled synthesis of vertically aligned single-walled carbon nanotubes from ethanol," *J. Nanosci. Nanotechnol.* 2009, in press.
6. **R. Xiang**, E. Einarsson, J. Okawa, Y. Miyauchi, S. Maruyama, Acetylene-Accelerated Formation of Vertically Aligned Single Walled Carbon Nanotubes, *J. Phys. Chem. C* 2009, 113, 7511.
7. **R. Xiang**, Z. Yang, Q. Zhang, G. H. Luo, W. Z. Qian, F. Wei, E. Einarsson, S. Maruyama. Decelerating Growth of Vertically Aligned Carbon Nanotube Arrays: Catalyst Deactivation or Feedstock Diffusion Controlled?, *J. Phys. Chem. C* 2008, 112, 4892.
8. **R. Xiang**, Z. Zhang, K. Ogura, J. Okawa, E. Einarsson, Y. Miyauchi, J. Shiomi, S. Maruyama. Vertically Aligned ^{13}C Single-Walled Carbon Nanotubes from No-flow Alcohol Chemical Vapor Deposition and their Root Growth Mechanism, *Jpn. J. Appl. Phys.* 2008, 47, 1971.
9. **R. Xiang**, G. H. Luo, Z. Yang, Q. Zhang, W. Z. Qian, F. Wei. Large Area Growth of Aligned CNT arrays on Spheres: Cost performance and Product Control, *Mater. Lett.* 2009, 63, 84.
10. **R. Xiang**, G. H. Luo, Z. Yang, Q. Zhang, W. Z. Qian, F. Wei. Temperature effect on the substrate selectivity of carbon nanotube growth in floating chemical vapor deposition, *Nanotechnology* 2007, 18, 415703.
11. **R. Xiang**, G. H. Luo, W. Z. Qian, Y. Wang, F. Wei, Q. Li. Large Area Growth of Aligned CNT Arrays on Spheres: Towards Large Scale and Continuous Production, *Chem. Vapor Depos.* 2007, 13, 533.
12. **R. Xiang**, G. H. Luo, W. Z. Qian, Q. Zhang, Y. Wang, F. Wei, Q. Li, A. Y. Cao. Encapsulation, compensation, and substitution of catalyst particles during continuous growth of carbon nanotubes, *Adv. Mater.* 2007, 19, 2360.

13. P. Zhao, E. Einarsson, **R. Xiang**, Y. Murakami, S. Maruyama, Controllable Full-Color Expansion of Dispersed Single-walled Carbon Nanotubes Using Density Gradient Ultracentrifugation, to be submitted.
14. E. Einarsson, K. Kadowaki, K. Ogura, J. Okawa, **R. Xiang**, Z. Y. Zhang, T. Yamamoto, Y. Ikuhara, S. Maruyama. Growth mechanism and internal structure of vertically aligned single-walled carbon nanotubes, *J. Nanosci. Nanotechnol.* 2008, 8, 6093.
15. H. M. Duong, E. Einarsson, J. Okawa, **R. Xiang**, S. Maruyama. Thermal degradation of single-walled carbon nanotubes, *Jpn. J. Appl. Phys.* 2008, 47, 1994.
16. Q. Zhang, W. Z. Qian, **R. Xiang**, Z. Yang, G. H. Luo, Y. Wang, F. Wei. In situ growth of carbon nanotubes on inorganic fibers with different surface properties, *Mater. Chem. Phys.* 2008, 107, 317.
17. F. Wei, Q. Zhang, W. Z. Qian, G. H. Xu, **R. Xiang**, Q. Wen, Y. Wang, G. H. Luo. Progress on aligned carbon nanotube arrays, *New Carbon Materials* 2007, 22, 271.
18. Q. Zhang, W. P. Zhou, W. Z. Qian, **R. Xiang**, J. Q. Huang, D. Z. Wang, F. Wei. Synchronous Growth of Vertically Aligned Carbon Nanotubes with Pristine Stress in the Heterogeneous Catalysis Process, *J. Phys. Chem. C* 2007, 111, 14638.
19. Z. F. Li, G. H. Luo, W. P. Zhou, F. Wei, **R. Xiang**, Y. P. Liu. The quantitative characterization of the concentration and dispersion of multi-walled carbon nanotubes in suspension by spectrophotometry, *Nanotechnology* 2006, 17, 3692.
20. Z. F. Zhang, G. H. Luo, Z. J. Fan, **R. Xiang**, L. Zhou, F. Wei. Complex permittivity and permeability spectra of different kinds of carbon nanotubes, *Acta Physico-Chimica Sinica* 2006, 22, 296.

Conference Contributions

1. **R. Xiang**, et al., ASME 2009 2nd Micro/Nanoscale Heat & Mass Transfer International Conference, Dec. 2009, Shanghai, China.
2. **R. Xiang**, et al., 37th Fullerene Nanotube General Symposium, Sep. 2009, Tsukuba, Japan.
3. **R. Xiang**, et al., 10th International Conference on the Science and Application of Nanotubes (NT09), Jun. 2009, Beijing, China.
4. **R. Xiang**, et al., APS March Meeting, Mar. 2009, Pittsburgh, USA.
5. **R. Xiang**, et al., IWEPNM 2009, Mar. 2009, Kirchberg, Austria.
6. **R. Xiang**, et al., 36th Fullerene Nanotube General Symposium, Mar. 2009, Nagoya, Japan.
7. **R. Xiang**, et al., MRS Fall Meeting, Dec. 2008, Boston, USA.
8. **R. Xiang**, et al., The 5th Japan-Korea Symposium on Carbon Nanotube, Nov. 2008, Pusan, Korea.
9. **R. Xiang**, et al., 35th Fullerene Nanotube General Symposium, Aug. 2008, Tokyo, Japan.
10. **R. Xiang**, et al., 9th International Conference on the Science and Application of Nanotubes (NT08), Jul. 2008, Montpellier, France.
11. **R. Xiang**, et al., the Japan Society of Applied Physics Annual Meeting 2008, Mar. 2008, Chiba, Japan.
12. **R. Xiang**, et al., The American Physical Society (APS) March Meeting, Mar. 2008, New Orleans, USA.
13. **R. Xiang**, et al., 34th Fullerene Nanotube General Symposium Spring Meeting, Mar. 2008, Nagoya, Japan.
14. **R. Xiang**, et al., The 34th International Symposium on Compound Semiconductors (ISCS 2007), Oct. 2007, Kyoto, Japan.
15. **R. Xiang**, et al., 8th International Conference on the Science and Application of Nanotubes (NT07), May 2007, Ouro Preto, Brazil.
16. **R. Xiang**, et al., China/USA/Japan Joint Chemical Engineering Conference, Oct. 2005, Beijing, China

